國立臺灣大學理學院化學研究所

碩士論文

Department of Chemistry

College of Science

National Taiwan University

Master Thesis

PSII 複合體光捕捉動力學的理論研究

A Theoretical Study on Dynamics of Light Harvesting in Photosystem II Supercomplex

洪加城

Jia-Cheng Hong

指導教授: 鄭原忠 博士

Advisor: Yuan-Chung Cheng, Ph.D.

中華民國 112 年 7 月

July, 2023

doi:10.6342/NTU202301637

doi:10.6342/NTU202301637

doi:10.6342/NTU202301637

Acknowledgements

在過去的兩年研究生涯中，我最感謝的是鄭原忠老師。首先，我的指導教授讓我體會了從 fundamental 到與實驗連結的過程，使我更深刻地體會到理論化學家如何給出科學上的 insight。我從最基礎的模型開始建立，到後續的模型驗證與探究 PSII-sc 有哪些特性，這裡的每一步中，老師都會先給個開頭，讓我自己去嘗試與挖掘。接下來，老師再跟我討論從我的模擬中看到的現象。這個過程讓我充分地體會到怎麼系統性地研究問題，並給出定量的科學證據支持我的結論。第二，我在研究初期的時候卡了很久，老師都會適時地提點我，讓我在比較沒有壓力地的情況下，完成我的工作。在碩一的時間中，我花了很多時間在建立計算 EET rate 的方法、計算時間加速與模型驗證上。從一開始，跑一次 EET rate matrix 可能需要一周左右的時間，到後期跑一次只需要 0.7 秒。我對計算方法做了許多改良，也感謝老師讓我有充裕的時間。另外，我很感謝我的研究 partner 楊允中、實驗室的其他人和我討論的我的研究工作，給了我許多靈感，讓我的研究更加完整。最後，我也感謝金必耀老師在 Group Meeting 的時候給我的許多意見以及對用字遣詞上的糾正。

doi:10.6342/NTU202301637

doi:10.6342/NTU202301637

摘要

光合作用系統 II (PSII) 仰賴一個巨大的天線複合體用以蒐集充足的光能，這些光能能夠驅動光合作用系統 II 中的反應中心 (RCs)。在這個光捕捉的過程中，太陽光會激發天線複合體中的色素分子，將光能轉換成激發能。然而，在激發能從天線複合體轉移到 RCs 的過程中，蛋白質結構的振動會擾動各個色素分子的激發能，從而在 PSII 上形成一個波動的能量曲面。此外，巨大的天線複合體中的色素分子數目遠遠超過 RC 中的數目，這樣的差異使得巨大的天線複合體具有更高的自由度，同時也產生了相對應的熵效應。即便在這些限制下，PSII 仍能在光捕捉的過程中保持高量子效率。因此，我們需要瞭解大自然使用了哪些策略。了解這些策略對於我們理解 PSII 如何在限制條件下實現高效能光捕捉至關重要。為此，我們建立了一個光合作用系統 II 激發能轉移的簡化群集模型，我們能夠建立有效的內能能量曲面。從這個能量曲面上，我們發現在群集中有一些特殊的時標分離 (timescale separation) 的性質，降低了激發能在天線複合體中的自由度並促進激發能進入反應中心。另外，光合作用系統 II 在其主要的能量轉移路徑上設計了精巧的能量梯度，這些優化能量曲面的設計是用來達成高效地光捕捉。同時，PSII 還利用熱能來克服激發能擾動所產生的障礙。透過研究 PSII 能量曲面的優化設計，我們可以為未來設計大型高效光捕捉系統提供一些有價值的指引。

關鍵字：光合作用系統 II、激發能轉移、光捕捉系統、能量曲面

doi:10.6342/NTU202301637

doi:10.6342/NTU202301637

Abstract

Photosystem II (PSII) relies on a large antenna complex to collect sufficient light energy to power its reaction centers (RCs). In this light harvesting process, molecular excitation must pass through the fluctuating energy surface where the static disorder perturb site energies, and overcome unfavorable entropic effects to be transferred from the large antenna to the much smaller RC with low energy loss. It is thus of significant importance to uncover the strategies that the nature applied to achieve the remarkably high quantum efficiency of PSII under the constrains. To this end, we constructed a coarse-grained model for exciton energy transfer in PSII, which allows us to establish an effective internal energy surface for excitation energy transfer in the PSII. We found that the energy landscape exhibits timescale separation characteristics among the clusters, which suppresses the entropic effect and facilitates the energy transfer to the RC. Further investigation revealed that the energy surface is optimized for efficient light harvesting and tolerating static disorder of site energy by using a specifically designed energy gradient along the

doi:10.6342/NTU202301637

main energy-transfer pathways and utilization of thermal energy to overcome the barriers. The optimal energy landscape for EET in the PSII provides important insight towards how to achieve highly efficient energy harvesting in a large and fluctuating system.

Keywords: PSII, EET, light harvesting system, energy surface

doi:10.6342/NTU202301637

Contents

Page

Verification Letter from the Oral Examination Committee **i**

Acknowledgements **iii**

摘要 **v**

Abstract **vii**

Contents **ix**

List of Figures **xiii**

List of Tables **xix**

Denotation **xxi**

Chapter 1 Introduction **1**

1.1 Light harvesting process in PSII 1

1.2 The constraints for light harvesting in PSII-sc 4

1.3 The EET dynamics in PSII-sc 7

1.4 Theorical Simulation of EET dynamics in PSII 8

1.5 The outline of this work 9

Chapter 2 Theoritical description of EET dynamics in photosynthetic system **13**

2.1 Model Hamiltonian 14

doi:10.6342/NTU202301637

2.2 Construction of effecitve Hamiltonian 18
2.3 Conbined Generalized Föster and modified Redfield method 19
2.4 Simulation of absorption spectrum 22
2.5 Simulation of migration time 23
2.6 Summary 24

Chapter 3 Construction of effective model and model validation 27

3.1 Construction of effective Hamiltonian 28
3.2 Spectral density 29
3.3 Fitted site energies 30
3.3.1 Slow EET dynamics in LHCII 35
3.4 Model validation for EET dynamics in PSII-sc 40
3.4.1 Migration time 41
3.5 Summary 42

Chapter 4 The effective internal energy surface in PSII-sc 43

4.1 Static disorder effect in light harvesting 44
4.2 Effective internal energy surface of PSII-sc 47
4.2.1 Construction of effective internal energy surface 49
4.2.2 High barriers in effective internal energy surface 53
4.3 Timescale separation on EET dynamics in PSII-sc 56
4.3.1 EET dynamics in upper side of PSII-sc 57
4.3.2 Energy transfer trajectories to RC 60
4.4 Summary 63

doi:10.6342/NTU202301637

Chapter 5 Inter PSII-sc EET on the thylakoid membrane 65

5.1 The crystal parameters of PSII-scs on the thylakoid membrane 65

5.2 Migration time between two adjacent PSII-scs 67

5.2.1 Low light adaptive condition 69

5.2.2 High light adaptive condition 72

5.3 Summary 78

Chapter 6 The factors govering the QY of light harvesting 79

6.1 Site energies effect on QY 80

6.2 The level of static effect on QY 85

6.3 Excitonic coupling effect on QY 86

6.4 Summary 91

Chapter 7 Conclusion 93

References 95

doi:10.6342/NTU202301637

doi:10.6342/NTU202301637

List of Figures

1.1 Illustration of the crystal structure of PSII-sc 1

1.2 (a) The protein conformation of PSII supercomplex (PDB: 5XNL) (b) The alignment of pigments and labels of subunits in PSII supercomplex (Chl a is labled in green, Chl b is labled in blue, and Phe is labled in purple) . . 3

2.1 The illustration of the Föster interaction and the Dexter interaction 16

2.2 (a) The distribution of distances between pigments in PSII-sc (b) A part of distribution of distances between pigments in PSII-sc 17

2.3 Illustration of domains of system Hamiltonian 19

2.4 Illustration of two path for exciton in PSII-sc 24

3.1 The spectra density for all site in PSII 30

3.2 (a) The location of RC in PSII-sc, RCs are labeled in orange. (b) Simulated (blue curve) and experimental(red curve) OD as a function of wavelength for the RC complex. The black sticks represent the peak positions and oscillator strengths of the exciton states 32

3.3 (a) The location of CP43 in PSII-sc, CP43s are labeled in orange. (b) Simulated (blue curve) and experimental (red curve) OD as a function of wavelength for the CP43 complex. The black sticks represent the peak positions and oscillator strengths of the exciton states 33

3.4 (a) The location of CP47 in PSII-sc, CP47s are labeled in orange. (b) Simulated (blue curve) and experimental (red curve) OD as a function of wavelength for the CP47 complex. The black sticks represent the peak positions and oscillator strengths of the exciton states 34

doi:10.6342/NTU202301637

3.5 (a) The location of LHCII monomer in PSII-sc, LHCII monomer (LHCII-M and LHCII-S) are labeled in orange. (b) Simulated (blue curve) and experimental (red curve) OD as a function of wavelength for the LHCII monomer. The black sticks represent the peak positions and oscillator strengths of the exciton states 35

3.6 The population dynamics of 14 Chl sites in LHCII monomer after the exciton states in 650 ± 1 nm are excited 37

3.7 (a) The location of CP29 in PSII-sc, CP29s are labeled in orange. (b) Simulated (blue curve) and experimental (red curve) OD as a function of wavelength for the CP29 complex. The black sticks represent the peak positions and oscillator strengths of the exciton states 38

3.8 (a) The location of CP26 in PSII-sc, CP26s are labeled in orange. (b) simulated (blue curve) and experimental (red curve) OD as a function of wavelength for the CP26 complex. The black sticks represent the peak positions and oscillator strengths of the exciton states 39

3.9 (a) The location of CP24 in PSII-sc, CP24s are labeled in orange. (b) simulated (blue curve) and experimental (red curve) OD as a function of wavelength for the CP24 complex. The black sticks represent the peak positions and oscillator strengths of the exciton states 40

4.1 The distribution of the QY of 1000 realizations 45

4.2 (a) Distribution of average L_D of exciton states from 1000 realization (b) Standard deviation of L_D - average L_D 46

4.3 The distribution of site energies of pigments of 1000 realizations 47

4.4 (a) The effective rate (in ps^{-1}) between clusters in PSII-sc and (b) the location of pigments in each clusters and in PSII-sc. Note: this picture is done by my coworker, Yun-Chung Yang 48

4.5 Illustration of the relation between $\Delta\Delta F^{\ddagger}_{BA}$ and $\Delta F^{\ddagger}_{BA}$ 51

4.6 Illustration of the relation between $\Delta\Delta U^{\ddagger}_{BA}$ and $\Delta\Delta F^{\ddagger}_{BA}$ 52

doi:10.6342/NTU202301637

4.7 Averaged effective internal energy surface of the clusters on the circular network in PSII-sc. (a) effective internal energy surface along the upper-circle path from RC_1 to RC_2 (b) effective internal energy surface along the lower-circle path from RC_2 to RC_1 Note that the cluster 8, 9, 12, and 17 are not in the circular network, so we remove them for clarity (The red states indicate the states with high effective transition state energy) . . . 55

4.8 The EET dynamics in PSII-sc within 200 ps population time, after we populate the subunit in upper left side of PSII-sc (a) LHCII-M_1-1 (b) LHCII-M_1-2 (c) LHCII-M_1-3 (d) $CP24_1$ (e) $CP29_1$ (f) $CP47_1$ ((Note that the exciton in RC_1 (RC_2) quickly transfer to RP_1 (RP_2), so we remove the EET dynamics of RC_1 and RC_2 for clarity) 58

4.9 The EET dynamics in PSII-sc within 200 ps population time, after we populate the subunit in upper right side of PSII-sc (a) LHCII-S_2-1 (b) LHCII-S_2-2 (c) LHCII-S_2-3 (d) $CP26_2$ (e) $CP43_2$ (Note that the exciton in RC_1 (RC_2) quickly transfer to RP_1 (RP_2), so we remove the EET dynamics of RC_1 and RC_2 for clarity) 59

4.10 Energy transfer trajectories of the effective center of population from 0 ps to 200 ps (The times of circle labels in path are 0, 50, 100, 200 ps) (Both RC_2 and RC_1 contribute to the QYs. However, to ensure clarity in the visualization, if the ratio of high QY and low QY is larger than 2, we ignore the minor path.) 61

5.1 The arrangement of PSII-scs 66

5.2 The comparison of alignment of PSII-scs in experimental results and in our model (a) at low light adaptive (b) at high light adaptive 67

5.3 (a) the structure of two connecting PSII-sc along the $\boldsymbol{b} - \boldsymbol{a}$ direction (b) as the exciton forms, it transfers to RC_A and to RC_B (c) the plausible paths for exciton are transferring to RC_A, RC_B, and stimulated emission of exciton 68

doi:10.6342/NTU202301637

5.4 Illustration of exciton migration to RC_A and RC_B (a) the antenna in the blue region is populated (b) the antenna in the green region is populated (c) the migration time between the antenna in the blue region and that in the green region 69
5.5 The two PSII-sc units at low light adaptive condition aligned along (a) $\boldsymbol{a}$ direction (b) $\boldsymbol{b}$ direction (c) $\boldsymbol{b} - \boldsymbol{a}$ direction 70
5.6 Illustration of plausible path for EET at low light adaptive 72
5.7 The two PSII-sc units at hight light adaptive condition aligned along (a) $\boldsymbol{b}$ direction (b) $\boldsymbol{b} - \boldsymbol{a}$ direction 73
5.8 Illustration of plausible path for EET at high light adaptive 75
5.9 Illustration of exciton migrate to the others PSII-sc units in $\boldsymbol{a}$ direction . 76
5.10 (a) illustration of the exciton migrate from the first PSII-sc unit (b) L_{PSII} changes as the probability of exciton diffusing among PSII-sc units. The blue region is $L_{PSII} \pm \sigma$. 77
5.11 (a) illustration of the exciton migrate from the third PSII-sc unit (b) L_{PSII} changes as the probability of exciton diffusing among PSII-sc units. The blue region is $L_{PSII} \pm \sigma$. 78

6.1 Illustration of Path in the upleft side of PSII 81
6.2 Correlation between average site energies of cluster and effective internal energies of the clusters (y=0.56x-8037) 81
6.3 (a) The average QY for 1000 realization as a function of energy shift on the site energies in cluster 3(b) The average QY for 1000 realization as a function of energy shift on the site energies in cluster 10 82
6.4 Illustration of Path in the upright side of PSII 83
6.5 The average QY for 1000 realization as a function of energy shift on the site energies in cluster 6 84
6.6 The distribution of QY with different sets of site energies (a) original set (b) the site energies of Chl b are 15385 cm^{-1}/ the site energies of Chl a and Pheo are 14900 cm^{-1} (c) the site energies of all pigments are 14900 cm^{-1} 84

doi:10.6342/NTU202301637

6.7 The distribution of the QY with different σ_s (a) $0.5k_BT$ (b) $1k_BT$ (c) $2k_BT$ . . . 86
6.8 The distribution of excitonic couplings of total Hamiltonian and that of the original PSII-sc Hamiltonian 88
6.9 The changes of migration time to RC as the degree of coupling changing(the direction of green is reducing the degree, and the direction of blue is increasing the degree. The blue area represents the $\pm 2\sigma$) (ln(edges) is reference to the natural PSII-sc) 89

doi:10.6342/NTU202301637

doi:10.6342/NTU202301637

List of Tables

2.1 The timescale of internal conversion (fs) for B $\rightarrow$ Q_x, Q_x $\rightarrow$ Q_y, and B $\rightarrow$ Q_y of Chla and Chlb (B represents the soret band) 18

3.1 The fitted site energies (cm^{-1}) of pigments in RC 31

3.2 The fitted site energies (cm^{-1}) of pigments in CP43 32

3.3 The fitted site energies (cm^{-1}) of pigments in CP47 33

3.4 The fitted site energies (cm^{-1}) of pigments in LHCII monomer 34

3.5 The fitted site energies (cm^{-1}) of pigments in CP29 (Because 601 and 616 in CP29 doesn' t available in the previous work, the site energy of those sites are set to be 14900 cm^{-1} before fitted) 37

3.6 The fitted site energies (cm^{-1}) of pigments in CP26 (Site energies of CP26 use site energies of LHCII. Because site 609 is Chl a in CP26, which is Chl b in LHCII, the site energy of this site are set to be 14900 cm^{-1} before fitted) 38

3.7 The fitted site energies (cm^{-1}) of pigments in CP24 (Site energies of CP24 use site energies of LHCII.) 39

4.1 The QYs of RC_1 and RC_2 as each subunit in the upside side of PSII are excited 62

5.1 The fitted crystal parameter (Å) 67

5.2 The migration times at low light adaptive condition (ps) (the first value in table represent the average value, and the second value represent the σ value) 70

doi:10.6342/NTU202301637

5.3 The migration times at low light adaptive condition (ps) where decreasing the $\boldsymbol{a}$ and $\boldsymbol{b}$ by 3 Å (the first value in table represent the average value, and the second value represent the σ value) 71

5.4 The migration times at high light adaptive condition (ps) (the first value in table represent the average value, and the second value represent the σ value) 73

5.5 The migration times at high light adaptive condition (ps) where decreasing the $\boldsymbol{a}$ and $\boldsymbol{b}$ by 3 Å (the first value in table represent the average value, and the second value represent the σ value) 74

6.1 Comparison of $\langle \tau_{mig} \rangle$ to RCs for different number of edges 90

doi:10.6342/NTU202301637

Denotation

PSII	photosystem II
PSII-cc	photosystem II core complex
PSII-sc	photosystem II supercomplex
OER	oxygen evolving reaction
QY	quantum yield
EET	excitation energy transfer
RC	reaction center
LHCII	light harvesting complex II
τ_{mig}	migration time
σ_s^e	relative error

doi:10.6342/NTU202301637

doi:10.6342/NTU202301637

Chapter 1

Introduction

1.1 Light harvesting process in PSII

Photosynthesis is a fundamental process converting light energy into chemical energy. Efficient light harvesting is critical for sustainable energy production, and it involves converting light energy into chemical potential energy to drive further chemical reactions. In higher plants, the photosystem II supercomplex (PSII-sc) is responsible for unit of the light harvesting process in the thylakoid membrane[1–3]. The crystal structure of PSII-sc is illustrated in Figure 1.1[4]. 2RC in the center and the other protein subunits are antenna.

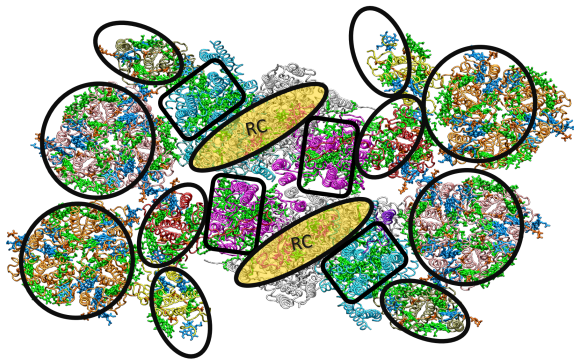

Figure 1.1: Illustration of the crystal structure of PSII-sc

doi:10.6342/NTU202301637

To accurately simulate the EET rate in PSII-sc, it is essential to have detailed alignment of pigments within the PSII-sc structure. The arrangement of pigments directly influences the EET rate. By having precise information about the pigment alignment, we can simulate and study the EET rate in PSII-sc. For higher accuracy in determining the EET rate we select, we selected the $C_2S_2M_2$-type PSII-sc from *Pisum sativum* at a resolution of 2.7 Å, which was determined using Cryo-EM techniques [4]. This crystal structure currently provides the highest resolution available for studying the PSII-sc.

To accurately obtain structural information about PSII-sc, it is indeed crucial to understand the composition of its subunits. The PSII-sc involves several subunits, with the PSII core complex (PSII-cc) being the fundamental building block. Notable subunits within the PSII-cc include the RC, CP43, and CP47. Additionally, the PSII-cc interacts with the light-harvesting complex II (LHCII) and additional protein subunits, such as CP29, CP26, and CP24, to form the complete PSII-sc structure. These subunits play vital roles in the assembly and functionality of PSII-sc, and several PSII-scs aggregates on the membrane [5].

Figure 1.2 a shows the conformational protein structure of PSII-sc, while Figure 1.2 b displays the alignment of pigments within the PSII-sc structure. The pigments found in PSII-sc include chlorophyll a (Chl a), chlorophyll b (Chl b), and pheophytin (Phe). The subunits of PSII-sc, namely RC, CP43, CP47, LHCII-M, LHCII-S, CP29, CP26, and CP24, are labeled accordingly. Due to the C_2 symmetry of the PSII-sc, the subunits on the left side are labeled with subscript 1, while those on the right side are labeled with subscript 2.

doi:10.6342/NTU202301637

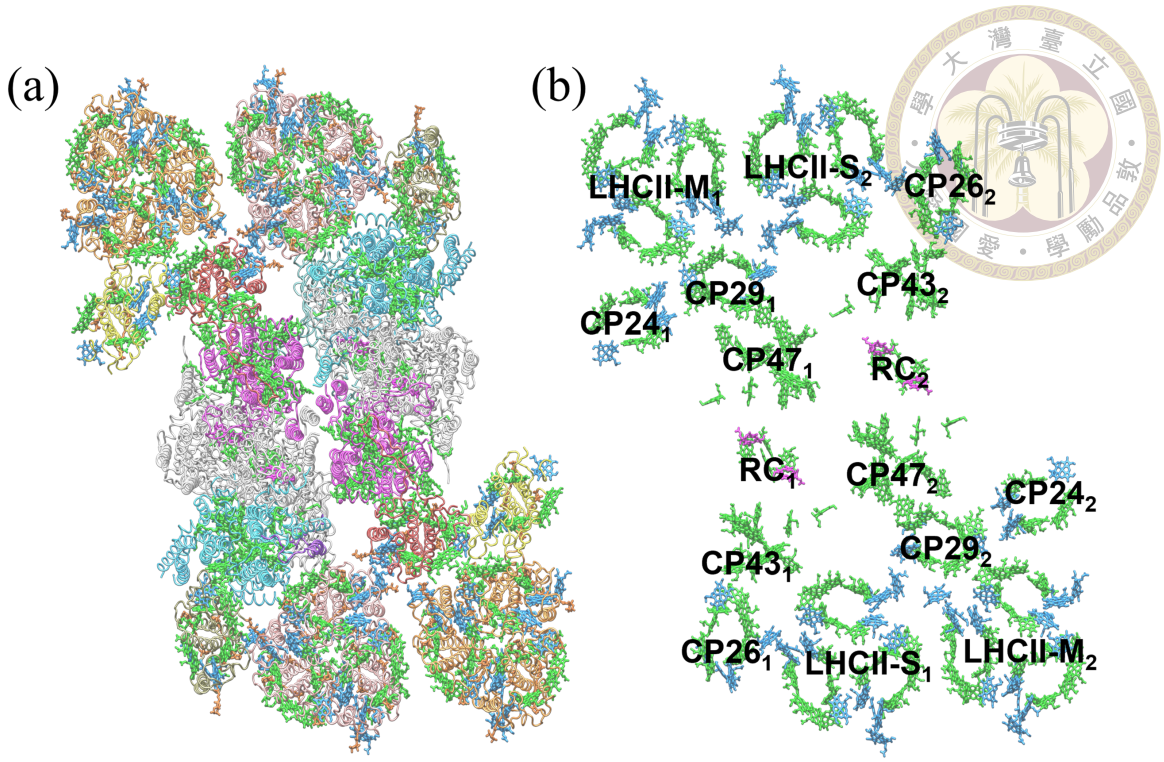

Figure 1.2: (a) The protein conformation of PSII supercomplex (PDB: 5XNL) (b) The alignment of pigments and labels of subunits in PSII supercomplex (Chl a is labled in green, Chl b is labled in blue, and Phe is labled in purple)

With this information about the alignment of pigments in PSII-sc, we have the ability to accurately simulate the EET rate. Previous studies have systematically investigated the EET and function of the PSII-cc [6]. Now, we are shifting our focus from the smaller PSII-cc system to the larger PSII-sc system. In the PSII-sc, the interplay between different subunits and the intricate arrangement of pigments leads to a higher level of complexity in energy transfer.

When solar radiation excites the pigments in the antenna of PSII, excitons are formed. These excitons then transfer to the reaction center (RC), where charge separation occurs, separating the excitons into electrons and holes. The electrons transfer to photosystem I (PSI) for $NADP^+$ reduction, while the holes transfer to the oxygen evolving complex for the oxygen evolving reaction (OER)[7].

doi:10.6342/NTU202301637

Because the light harvesting is an important process for photosynthesis, the fundamental mechanism of light harvesting in nature has been studied for decades, and the dynamics of each step in the light harvesting process have been analyzed. In light absorption of a pigment, the timescale for energy relaxation from the high excited states to first excited state (Qy band) has been assigned to several hundred femtoseconds. As such, higher excited states (sub-ps timescale) can be ignored when studying the excitation energy transfer (EET) in PSII (10 ps timescale) [1, 8, 9]. While coherence has been shown to play an important role in the EET and quenching process [10–19], some researchers have also proposed that it is less significant [20]. In addition to EET, the charge separation process has also been studied in terms of how the protein environment influences the process [21].

By investigating these processes, researchers try to learn "something" from light harvesting systems in nature [11]. However, many questions remain unanswered, including the mystery of how excitons efficiently transfer from a large antenna to a small RC in PSII supercomplex (PSII-sc).

1.2 The constraints for light harvesting in PSII-sc

PSII-sc faces two key constraints that hinder the efficient transfer of excitons to the RC. Firstly, the presence of large antenna complexes with numerous pigments introduces a significant number of states, which making it favorable to trap the exciton in antenna. Consequently, the transfer of excitons from the large antenna to the smaller RC becomes challenging. Secondly, the exciton energy in PSII-sc is utilized for driving the highly endothermal OER. As a result, the allowable energy loss in the EET process is limited,

doi:10.6342/NTU202301637

further complicating how to efficiently transfer excitons to RC.

Large antenna complexes is necessary for efficiently collect sufficient light energy, because chlorophyll molecules absorb only a few photons per second, which is insufficient for sustainably driving chemical reaction. In general, each RC connects with a large antenna (100 ∼ 1000 pigments) to collect light energy.[22] By connecting to antenna, the PSII-sc can capture additional photons and convert them into usable energy for the OER.

Because each RC connects with a large antenna, one challenge faced by PSII-sc is the unfavor entropy effect that comes with a large number of states in the antenna complexes while transferring the exciton to the small RC. This unfavor entropy effect had been found in experiment. In a notable experiment conducted by Scholes et al., the researchers investigated the role of entropy in rearranging the free energy of states within a system [23]. Their system consisted of two types of states: lower polariton states with lower electronic energy and dark states with higher electronic energy. Notably, the number of states in the dark state was significantly larger than the lower polariton state, which only had one state. Surprisingly, despite the dark state having higher electronic energy, Scholes et al. observed that when lower polaritons state was excited, the population spontaneously transferred to the dark states. This observation directly proves that the number of states reduces the free energy of dark states and effectively traps energy within them. Consequently, in the PSII-sc, where the small RC is connected to a large antenna complex comprising hundreds of states, there is a potential for excitons to become trapped in antenna due to the high entropy.

To overcome the entropy effect described earlier, purple bacteria, having another type of light harvesting system, has evolved a distinct strategy. This system consists of

doi:10.6342/NTU202301637

three types of subunits: LH2, LH1, and RC. The excitons within the LH2 subsequently pass through LH1 and are ultimately transferred to the RC. In purple bacteria, the LH2 units aggregate to form an antenna pool that efficiently absorbs photons, resulting in high entropy.

Interestingly, during this EET process from LH2 to RC, there is an energy loss of approximately $2k_B$T (twice the thermal energy). This significant energy difference between LH2 and RC enables the efficient transfer of excitation energy to the RC with a high quantum yield [24–26]. This energy gradient in purple bacteria's light harvesting system helps overcome the entropy-related challenges and ensures the efficient EET from antenna to RC.

Unlike purple bacteria, PSII-sc cannot employ the same strategy from the antenna to the RC. In PSII-sc, the excitation energy is required for driving the highly endothermal OER[27]. If a large amount of excitation energy is lost during the EET from the antenna to the RC, the exciton in the RC may not possess sufficient energy to drive the OER effectively. As a result, the excitons in PSII-sc struggle to overcome the entropy effect and not losing significant electronic energy.

To address these limitations, the energy landscape in PSII must employ alternative strategies to achieve high quantum efficiency[28, 29, 1] while considering the entropic effects and the need to minimize energy loss. Despite these challenges, PSII exhibits an impressive ability to achieve high quantum efficiency in the process of light harvesting. The design of the energy landscape to efficiently transfer exciton from a large antenna to a small RC in PSII-sc remains a mystery.

doi:10.6342/NTU202301637

1.3 The EET dynamics in PSII-sc

The high QY of light harvesting in the PSII-sc has sparked considerable interest in the research of EET within PSII-sc, leading to numerous experimental and simulation studies. Experimental studies[30–35] have utilized fluorescence spectrum and two-dimensional electronic spectroscopy to investigate EET in PSII-sc. The utilization of 2DES allows us to investigate changes in excitation energy distribution following different initial population scenarios, providing insights into the relaxation of excitons from high energies of excitonic states to lower lying excitonic states.

However, despite the advancements provided by 2DES, the complex dynamics of EET between chlorophylls within PSII-sc pose challenges for detailed analysis solely through experimental methods. The intricacy of PSII-sc, consisting of approximately 300 pigments, presents further hurdles in studying the spatial aspects of EET within the system and gaining a deeper understanding of its underlying physical mechanisms. Thus, theoretical modeling of EET in PSII-sc assumes a critical role in offering meaningful insights that complement experimental findings. Theoretical models enable a more comprehensive exploration of the intricate EET dynamics between chlorophylls, facilitating a deeper understanding of the processes driving energy transfer within PSII-sc.

Previous theoretical modeling of EET dynamics in PSII-sc has employed site energies and calculated couplings to simulate the energy transfer processes[36–39, 6]. Fleming and coworkers use structure-based models for light harvesting in PSII-sc and thylakoid membranes. These models exhibit rapid EET dynamics characterized by linear EET cascades in a single PSII supercomplex and one-dimensional diffusion-trapping in thylakoid membrane models. These models successfully describe experimental data on the dynamics of

doi:10.6342/NTU202301637

light harvesting in the respective systems.

Subsequently, Kreisbeck and Aspuru-Guzik applied numerically exact EET theory to the same PSII model, emphasizing the significance of non-equilibrium dynamics. While these insights are valuable, the models are based on approximated point dipole-point dipole interactions and highly averaged observables of EET dynamics, lacking specific structural details that explain the observed high quantum efficiency in nature.

The complexity of the full kinetic model for a system like the PSII-sc makes it challenging to obtain a clear view of the light harvesting process. Consequently, it is crucial to develop a theoretical approach that provides straightforward yet comprehensive temporal and spatial representations of EET dynamics in PSII to deepen our understanding. Further research focusing on the structural factors responsible for the diffusive characteristics observed in large and complex photosynthetic systems is essential for unraveling the mechanisms by which nature achieves efficient light harvesting.

1.4 Theorical Simulation of EET dynamics in PSII

To unravel the mystery behind the efficient light harvesting process in PSII-sc, the development of a model that accurately simulates the EET rates between exciton states is crucial. This model will provide valuable insights into the underlying mechanisms and allow for the calculation of EET rates.

A suitable approach for simulating EET rates in PSII-sc is the methodology proposed by van Grondelle, which provides a framework for calculating EET rates between exciton states and simulating the dynamics of EET [40]. This methodology enables a detailed investigation of the EET process within PSII-sc.

doi:10.6342/NTU202301637

In this methodology, two key parameters are considered for calculating the EET rates. The first parameter is the site energy of the pigment molecules, which can be obtained from previous literature, the work done by Renger et al. The second parameter is the excitonic coupling between pigments, which is strongly influenced by the arrangement and alignment of the pigments within PSII-sc.

The accuracy of the excitonic coupling directly affects the calculated EET rates between exciton states. Therefore, an deteiled structure of PSII-sc is crucial for determining the precise excitonic coupling and subsequently calculating the EET rates.

1.5 The outline of this work

The efficient energy transfer process in PSII-sc, where the exciton is transferred to the RC with a high QY of light harvesting, is truly remarkable considering the two limitations it faces: high entropy in the antenna and constraint of energy loss in light harvesting process. In this work, we are aim to uncover the specific design principles employed by PSII-sc for efficient light harvesting.

To investigate how PSII-sc achieves this high QY of light harvesting, we utilize the methodology proposed by van Grondelle, which involves calculating the EET rate in PSII-sc. We employ the Generalized Förster and modified Redfield methods, which are reliable approaches for accurately determining the EET rate in pigment-protein systems like PSII-sc.

To build up this model and calculate the EET rate, we utilize two key parameters: site energy and exciton coupling between pigments. The site energies are obtained from the literature, specifically from Renger's works. However, to improve the accuracy of our

doi:10.6342/NTU202301637

model, we adjust the site energies by fitting the experimental absorption spectrum of the subunits in PSII-sc. This shifting improve our model for more accurate EET rate in PSII-sc system. For calculating the electronic coupling between pigments, my coworker apply the TrEsp method based on the alignment of pigments in PSII-sc . This information helps in determining the strength of the interaction between pigments, which directly influences the EET rate.

After building up this model, we compare the simulated migration time with experimental results to validate our model. This comparison allows us to assess the accuracy and reliability of our model in capturing the dynamics of exciton transfer within PSII-sc. By validating our model against experimental data, we can gain confidence in the insights and predictions it provides regarding the efficient light harvesting process in PSII-sc.

With our reliable model for simulating the EET rate, we are capable of calculating the QY of PSII-sc. However, it is crucial to consider the impact of static disorder on the energy landscape during the EET process from the antenna to the RC. Static disorder arises from the vibrational modes of the proteins surrounding the pigments, leading to fluctuations in the site energy of the embedded pigments. Consequently, the site energies within PSII-sc vary across different realizations. So, we will systematically study static disorder effect on exciton states and QY in PSII-sc.

Next, to reveal how PSII-sc against the high entropy in antenna, we focus on the effective internal energy surface for the clustered PSII-sc system[10]. Initially, we select a specific EET rate matrix of a realization. However, the resulting EET rate matrix is highly complex and challenging to analyze directly. To address this issue, my coworker employs a clustering method to reduce the complexity of the EET rate matrix and obtain a

doi:10.6342/NTU202301637

more manageable representation. This clustering technique groups the pigments in PSII-sc into several clusters, allowing us to study the characteristics of the effective internal energy surface and EET dynamics based on this clustered representation.

Furthermore, because PSII-sc aggregate on the membrane, we investigate the potential impact of the presence of an additional PSII-sc on the QY. To assess investigation, we calculate the migration time and QY associated with the transfer of excitons from one PSII-sc complex to another. This analysis allows us to determine whether the interactions between the two PSII-sc enable efficient passage of excitons within the timescale relevant to light harvesting.

Following the construction of the effective internal energy surface for the clustered PSII-sc system, we now focus on manipulating the site energies and couplings within PSII-sc to gain insights into its unique characteristics. By examining the QY as an indicator, we aim to investigate the role of site energy and the choice of exciton couplings in enhancing the overall QY of PSII-sc. We also systematically vary the site energies associated with the pigments in PSII-sc. By exploring different configurations of site energies, we can assess their impact on the efficiency of energy transfer and ultimately the QY. we examine the influence of exciton couplings within PSII-sc. By carefully selecting and manipulating the couplings between pigments, we can evaluate their significance in efficient energy transfer and the QY.

Through our comprehensive analysis of the EET dyanmics in PSII-sc, our research unravel the intricate energy landscape of this complex system. By examining the site energies and static disorder within PSII-sc, we seek to uncover the design principles and strategies employed by nature for efficient light harvesting. The insights gained from

doi:10.6342/NTU202301637

our study have the potential to inspire the development of novel artificial light-harvesting systems, and advance our understanding of natural photosynthetic processes.

doi:10.6342/NTU202301637

Chapter 2

Theoritical description of EET dynamics in photosynthetic system

In this chapter, we will introduce the model Hamiltonian for constructing exciton states in PSII-sc, and explain the methodology for calculating the EET rate between these states. The model Hamiltonian consists of three components: the system Hamiltonian, the bath Hamiltonian, and the system-bath interaction.

After a model Hamiltonian is obtained, we apply two theories, namely the Generalized Föster theory[41] and the modified Redfield theory[42], to calculate the EET rate between the exciton states. In EET calculations, the challenge of dynamical localization[43] is a well-known phenomenon. To account for this phenomenon, a threshold is introduced on excitonic couplings. To divide the system Hamiltonian into several domains and determine the electronic couplings required for constructing the exciton states in our model. The Generalized Föster theory is utilized to calculate the EET rate between different domains, while the modified Redfield theory is employed for EET within the same domain. This approach enables us to accurately determine the rates of energy transfer between the exciton states, taking into consideration both inter-domain and intra-domain transfers.

doi:10.6342/NTU202301637

2.1 Model Hamiltonian

The model Hamiltonian for studying the EET in the pigment-protein complexes (PPC) involves three parts

$$H_m = H_s + H_b + H_{sb} \tag{2.1}$$

where H_s is system Hamiltonian, H_b is the bath Hamiltonian, and H_{sb} is the system-bath interactions.

We use Frenkel exciton model[44] to describe the system Hamiltonian H_s, and the Frenkel exciton Hamiltonian for PSII system containing N pigments is written as

$$H_s = \sum_{n=1}^{N} E_n |n\rangle\langle n| + \sum_{n\neq m} V_{nm} |n\rangle\langle m| \tag{2.2}$$

where $|n\rangle$ depicts the Q_y band excitation at nth pigment, E_n is the site energy (Q_y band transition energy) of $|n\rangle$, and V_{nm} is excitonic coupling between $|n\rangle$ and $|m\rangle$.

In the PPC, the H_{sb} describes the interaction between pigment and environment. The pigments are embedded in the protein, so there is an interaction between the protein and the pigment. As a result, the vibration of the protein is coupled to the excitation of the pigment. The H_b represents the modes of vibration in the environment of the pigments, and we use a series of independent harmonic oscillators to represent those protein vibrations.

$$H_b = \sum_{\xi} \hbar\omega_\xi \left\{ b_\xi^\dagger b_\xi + \frac{1}{2} \right\} \tag{2.3}$$

where ω_ξ is the vibrational frequency at ξth bath mode. The interaction between excitation

doi:10.6342/NTU202301637

and protein vibrations is described in the H_sb, which are given by

$$H_{sb} = \sum_{n=1}^{N} \sum_{\xi} \hbar\omega_\xi g_\xi^n (b_\xi^\dagger + b_\xi)|n\rangle\langle n| \tag{2.4}$$

where g_ξ^n describes the system-bath coupling of excitation transition at n pigment and normal mode at ξ th bath.

The system-bath couplings are described by the spectral density, which represents the density of states of the vibration modes weighted by these couplings. The spectral density is given by

$$J_{nm}(\omega) = \sum_{\xi} g_\xi^n g_\xi^m \delta(\omega - \omega_\xi) \tag{2.5}$$

If n = m, $J_{nn}(\omega)$ describes that the energy fluctuation of E_n because of the protein vibrations; if $n \neq m$, $J_{nm}(\omega$ describes the correlation between the fluctuation of E_n and that of E_m. We assume that $J_{nn}(\omega)$ is identical for any n, and the fluctuation of E_n and that of E_m are independent, so $J_{nm}(\omega) = 0$.

First, we explain the formation of electronic couplings between pigments. When multiple pigments (molecules that absorb light) are present in a system, they can interact with each other through electronic coupling, resulting in energy transfer between them. This interaction is known as electronic coupling, which arises from the overlap of the transition densities of the pigments. The Föster interaction and the Dexter interaction both contribute to the coupling between excited states.

doi:10.6342/NTU202301637

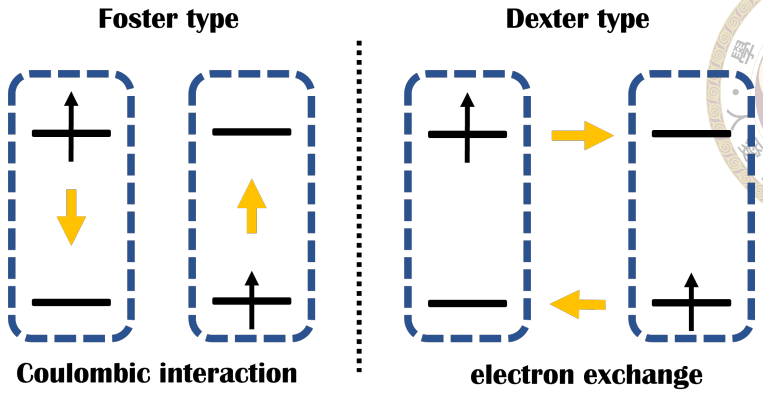

Figure 2.1: The illustration of the Föster interaction and the Dexter interaction

Figure 2.1 illustrates the difference between these two types of interactions. In the Föster interaction, the electron in the excited state of the first site relaxes to the ground state, while the electron in the ground state of the second site is excited to the excited state. The transfer of energy between the two sites is mediated by an interaction, such as a dipole-dipole interaction.

In the Dexter interaction, the electron in the excited state of the first site is transferred to the excited state of the second site, while the electron in the ground state of the second site is transferred to the ground state of the first site. The Dexter interaction relies on an orbital overlap to transfer the electron from one site to another. However, this interaction is not significant when the distance between the two excitations is larger than 10 Å.

doi:10.6342/NTU202301637

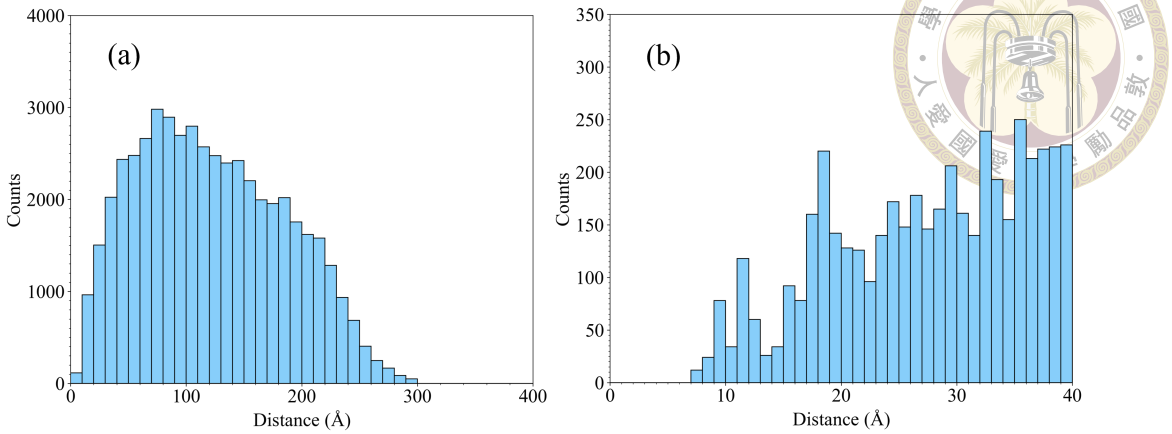

Figure 2.2: (a) The distribution of distances between pigments in PSII-sc (b) A part of distribution of distances between pigments in PSII-sc

We plot the distribution of distances between two pigments in PSII-sc, and show in Figure 2.2. This figure demonstrates that the 99.999% distances between pigments in PSII are greater than 10 Å, so we can disregard the Dexter interaction between excitations.

Then, we can utilize the Transition Charge from Electrostatic potential (TrEsp) method[45, 46] to calculate the excitonic coupling by using the alignment of the pigments in the crystal structure. The equation for calculating the coupling is given by Eq 2.6.

$$V_{nm} = \frac{f}{4\pi\epsilon_0} \sum_{i\in n, j\in m} \frac{q_i^{T,n} q_j^{T,m}}{|\boldsymbol{R_n^i} - \boldsymbol{R_m^j}|} \tag{2.6}$$

where q_i^T is the transition charge of atom i in pigment n at position $\boldsymbol{R_n^i}$, and f is a parameter describing the screening effect between pigments[47], which is given by

$$f = 2.68 \times (e^{-0.27d} + 0.54) \tag{2.7}$$

where d is the distance between pigment m and n with units in Å.

Second, we introducing the types of pigments present in PSII-sc and their excited

doi:10.6342/NTU202301637

states. The pigments in the PSII-sc mainly consist of Chla and Chlb, which absorb photon energy and transfer exciton energy to the RC. When these pigments are excited by sunlight, possible transitions from low to high transition energy include the Q_y, Q_x, and soret band.

If pigments are excited to Q_x and soret band, the sub-ps internal conversion from high energy states to Q_y occurs. Experimental results in Table 2.1 show that the relaxation time from high energy states to Q_y is on the timescale of 100 fs[8]. Compared to the timescale of the EET rate between Chla (10 ps), we can ignore the sub-ps internal conversion and only consider the Q_y transition in each site.

Table 2.1: The timescale of internal conversion (fs) for B $\rightarrow$ Q_x, Q_x $\rightarrow$ Q_y, and B $\rightarrow$ Q_y of Chla and Chlb (B represents the soret band)

	B $\rightarrow$ Q_x	Q_x $\rightarrow$ Q_y	B $\rightarrow$ Q_y
Chla	99.2	128	223
Chlb	57.9	208	267

2.2 Construction of effecitve Hamiltonian

We follow van Grondele's fomulation [40] to calculate EET rates between exciton states in the PSII-sc. In EET calculations and determining the exciton states, the dynamical localization of excitons in pigment-protein complexes poses a well-known challenge[43]. The coherence between excitations at pigments rapidly decays, causing the delocalized excitation through weak electronic coupling to transition into local excitation. To account for this decoherence phenomenon, we set a threshold on excitonic couplings to determine the H_s and exciton states in our model, and H_s is divided into several isolated domains to simulate this dynamical localization. We adopt threshold value (V_{cut} = 15 cm^{-1}) from van Grondelle[40], remove V_{nm} whose absolute value is equal to and less than 15 cm^{-1},

doi:10.6342/NTU202301637

and H_s is divided into several isolated domains, which shows in Figure 2.3.

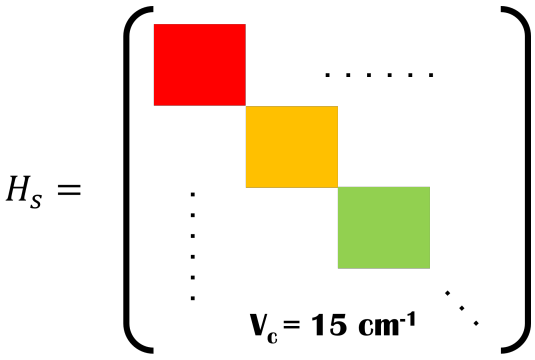

Figure 2.3: Illustration of domains of system Hamiltonian

We diagonalize this blocked H_s to obtain the exciton states, and the exciton state $|\alpha\rangle$ is the linear combination of the pigment states within the isolated domain M_A, which is described by

$$|\alpha\rangle = \sum_{n \in M_A} c_n^\alpha |n\rangle, \; E_\alpha = \sum_{n \in M_A} c_n^\alpha E_n \tag{2.8}$$

where E_α is the exciton energy of α state.

2.3 Conbined Generalized Föster and modified Redfield method

The methods for EET rate calculation within a domain and between domains are different. The selection of the method depends on the dominant factor that drives the EET[48]. For EET between exciton states in the same domain, the excitations at pigment use the couplings to form exciton states, and the EET is driven by site energy fluctuation. The EET rate can be calculated by the modified Redfield theory. For EET between exciton states in different domains, the interaction between the excitations is so weak that it cannot form a stable state. Therefore, the EET is driven by the weak excitonic coupling between

doi:10.6342/NTU202301637

the exciton states, and the EET rate can be calculated by the generalized Föster theory.

We use the combined generalized Föster[49–53, 41] and modified Redfield method[54, 42, 55] to calculate the rate of population transfer, and the general form for both theories is given by

$$R_{\beta\beta\alpha\alpha} = -2Re\left[\int_0^\infty {F_\alpha}^*(t)A_\beta(t)X_{\beta\alpha}(t)dt\right] \tag{2.9}$$

where $R_{\beta\beta\alpha\alpha}$ represents the population transfer rate from α state to β state, $F_\alpha(t)$ represent the fluorescence spectra of α state, $A_\beta(t)$ represents the absorption spectra of β state, and $X_{\beta\alpha}(t)$ represents the interaction part from perturbation terms. The fluorescence and absorption spectra are described by

$$F_\alpha(t) = \exp\{-i(\omega_\alpha - \lambda_{\alpha\alpha\alpha\alpha})t - g^*_{\alpha\alpha\alpha\alpha}(t)\} \tag{2.10}$$

$$A_\beta(t) = \exp\{-i(\omega_\beta + \lambda_{\beta\beta\beta\beta})t - g_{\beta\beta\beta\beta}(t)\} \tag{2.11}$$

where ω_α represents the transition frequency at α state, $\lambda_{\alpha\alpha\alpha\alpha}$ represents the reorganization energy at α state, and $g_{\alpha\alpha\alpha\alpha}(t)$ represents the line shaped function at α state. Transition frequency ω_α is evaluated from E_α divided by $\hbar$,

$$\omega_\alpha = \frac{E_\alpha}{\hbar} \tag{2.12}$$

With the spectral density, the time correlation function $\ddot{g}$ (t) is evaluated by

$$\ddot{g}(t) = \int_0^\infty \{(1+n(\omega))J(\omega)e^{-i\omega t} + n(\omega)J(\omega)e^{i\omega t}\}d\omega \tag{2.13}$$

doi:10.6342/NTU202301637

$$n(\omega) = \frac{1}{\exp(\frac{\hbar\omega}{k_B T}) - 1} \tag{2.14}$$

and the time correlation function in the exciton basis is evaluated by

$$\ddot{g}_{\alpha\beta\gamma\delta}(t) = \sum_{n=1}^{N} c_n^{\alpha} c_n^{\beta} c_n^{\gamma} c_n^{\delta} \ddot{g}(t) \tag{2.15}$$

The line shape function in exciton state is defined by

$$g_{\alpha\beta\gamma\delta}(t) = \int_0^t \ddot{g}_{\alpha\beta\gamma\delta}(\tau)(t-\tau)d\tau \tag{2.16}$$

and the reorganization energy of exciton state is defined by

$$\lambda_{\alpha\beta\gamma\delta} = -\int_0^{\infty} Im[\ddot{g}_{\alpha\beta\gamma\delta}(\tau)]d\tau \tag{2.17}$$

For the EET within the same domain, the rate is calculated by modified Redfield approach and the interaction part is described by

$$X_{\beta\alpha}(t) = \exp[2g_{\alpha\alpha\beta\beta}(t) + 2i\lambda_{\alpha\alpha\beta\beta}t] \times$$
$$\{\ddot{g}_{\alpha\beta\beta\alpha}(t) - [\dot{g}_{\alpha\beta\beta\beta}(t) - \dot{g}_{\alpha\beta\alpha\alpha}(t) - 2i\lambda_{\alpha\beta\alpha\alpha}] \times [\dot{g}_{\beta\alpha\beta\beta}(t) - \dot{g}_{\beta\alpha\alpha\alpha}(t) - 2i\lambda_{\beta\alpha\alpha\alpha}]\} \tag{2.18}$$

For the EET between the different domains, the transfer rate is calculated by generalized Föster approach and the interaction part is described by

$$X_{\beta\alpha}(t) = \left| \sum_{n,m} c_n^{\alpha} V_{nm} c_m^{\beta} \right|^2 \tag{2.19}$$

doi:10.6342/NTU202301637

2.4 Simulation of absorption spectrum

This section introduce how to simulate the absorption spectrum and the spectra density in this effective model. To simulate the absorption spectrum, we consider that it results from linear response of exciton states in subunits[56], and we also take into account the uncertainty of states arising from exciton transfer between exciton states ($R_{\alpha\alpha\alpha\alpha}$)[57]. For the static disorder resulting from long-period fluctuations in site energies, we use MT19937[58], a type of Mersenne Twister pseudo-random number generator, to simulate those fluctuations. MT19937 has a long period 2^{19937}-1, which ensures that the disorders on each site energies are random enough to simulate the fluctuations in the large system with 318 sites. The absorption spectrum is given by

$$OD(\omega) \propto \omega \sum_{\alpha} \left\langle |\boldsymbol{\mu_\alpha}|^2 Re\left\{ \int_0^{\infty} \exp[i(\omega-\omega_\alpha)t - g_{\alpha\alpha\alpha\alpha}(t) - R_{\alpha\alpha\alpha\alpha}t]dt \right\} \right\rangle_s \quad (2.20)$$

where the $\langle \dots \rangle_s$ represents average of all realization from static disorder, where each site energy is sampled according to Gaussian distribution with center at E_n and width is 100 cm^{-1}.

$\boldsymbol{\mu_\alpha}$ represents the transition dipole moment of the α-th exciton state, which is given by

$$\boldsymbol{\mu_\alpha} = \sum_{n=1}^{N} c_n^{\alpha} \boldsymbol{\mu_n} \quad (2.21)$$

$R_{\alpha\alpha\alpha\alpha}$ represents the sum of all transfer rate from α state to the other states, which is given by

$$R_{\alpha\alpha\alpha\alpha} = -\sum_{\beta\neq\alpha} R_{\beta\beta\alpha\alpha} + k_{FL} \quad (2.22)$$

doi:10.6342/NTU202301637

where $k_{FL}$is fluorescence decay rate constants given by

$$k_{FL} = \frac{|\boldsymbol{\mu_\alpha}|^2}{|\boldsymbol{\mu_0}|^2} \times 0.5(\text{ns}^{-1}) \tag{2.23}$$

where $\boldsymbol{\mu_0}$ represents the average dipole moment of exciton states.

2.5 Simulation of migration time

In this section, we establish the procedure to calculate $\langle \tau_{mig} \rangle$ from outer antenna to RC, and compare the simulated $\langle \tau_{mig} \rangle$ to the previous assignments. $\langle \tau_{mig} \rangle$ is the average timescale for exciton transfer from antenna to RC, and it is controlled by the EET rate in PSII-sc. So, we can validate our model for describing the EET rate in PSII-sc by comparing $\langle \tau_{mig} \rangle$ based on our model to the simulated and experimental results in literature.

To obtain the $\langle \tau_{mig} \rangle$, we have the consider the static disorder effect on site energies. The static disorder affect the site energies in system Hamiltonian and the EET rate in PSII-sc, so the τ_{mig} at different realization is not identical. In this work, we calculate 1000 of τ_{mig} at 1000 different realizations, and average them to obtain the $\langle \tau_{mig} \rangle$.

To model the τ_{mig} from the antenna to RC, we sample a realization of system Hamiltonian, and calculate QY to obtain the the τ_{mig}. As the exciton forms in PSII-sc, the plausible paths for exciton is transferring to RC or disspated by stimulated emission, which are illustrated in Figure 2.4. As the result, the QY at a realization is the ratio of k_{mig} to $k_{mig} + k_{Fl}$, which is given by Eq 2.24.

doi:10.6342/NTU202301637

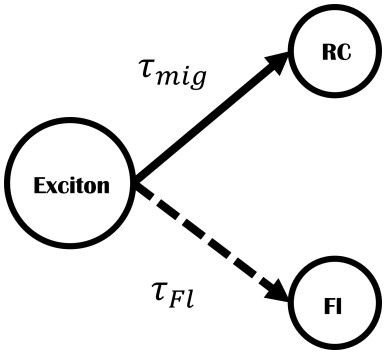

Figure 2.4: Illustration of two path for exciton in PSII-sc

$$QY = \frac{k_{mig}}{k_{mig} + k_{Fl}} \tag{2.24}$$

where k_{Fl} is the stimulated emission rate of Chla equal to 0.5 ns^{-1}, k_{mig} is the migration rate from the outer antenna to RC, and τ_{mig} is equal to $\frac{1}{k_{mig}}$.

2.6 Summary

This chapter presents construction of the model Hamiltonian and the methodology for studying EET in PSII-sc. The model Hamiltonian employed in this study comprises a system Hamiltonian, bath Hamiltonian, and system-bath interaction. The system Hamiltonian is described using the Frenkel exciton model, which considers site energies and excitonic couplings between sites.

To address the challenge of dynamical localization of exciton states, a threshold on excitonic couplings is set to determine the constitution of exciton states and divide the system Hamiltonian into several domains. The Generalized Foster theory is used to calculate the EET rate between different domains, while the modified Redfield theory is used for EET within the same domain.

doi:10.6342/NTU202301637

By employing this methodology, we are able to simulate the EET process in PSII-sc. More, we can analyze the factors that impact energy transfer within PSII-sc.

doi:10.6342/NTU202301637

doi:10.6342/NTU202301637

Chapter 3

Construction of effective model and model validation

We utilize the Frenkel exciton model to describe the system Hamiltonian, which incorporates both the site energies and the excitonic couplings between the sites. To determine the excitonic coupling among the pigments, we employ the TrEsp method, which calculates the Coulomb interactions between pairs of pigments. To enhance the accuracy of the site energies and account for system-bath interactions, we incorporate effective models and experimental spectra from the literature. This involves fitting the simulated spectrum to the experimental linear absorption spectrum.

We present a comprehensive analysis comparing the simulated spectra to the experimental spectra of each subunit, along with the fitted site energies for each subunit. By refining the site energies through fitting, we improve the effectiveness of the Hamiltonian in calculating EET rates in PSII-sc.

To validate the reliability of our model in describing EET processes in PSII, we compare our simulated EET dynamics with previous literature findings. Specifically, we focus on the PSII-sc and evaluate the average migration time from the outer antenna to the RC as

doi:10.6342/NTU202301637

a metric for model performance. We meticulously compare our simulated migration times with both experimental and simulated results available in the literature. Furthermore, we examine the detailed EET dynamics in the LHCII monomer by analyzing the long-time decay of the special a604 state. This analysis provides additional validation for our model.

To further assess the accuracy of our model, we investigate the lowest energy states in each protein subunit of the PSII-cc, which align with previously established assignments. By demonstrating consistency with known assignments, we strengthen the confidence in our model's reliability.

3.1 Construction of effective Hamiltonian

To construct an accurate model Hamiltonian for the EET in the entire PSII-sc, we determine the excitonic couplings and site energies based on experimental and simulated results from literature. We utilize the alignment of pigments in the crystal structural to evalue the excitonic couplings, and we use effective models in literal to determine the site energies of each pigment. More, to improve the site energies in our model Hamiltonian, we simulate the absorption spectrum for each subunits in the PSII-sc and compare it to the experimental spectrum to determine the optimal set of site energies, spectral density, and level of static disorder.

In previous research, several effective models have been proposed for the subunits within the PSII-sc. To determine the site energies, we adopted effective models proposed by Renger and coworkers for RC[59], CP43[60], CP47[33], CP29[57], and LHCII monomer[61]. Since CP24, CP26, and LHCII monomer are homologous Lhcb proteins that compose the PSII-sc[62], we adopt the effective model of LHCII monomer for CP24

doi:10.6342/NTU202301637

and CP26.

However, we found that simple adoption of the site energies from their model, along with our calculated excitonic couplings, did not accurately reproduce the experimental absorption spectra of each subunit. To address this, we readjusted the site energies by fitting them to the linear absorption spectrum for each subunit. During the fitting process, we allowed the site energies to shift within a range of ± 100 cm^{-1} while keeping the site energies of pigments in the same order in site energies. The results of the spectra fitting and optimal site energies are presented in section 3.3. The site energies determined by spectral fitting are commonly used to construct effective models for pigment-protein complexes. They often are consistent with experimental spectra and dynamics well. Moreover, since the energies are obtained by fitting the spectra of the complex in a solution, these values are expected to more accurately reflect the properties of the complex in its natural state.

3.2 Spectral density

To determine the spectral density for all pigments, we combine the ohmic oscillator for low frequency modes and Brownian oscillator for high frequency modes to describe the spectral density $J(\omega)$ for all pigments. We adjust the parameters in ohmic oscillator and Brownian oscillator by fitting the linear absorption spectrum for each subunit. In the fitting process, we constrain the reorganization energy within $50 \sim 100$ cm^{-1} . The optimal spectral density is presented in Eq 3.1 and plotted in Figure 3.1.

doi:10.6342/NTU202301637

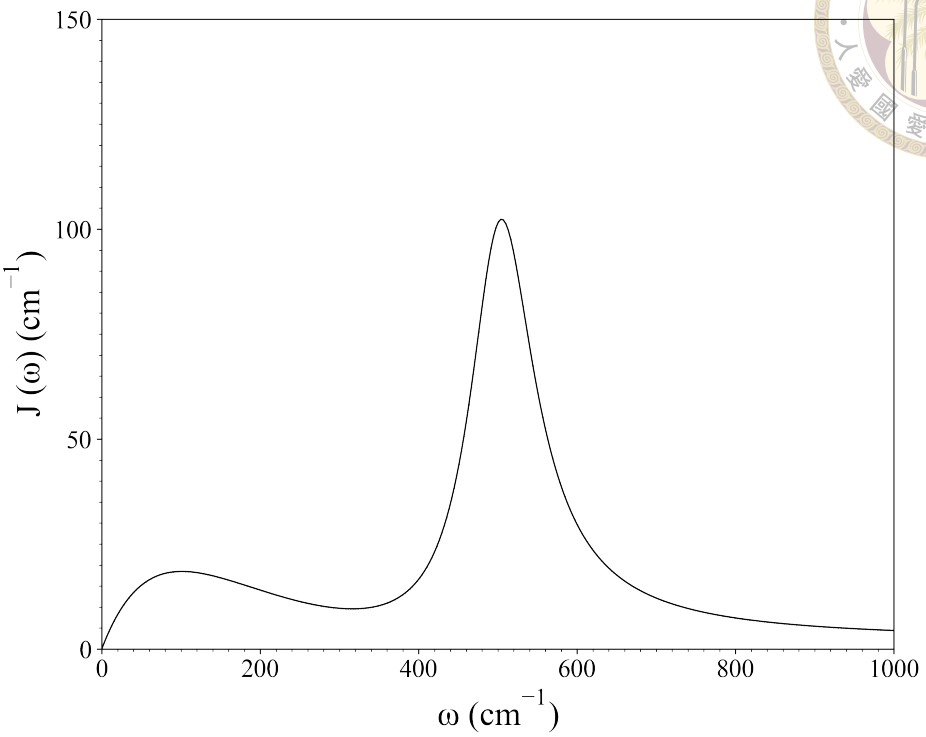

Figure 3.1: The spectra density for all site in PSII

$$J(\omega) = \gamma_0 \omega \, e^{-\frac{\omega}{\omega_0}} + \frac{4\gamma_1(\omega^2 + {\omega_1}^2){g_1}^2\omega^2}{[(\omega+\omega_1)^2 + {\gamma_1}^2][(\omega-\omega_1)^2 + {\gamma_1}^2]} \tag{3.1}$$

where $\gamma_0 = 0.5$, $\omega_0 = 100$ cm^{-1}, $\gamma_1 = 50$ cm^{-1}, $\omega_1 = 500$ cm^{-1}, and $g_1 = 0.1$.

3.3 Fitted site energies

In this section, we present the comparison of simulated and experimental absorption spectrum, and provide the fitted site energies in each subunits. The absorption spectrum provides direct information about the photophysical properties of a system, allowing us to roughly determine the transition energies of exciton states in the system. So, We modify the parameters in our model by comparing the experimental absorption spectrum of each

doi:10.6342/NTU202301637

complex with a simulated absorption spectrum, allowing us to improve our model and to more accurately calculate the EET rate.

We can simulate the absorption spectrum of each subunits in PSII-sc with our effective Hamiltonian. The subunits in PSII-sc are RC, CP43, CP47, LHCII monomer, CP29, CP26, and CP24. Note that LHCII-M is composed of three LHCII monomer, so does LHCII-S. To build up the effective Hamiltonian of subunits, we adopt the site energies from the previous effective Hamiltonian[60, 33, 59, 61, 57] and calculated the excitonic couplings by TrEsp method.

Note that simple adoption of site energies with the excitonic couplings does not reproduce the absorption spectrum, so we shift the site energies by comparing the simulated and experimental absorption spectra. In the fitting processing, we assume static disorders for all site are identical and equal to 100 cm^{-1}. The comparison of spectra is shown in Fig.3.2-3.9, and the fitted site energies are shown in Table.3.1-3.7. The pigments in RC are labeled by their numbering in the 2AXT crystal structure(traditional numbering), and other pigments in PSII-sc are labelled by their numbering in the 5XNL crystal structure.

RC subunit is located at the center of the PSII-sc, as depicted in Figure 3.2 (a). Within the RC, there are six Chl a pigments and two Phe. The fitted site energies of these pigments in the RC are listed in Table 3.1. Using this fitted site energies, simulated the absorption spectrum of the RC is similar to the the experimental absorption spectrum, as illustrated in Figure 3.2 (b). Chl_{D1} has the lowest site energy in RC[63, 37],

Site	P_{D1}	Chl_{D1}	Chl_{D2}	Phe_{D1}	Phe_{D2}	$Chlz_{D1}$	P_{D2}	$Chlz_{D2}$
E_n	14915	14729	14851	14894	14739	14902	14952	14992

Table 3.1: The fitted site energies (cm^{-1}) of pigments in RC

doi:10.6342/NTU202301637

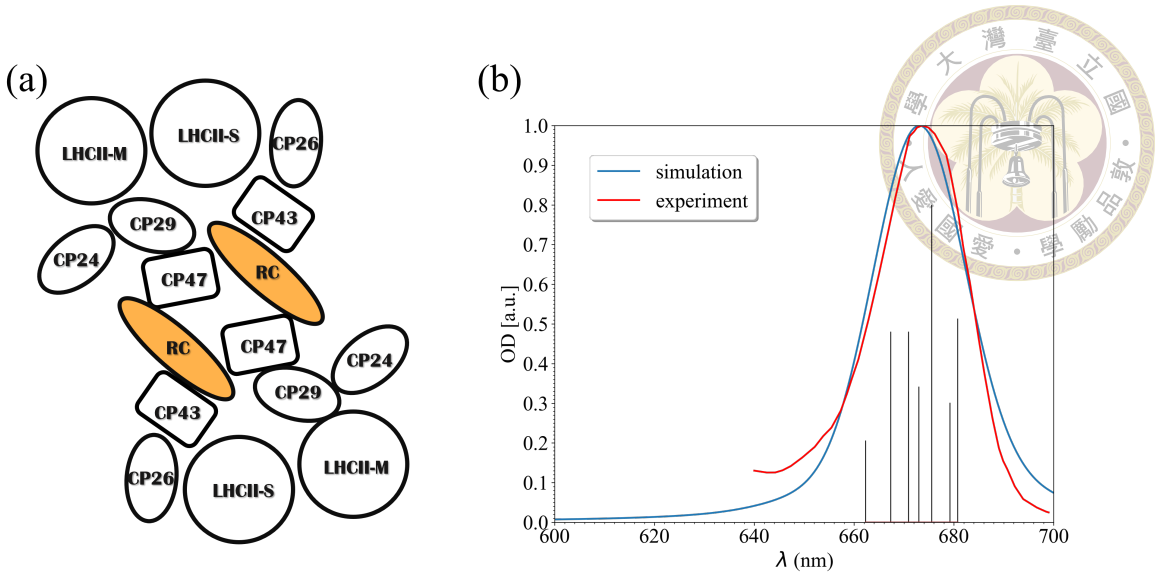

Figure 3.2: (a) The location of RC in PSII-sc, RCs are labeled in orange. (b) Simulated (blue curve) and experimental(red curve) OD as a function of wavelength for the RC complex. The black sticks represent the peak positions and oscillator strengths of the exciton states

CP43 subunit is adjacent to RC, as depicted in Figure 3.3 (a). Within the CP43, there are thirteen Chl a pigments. The fitted site energies of these pigments in the CP43 are listed in Table 3.2. Using this fitted site energies, simulated the absorption spectrum of the CP43 is similar to the the experimental absorption spectrum, as illustrated in Figure 3.3 (b).Site 504 has the lowest site energy in CP43[33, 44, 64],

Site	501	502	503	504	505	506	507
E_n	14,955	15,060	14,887	14,789	14,960	14,937	14,865
Site	508	509	510	511	512	513	
E_n	14,932	14,865	14,942	14,865	14,928	14,947	

Table 3.2: The fitted site energies (cm^{-1}) of pigments in CP43

doi:10.6342/NTU202301637

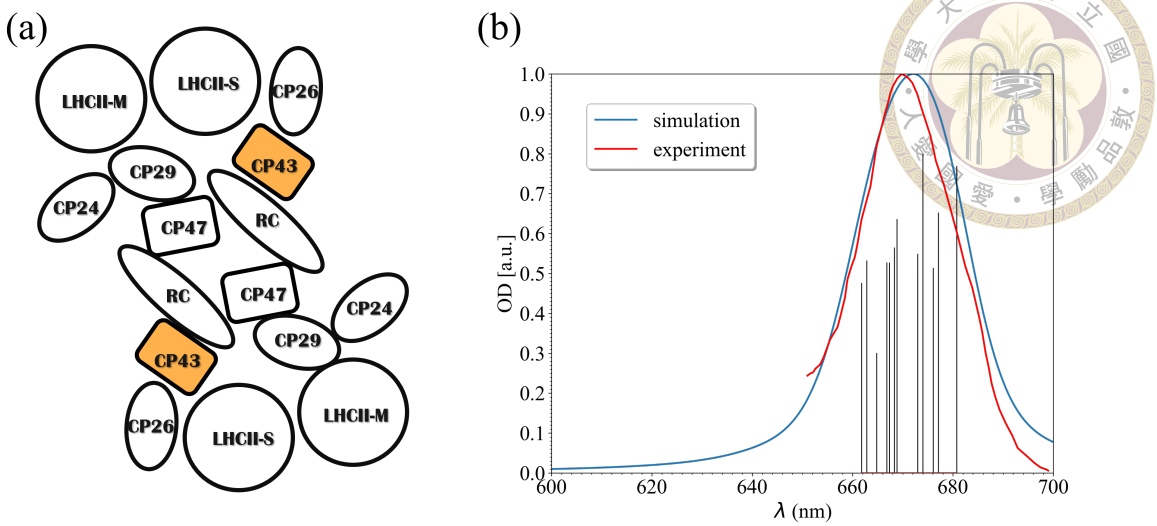

Figure 3.3: (a) The location of CP43 in PSII-sc, CP43s are labeled in orange. (b) Simulated (blue curve) and experimental (red curve) OD as a function of wavelength for the CP43 complex. The black sticks represent the peak positions and oscillator strengths of the exciton states

CP47 subunit is adjacent to RC, as depicted in Figure 3.4 (a). Within the CP47, there are sixteen Chl a pigments. The fitted site energies of these pigments in the CP47 are listed in Table 3.3. Using this fitted site energies, simulated the absorption spectrum of the CP47 is similar to the the experimental absorption spectrum, as illustrated in Figure 3.4 (b). Site 617 has the lowest site energy in CP47[65, 64].

Site	602	603	604	605	606	607	608	609
E_n	14778	15000	14903	14994	14858	14992	15076	14928
Site	610	611	612	613	614	615	616	617
E_n	14938	15152	14730	15025	14980	14910	14968	14602

Table 3.3: The fitted site energies (cm^{-1}) of pigments in CP47

doi:10.6342/NTU202301637

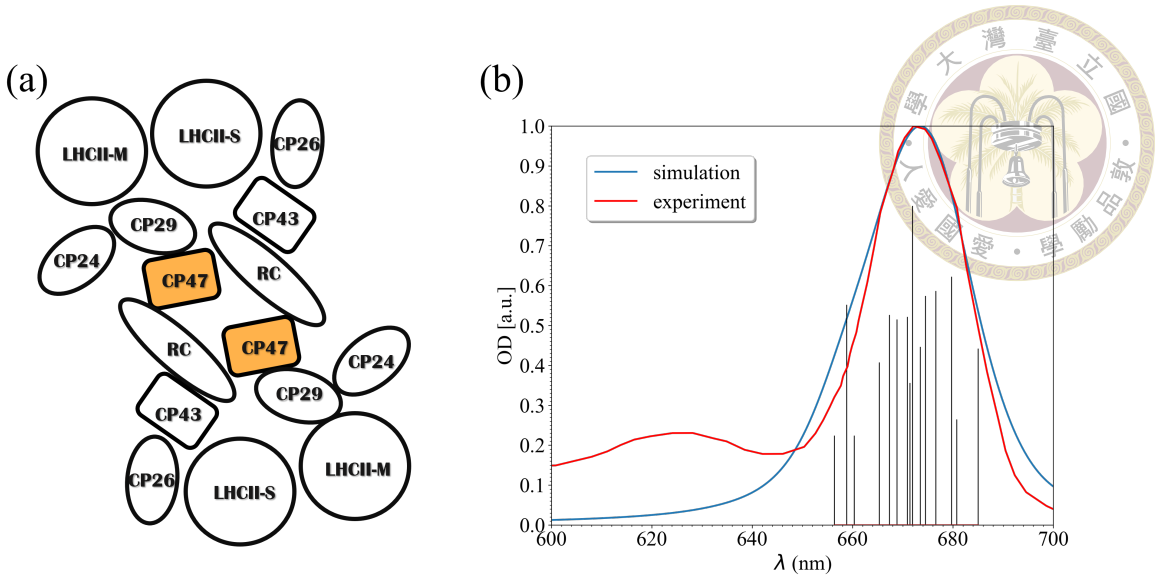

Figure 3.4: (a) The location of CP47 in PSII-sc, CP47s are labeled in orange. (b) Simulated (blue curve) and experimental (red curve) OD as a function of wavelength for the CP47 complex. The black sticks represent the peak positions and oscillator strengths of the exciton states

LHCII monomer subunit is the building block of LHCII-M and LHCII-S. LHCII-M (LHCII-S) is composed of three LHCII monomer. LHCII-M and LHCII-S are located at the boundary of PSII-sc, as depicted in Figure 3.5 (a). Within the LHCII monomer, there are eight Chl a pigments and Chl b pigments. The fitted site energies of these pigments in the LHCII monomer are listed in Table 3.4. Using this fitted site energies, simulated the absorption spectrum of the LHCII monomer is similar to the the experimental absorption spectrum, as illustrated in Figure 3.5 (b).

Site	601	602	603	604	605	606	607
E_n	15332	15030	14923	14725	15375	15321	15308
Site	608	609	610	611	612	613	614
E_n	15300	15395	14695	15048	15036	14756	15036

Table 3.4: The fitted site energies (cm^{-1}) of pigments in LHCII monomer

doi:10.6342/NTU202301637

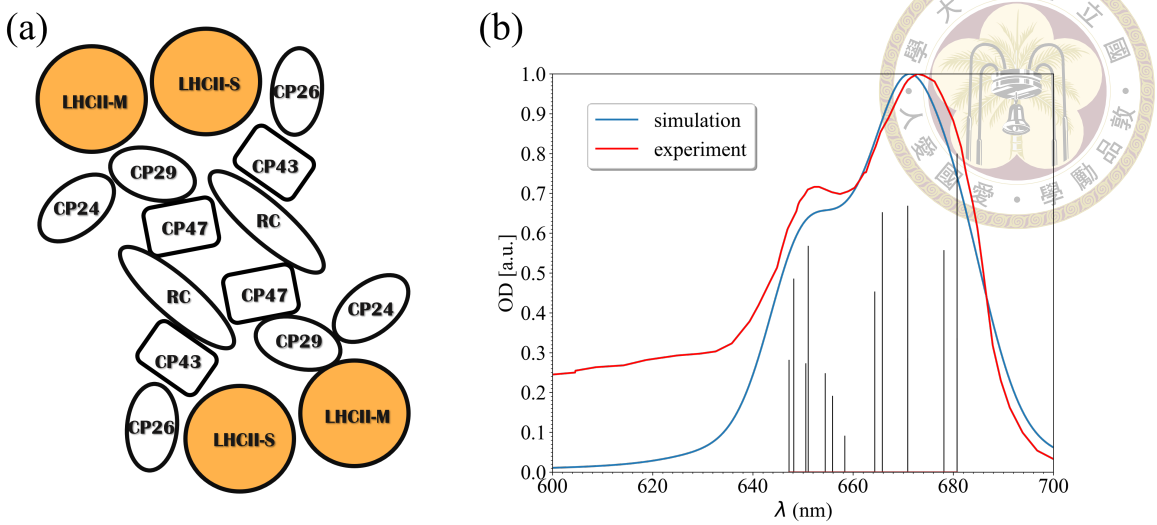

Figure 3.5: (a) The location of LHCII monomer in PSII-sc, LHCII monomer (LHCII-M and LHCII-S) are labeled in orange. (b) Simulated (blue curve) and experimental (red curve) OD as a function of wavelength for the LHCII monomer. The black sticks represent the peak positions and oscillator strengths of the exciton states

3.3.1 Slow EET dynamics in LHCII

In this sub-section, we compare the simulated EET dynamics in the LHCII monomer based on our model to van Grondelle's previous work. Additionally, we examine the lowest energy site of subunits in PSII-cc. To validate our effective model for the EET dynamics in subunit, we utilize the slow EET dynamics in LHCII monomer as reference. From van Grondelle's previous work, they found the slow equilibrium process between site 604 and other Chl a[40]. So, we use this as reference to validate our model.

We simulate EET dynamics in LHCII monomer by a representative Hamiltonian selected from a pool of 1000 realizations. Due to the presence of static disorder, the EET dynamics can exhibit variations across different realizations. To capture the dominant dynamical characteristic observed in most realizations, we utilized the relative error (σ^e) as a criterion, and choose the realization with lowest σ^e as the representative Hamiltonian.

doi:10.6342/NTU202301637

σ_s^e represents the relative error between the EET dynamics at the s realization and the average EET dynamics. In each realization, we determine the initial population of exciton states using Equation 3.5, and calculate the populations of sites at 20 ps. σ_s^e is then computed using Eq. 3.2.

$$\sigma_s^e = \sum_{n=1}^{14} \frac{|P_n^s - P_n^{avg}|}{\sigma_n} \tag{3.2}$$

where P_n^s is the population of n site at sth realization, P_n^{avg} is the average population of n site and calculated by Eq.3.3, and σ_n is the standard deviation of population of n site and calculated by Eq. 3.4.

$$P_n^{avg} = \frac{1}{1000} \sum_{s=1}^{1000} P_n^s \tag{3.3}$$

$$\sigma_n = \sqrt{\frac{1}{1000} \sum_{s=1}^{1000} (P_n^s - P_n^{avg})^2} \tag{3.4}$$

We reproduce the long time decay between site 604 and other Chla in LHCII monomer based on this representative Hamiltonian. We populate the exciton states in representation Hamiltonian within 650 $\pm$ 1 nm with Eq. 3.5, and the EET dynamics is shown in Fig.3.6. Similarly, we observe that site 604 has a relatively slow decay in a 10 ps timescale. This means that the EET from site 604 to other Chla is relatively slow, which is in excellent agreement with previous model.[40] This result shows that our effective model calculates the accurate EET rate within a subunit.

doi:10.6342/NTU202301637

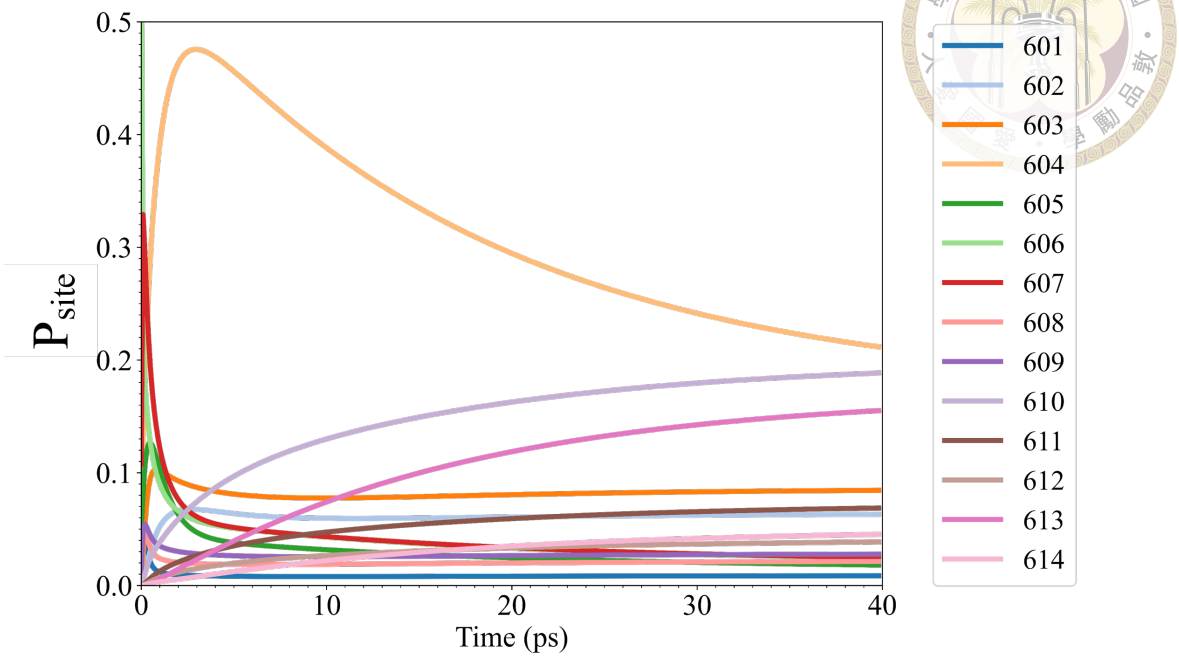

Figure 3.6: The population dynamics of 14 Chl sites in LHCII monomer after the exciton states in 650 ± 1 nm are excited

CP29 subunit is adjacent to CP47 and LHCII monomer, mediates the exciton from LHCII to CP47, as depicted in Figure 3.7 (a). Within the CP29, there are ten Chl a pigments and four Chl b pigments. The fitted site energies of these pigments in the CP29 are listed in Table 3.5. Note that the site energies of 601 and 616 in CP29 doesn't available in the previous work, so the site energy of those sites are set to be 14900 cm^{-1} before fitted. Using this fitted site energies, simulated the absorption spectrum of the CP29 is similar to the the experimental absorption spectrum, as illustrated in Figure 3.7 (b).

Site	601	602	603	604	606	607	608
E_n	14978	15023	14836	14821	15684	15349	15349
Site	609	610	611	612	613	614	616
E_n	15022	14992	14823	14956	14770	15579	14978

Table 3.5: The fitted site energies (cm^{-1}) of pigments in CP29 (Because 601 and 616 in CP29 doesn't available in the previous work, the site energy of those sites are set to be 14900 cm^{-1} before fitted)

doi:10.6342/NTU202301637

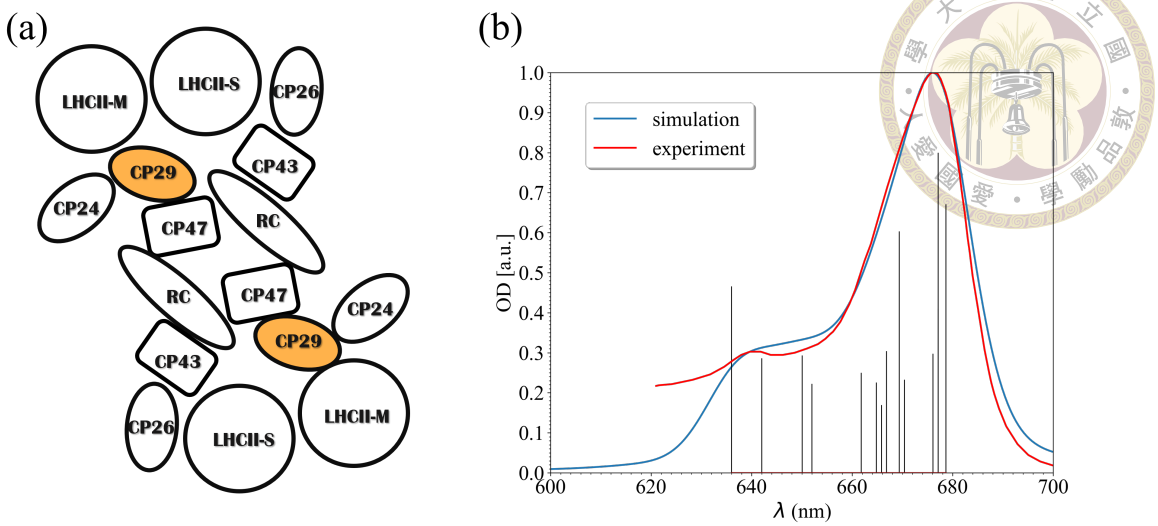

Figure 3.7: (a) The location of CP29 in PSII-sc, CP29s are labeled in orange. (b) Simulated (blue curve) and experimental (red curve) OD as a function of wavelength for the CP29 complex. The black sticks represent the peak positions and oscillator strengths of the exciton states

CP26 subunit is adjacent to CP43, as depicted in Figure 3.8 (a). Within the CP26, there are nine Chl a pigments and four Chl b pigments. The fitted site energies of these pigments in the CP26 are listed in Table 3.6. Note that we adopt the effective model of LHCII monomer for site energies in CP26. Site 609 is Chl a in CP26, which is Chl b in LHCII, so the site energy of this site are set to be 14900 cm^{-1} before fitted. Using this fitted site energies, simulated the absorption spectrum of the CP26 is similar to the the experimental absorption spectrum, as illustrated in Figure 3.8 (b).

Site	601	602	603	604	606	607	608
E_n	15329	15018	14870	14754	15295	15174	15132
Site	609	610	611	612	613	614	
E_n	14995	14693	15027	15040	14840	15030	

Table 3.6: The fitted site energies (cm^{-1}) of pigments in CP26 (Site energies of CP26 use site energies of LHCII. Because site 609 is Chl a in CP26, which is Chl b in LHCII, the site energy of this site are set to be 14900 cm^{-1} before fitted)

doi:10.6342/NTU202301637

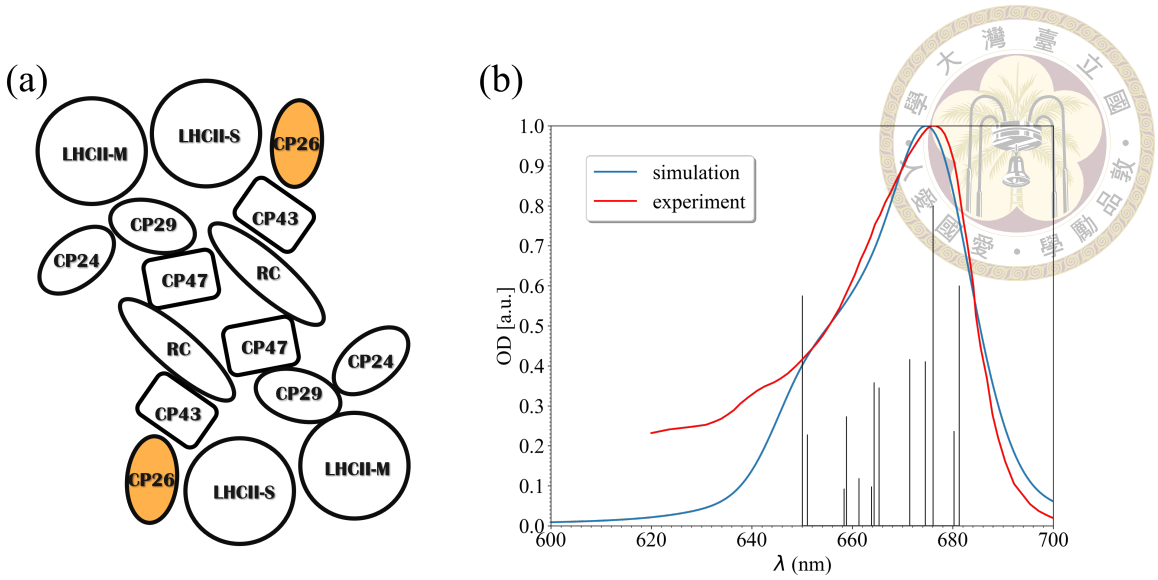

Figure 3.8: (a) The location of CP26 in PSII-sc, CP26s are labeled in orange. (b) simulated (blue curve) and experimental (red curve) OD as a function of wavelength for the CP26 complex. The black sticks represent the peak positions and oscillator strengths of the exciton states

CP24 subunit is adjacent to CP29, as depicted in Figure 3.9 (a). Within the CP24, there are six Chl a pigments and five Chl b pigments. The fitted site energies of these pigments in the CP24 are listed in Table 3.7. Note that we adopt the effective model of LHCII monomer for site energies in CP24. Using this fitted site energies, simulated the absorption spectrum of the CP24 is similar to the the experimental absorption spectrum, as illustrated in Figure 3.9 (b).

Site	601	602	603	604	606	607
E_n	15495	15000	14922	14850	15293	15234
Site	608	609	610	611	612	
E_n	15213	15560	14800	15020	15045	

Table 3.7: The fitted site energies (cm^{-1}) of pigments in CP24 (Site energies of CP24 use site energies of LHCII.)

doi:10.6342/NTU202301637

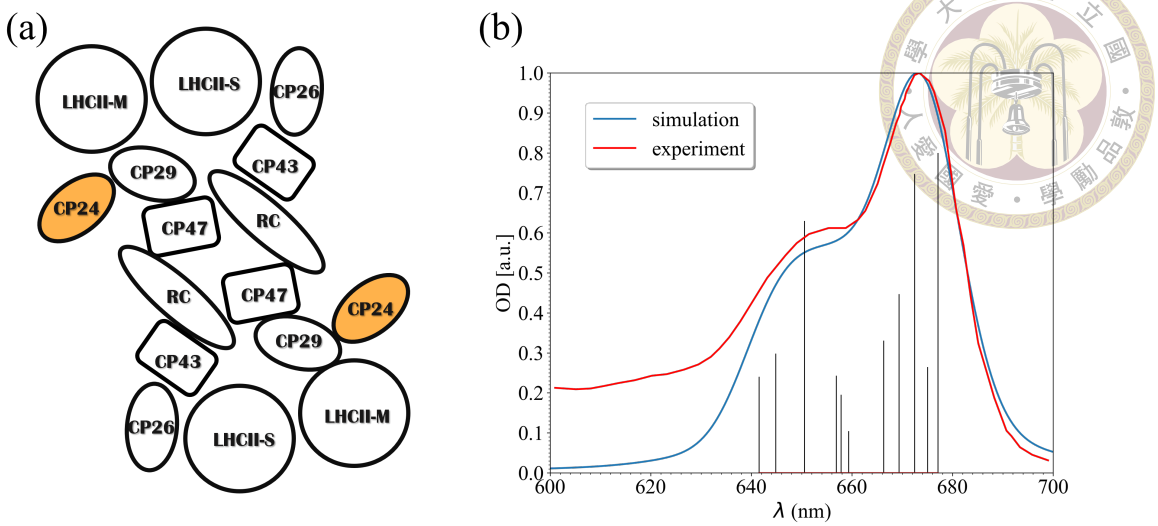

Figure 3.9: (a) The location of CP24 in PSII-sc, CP24s are labeled in orange. (b) simulated (blue curve) and experimental (red curve) OD as a function of wavelength for the CP24 complex. The black sticks represent the peak positions and oscillator strengths of the exciton states

Through the site energy fitting procedure, accurate site energies of each subunits were obtained that replicate the experimental absorption spectra. To further enhance the reliability of the calculated EET rate in PSII-sc based on the model, we validate the accuracy of the EET rate from the model with the following examinations.

3.4 Model validation for EET dynamics in PSII-sc

To validate our model to describe the EET in the PSII-sc, we compare average migration time ($\langle \tau_{mig} \rangle$) from outer antenna to RC with experimental and simulated results for overall EET in PSII-sc, check the special longtime decay of pigment 604 in LHCII for the detailed EET in LHCII monomer, and examine the lowest site energies in each protein subunit of PSII-cc to ensure consistency with previous assignments. With these validations, we have more confidence in the accuracy of the calculated EET rate based on this model.

doi:10.6342/NTU202301637

3.4.1 Migration time

We populate the exciton states in PSII-sc, and evaluate the QY by the following procedure. First, we construct the exciton states by the model Hamiltonian at a realization, and we assign the initial population of each exciton state according to their dipole strengths, which is given by,

$$P_{\alpha}^{ini} = \frac{|\mu_{\alpha}|^2}{\sum_i |\mu_i|^2} \tag{3.5}$$

where P_{α}^{ini} is the initial population at α-th exciton state, and $|\mu_{\alpha}|^2$ is the dipole strength of α state.

Second, we calculate the EET rate matrix to driven the EET dynamics in PSII-sc, and evaluate the QY. We generate the rate matrix for the EET from the antenna to the RC through the method described in section 2.3. To evaluate the QY, we include the P_{D1} and Chl_{D1} charge separation pathways in the RC in a phonological manner, with rate constants of 0.33 ps^{-1} and 1.43 ps^{-1}[6]. Those charge separation pathways is irreversible reaction path, so they can keep the population of exciton in RC, and we count the population in RC as QY.

To evaluate the QY, we drive the population transfer by the rate matrix for 10,000 ps. This is a long population time to ensure that the EET is complete. After all the exciton has decayed or keep in RC, we sum up the populations in RCs, and calculate the QY. To this end, we establish a procedure to calculate the QY at each realization and we estimate the τ_{mig} from the antenna to RC with the Eq.2.24.

We sample 1000 realizations and calculate the $\langle \tau_{mig} \rangle$. In this work, $\langle \tau_{mig} \rangle$ based on our effective model is 207 ps, which is in excellent agreement with the experimental

doi:10.6342/NTU202301637

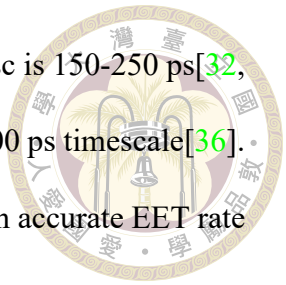

average lifetime. The experimental average lifetime of isolated PSII-sc is 150-250 ps[32, 66], and the time scale of simulated light harvesting in PSII-sc is $\sim$ 200 ps timescale[36]. This result shows that our effective model has the ability to produce an accurate EET rate in PSII-sc.

3.5 Summary

In this chapter, we present comparisons between the simulated spectrum and the experimental spectrum of each subunits, as well as the fitting of site energies for each subunit. By fitting the simulated spectrum to the experimental absorption spectrum, we improve the accuracy of our model Hamiltonian, which is used to calculate the EET rate in PSII-sc,.

We then proceed to validate our model for calculating the EET rate in PSII-sc by comparing the $\langle \tau_{mig} \rangle$ and EET dynamics in LHCII monomer with the previous findings in the literature. Our simulated results exhibit excellent agreement with the literature, indicating that our model is reliable in describing the overall EET in PSII-sc ($\langle \tau_{mig} \rangle$), as well as the EET dynamics in a subunit (slow EET rate between site 604 and other Chl a in LHCII monomer).

After establishing reliability of our model, we can now utilize it to investigate the impact of static disorder on the QY and exciton states of PSII. Additionally, we can explore the designs of PSII-sc for light harvesting.

doi:10.6342/NTU202301637

Chapter 4

The effective internal energy surface in PSII-sc

The pigments in PSII-sc exhibit static disorders in their site energies, which impacts the EET dynamics in PSII-sc. Therefore, it is important to examine the effect of static disorder on the QY first. In order to investigate this impact, we employ our effective model to 1000 different realizations of the PSII-sc Hamiltonian. Subsequently, we calculate the QY for each realization, enabling us to obtain a distribution of QY. This QY distribution allows us to study the influence of static disorder on the QY in PSII-sc. Then we select a proper EET rate matrix to simplify this complex EET rate matrix.

The number of states in PSII-sc is 318, which makes it challenging to analyze the complex EET rate matrix. To address this issue, my coworker applied the cluster method, to construct a Coarse-Grained (CG) model for PSII-sc. By clustering the EET rate matrix and grouping exciton states into clusters, the original 318×318 EET rate matrix was reduced to a more manageable 17×17 effective EET rate matrix.

We utilize the 17×17 effective EET rate matrix to construct the effective internal energy surface of the coarse-grained PSII-sc and investigate its characteristics. Our goal

doi:10.6342/NTU202301637

is to uncover the specific design strategies employed by PSII-sc to counteract the high entropy in antenna. By focusing exclusively on the effective internal energy component of PSII-sc, we can gain insights into the design strategies implemented to mitigate the impact of high entropy in the antenna.

Furthermore, to verify the characteristics observed in the effective internal energy surface, we perform EET dynamics simulations. By directly simulating the EET dynamics in PSII-sc, we can compare the observed characteristics on the energy surface with the actual EET processes from the antenna to RC_1 and RC_2. This validation through EET dynamics simulations enhances our confidence in the identified design strategies and their impact on the energy landscape of PSII-sc.

4.1 Static disorder effect in light harvesting

The site energies of pigments in PSII-sc are crucial in determining how excitons are transferred to the RC, and static disorder can perturb these energies over a long timescale, so it is important to study the influence of static disorder effect on QY. Static disorder refers to a fluctuation of site energy that occurs over a timescale longer than that of the energy transfer to the RC. Since static disorder can change the site energies in each realization, it is essential to investigate its effects on the QY of light harvesting and exciton states of PSII-sc. To accomplish this, we sampled 1000 realizations of the PSII-sc Hamiltonian, allowing us to study how static disorder affects the QY and exciton states comprehensively.

As previously mentioned, we sampled the PSII-sc Hamiltonian 1000 times to investigate the effects of static disorder on the QY and exciton states. In each realization, we populated the PSII-sc using equation 3.5 and calculated the QY at 10000 ps to ensure

doi:10.6342/NTU202301637

complete energy transfer in PSII-sc. The resulting distribution of QY values is shown in Figure 4.1, with an average QY of 0.906 and a standard deviation of 0.010. This indicates that the QY only changes slightly regardless of the realization chosen.

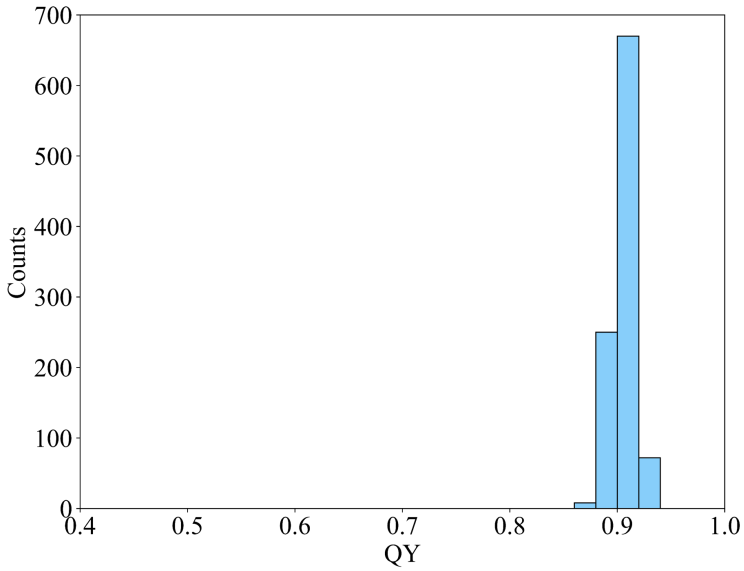

Figure 4.1: The distribution of the QY of 1000 realizations

We also studied the distribution of the delocalization length (L_D) of exciton states in PSII-sc when static disorder is considered. L_D represent the number of pigments where this exciton state delocalized, which are given by Eq.4.1 The average delocalization length of exciton states is depicted in Figure 4.2 a. Our findings indicate that 64% of exciton states have a short delocalization length ($L_D = 1 \sim 2$), indicating that most exciton states are delocalized among 1-2 pigments. Figure 4.2 b shows that the σ of L_D has good linear correlation with averaged L_D, indicating that static disorder has weak effect on the exciton states with low L_D.

$$L_D(\alpha) = \left(\sum_{n=1}^{Nsites} c_n^{\alpha 4} \right)^{-1} \tag{4.1}$$

doi:10.6342/NTU202301637

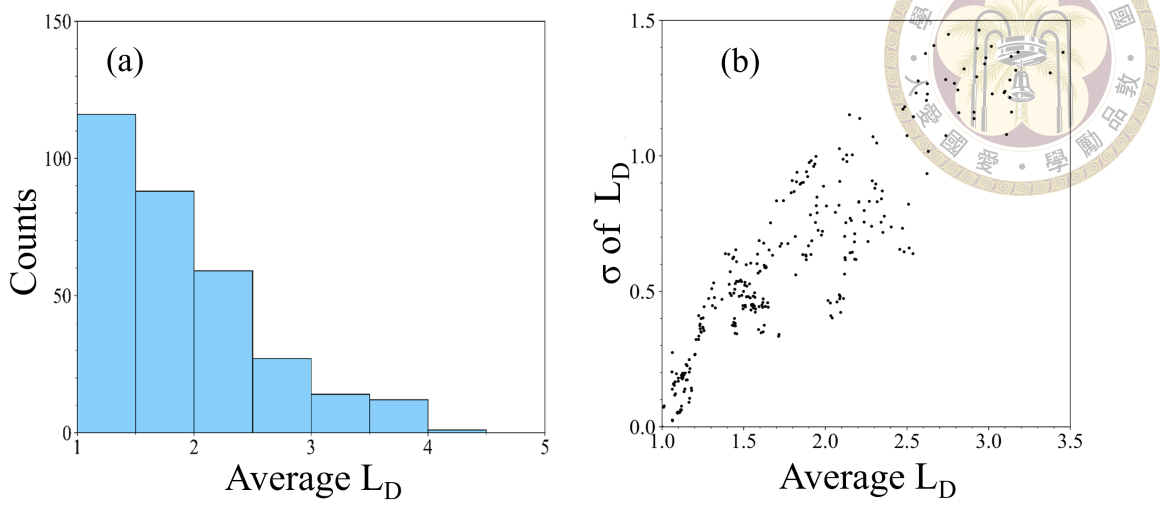

Figure 4.2: (a) Distribution of average L_D of exciton states from 1000 realization (b) Standard deviation of L_D - average L_D

Furthermore, we analyzed the distribution of site energies for 1000 realizations. Since the site energies of pigments change in each realization due to site energy fluctuation from the environment, the rate matrix, eigenvector, and eigenvalue of different realizations are not constants. Figure 4.3 shows the distribution of site energies of pigments for 1000 realizations.

Three types of pigments are in PSII-sc, Chla , Phe, and Chlb, and their distribution of site energies are shown in Figure 4.3. Three groups of site energy distribution are 14600 to 14900 cm^{-1}, 14900 to 15100 cm^{-1}, and 15300 to 15400 cm^{-1}. The Chla mainly contributes to first and second group, the Phe contributes to second group, and Chl b contributes to third group.

doi:10.6342/NTU202301637

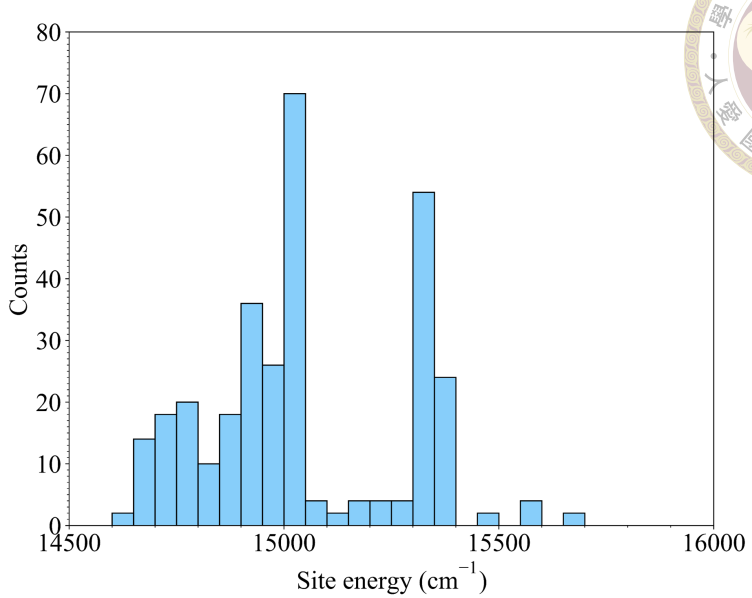

Figure 4.3: The distribution of site energies of pigments of 1000 realizations

In summary, we found that the PSII-sc Hamiltonian in 1000 realizations produces similar QY, and that static disorder has no significant effect on L_D of most exciton states. As a results, we choose a realization with QY of 0.906 for the following investigation.

4.2 Effective internal energy surface of PSII-sc

In order to address the issue of high entropy in the antenna trapping the excitons, which phenomenon has been highlighted by Scholes et al.[23], PSII-sc has to develop a strategy in its energy landscape that enables highly efficient light harvesting. In our investigation, we aim to uncover the specific design employed by PSII-sc to counteract this high entropy.

To achieve this, we construct the effective internal energy surface of PSII-sc. By focusing solely on the effective internal energy component of PSII-sc, we are able to elu-

doi:10.6342/NTU202301637

cidate the design strategies employed to mitigate the impact of high entropy in the antenna. We utilized EET rate matrix to construct the effective internal surface of PSII-sc.

However, there are 318 exciton states in PSII-sc, which makes analyzing this complex energy surface challenging. To simplify this EET rate matrix, my coworker applied the minimum-cut approach to determine the bottlenecks between clusters in the EET rate matrix. As a result, the 318×318 EET rate matrix was reduced to a more manageable 17×17 EET rate matrix. The clustering results are shown in Figure 4.4.

Figure 4.4 a shows the effective rate between clusters, and we found that EET rate matrix network has a circular structure. This circular structure can be depart into upper-circle path and lower-circle path. Upper-circle path is the path along the cluster 1 (RC_1) - 3 - 10 - 13 - 16 - 6 - 2 (RC_2), and lower-circle path is the path along the cluster 2 (RC_2) - 4 - 7 - 11 - 14 - 15 - 5 - 1 (RC_1). Furthermore, Figure 4.4 b shows the location of pigments in each clusters

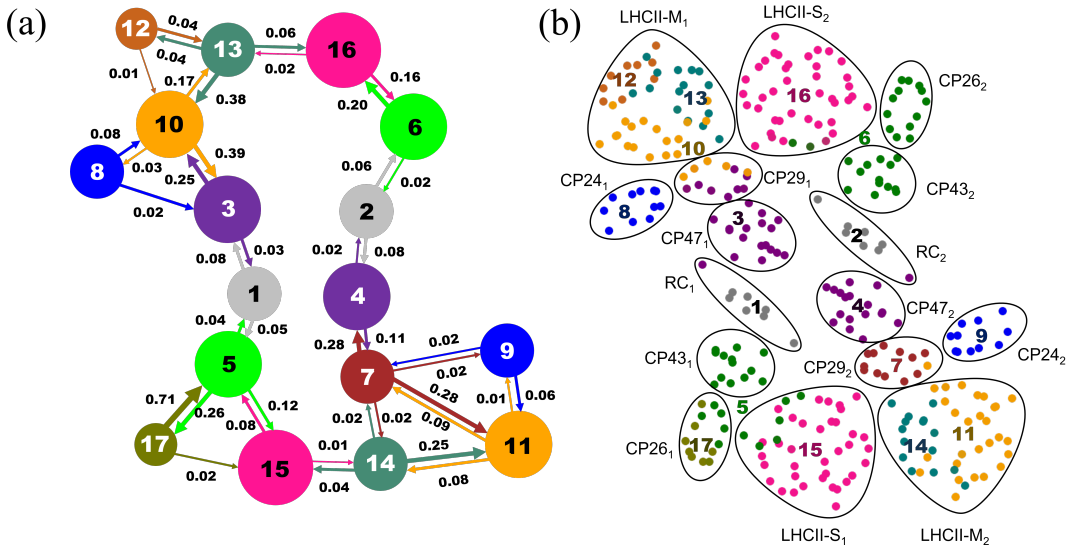

Figure 4.4: (a) The effective rate (in ps^{-1}) between clusters in PSII-sc and (b) the location of pigments in each clusters and in PSII-sc. Note: this picture is done by my coworker, Yun-Chung Yang

doi:10.6342/NTU202301637

4.2.1 Construction of effective internal energy surface

We use this effective rates between clusters to construct the effective internal energy surface of PSII-sc. In this subsection, we define the effective internal energy of clusters in PSII-sc and the activation internal energy from one cluster to another cluster in PSII-sc.

Here, we introduce our method for defining the effective internal energy of cluster A (ΔU_A). Initially, we consider our system is constant number of states and normalized population, so we use canonical ensemble to derive Helmholtz free energy (F), which is given by:

$$F_A = -k_B T ln(Q_A) \tag{4.2}$$

where The partition function Q_A here is equal to the P_A, Temperature (T) is 298 K, P_A is the population in cluster A at thermal equilibrium.

Then, we calculate the effective Helmholtz free energy of cluster A (ΔF_A) by defining a reference point, which is given by:

$$\Delta F_A = -k_B T ln(P_A) - F_{ref} \tag{4.3}$$

where F_{ref} is set to be $-k_B T ln(P_{min})$ so that the maximum of effective Helmholtz free energies of clusters is 0 cm^{-1}.

Then, by removing the entropic term, we can obtain the ΔU_A, which is given by:

$$\Delta U_A = \Delta F_A + T S_A \tag{4.4}$$

where S_A is given by

$$S_A = -k_B ln(N_A) \tag{4.5}$$

doi:10.6342/NTU202301637

where N_A is the number of states in cluster A.

Here, we introduce how we define the activation internal energy from cluster A to cluster B ($\Delta\Delta U^{\ddagger}_{BA}$) in this work. First, we calculate the activation Helmholtz free energy from cluster A to cluster B ($\Delta\Delta F^{\ddagger}_{BA}$) by Arrhenius equation, which is given by:

$$\Delta\Delta F^{\ddagger}_{BA} = -k_B T ln(\frac{R_{BA}}{R_{ref}}) \tag{4.6}$$

where R_{BA} is the effective rate from cluster A to cluster B, and R_{ref} is an arbitrary reference rate. To ensure a reasonable energy landscape where the transition state internal energy between two clusters is larger than the effective internal energy of those clusters, we set R_{ref} as 30 ps^{-1}.

Then, we calculate the effective activation internal energy $\Delta\Delta U^{\ddagger}_{BA}$ by removing the entropic term. The derivative process is following:

$\Delta\Delta F^{\ddagger}_{BA}$ is the energy from ΔF_A to transition state energy between cluster A and cluster B ($\Delta F^{\ddagger}_{BA}$) , which is illustrated in Figure 4.5.

doi:10.6342/NTU202301637

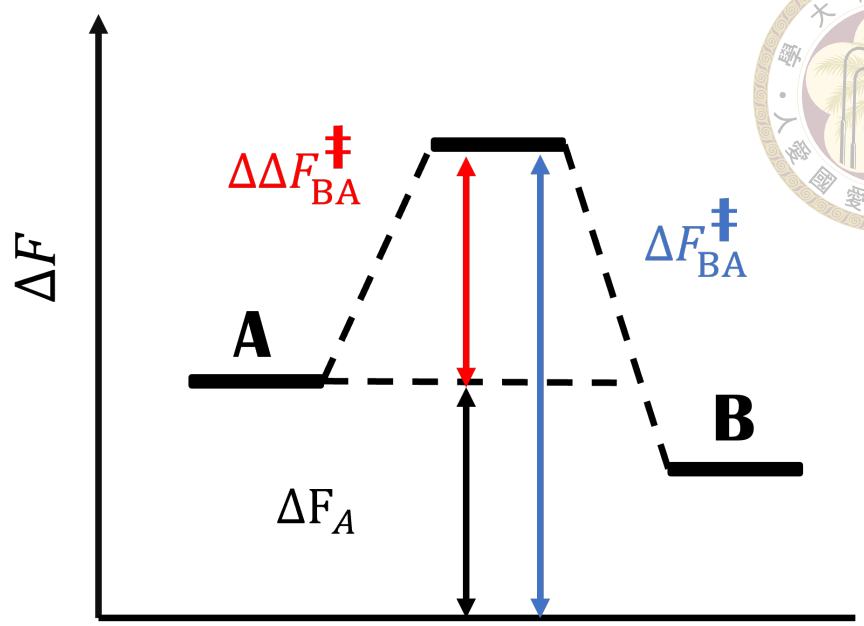

Figure 4.5: Illustration of the relation between $\Delta\Delta F^{\ddagger}_{BA}$ and $\Delta F^{\ddagger}_{BA}$

So, $\Delta\Delta F^{\ddagger}_{BA}$ can be wrote as:

$$\Delta\Delta F^{\ddagger}_{BA} = \Delta F^{\ddagger}_{BA} - \Delta F_A \tag{4.7}$$

We remove the the entropic term in $\Delta F^{\ddagger}_{BA}$ and ΔF_A.

$$\Delta\Delta F^{\ddagger}_{BA} = \Delta U^{\ddagger}_{BA} - (\Delta U_A - TS_A) \tag{4.8}$$

Note that we only consider one the transition state between cluster A and cluster B and we calculate the $\Delta\Delta F^{\ddagger}_{BA}$ by weighted the exciton population at equilibrium. As a result, the entropic term in $\Delta F^{\ddagger}_{BA}$ is 0 and $\Delta F^{\ddagger}_{BA}$ is equal to effective transition internal energy between cluster A and cluster B ($\Delta U^{\ddagger}_{BA}$).

Then, we combine $\Delta U^{\ddagger}_{BA}$ with $-\Delta U_A$, and we get $\Delta\Delta U^{\ddagger}_{BA}$. So, $\Delta\Delta U^{\ddagger}_{BA}$ is given

doi:10.6342/NTU202301637

by:

$$\Delta\Delta U^{\ddagger}_{BA} = \Delta\Delta F^{\ddagger}_{BA} - TS_A \tag{4.9}$$

The relation between $\Delta\Delta U^{\ddagger}_{BA}$ and $\Delta\Delta F^{\ddagger}_{BA}$ is illustrated in Figure 4.6.

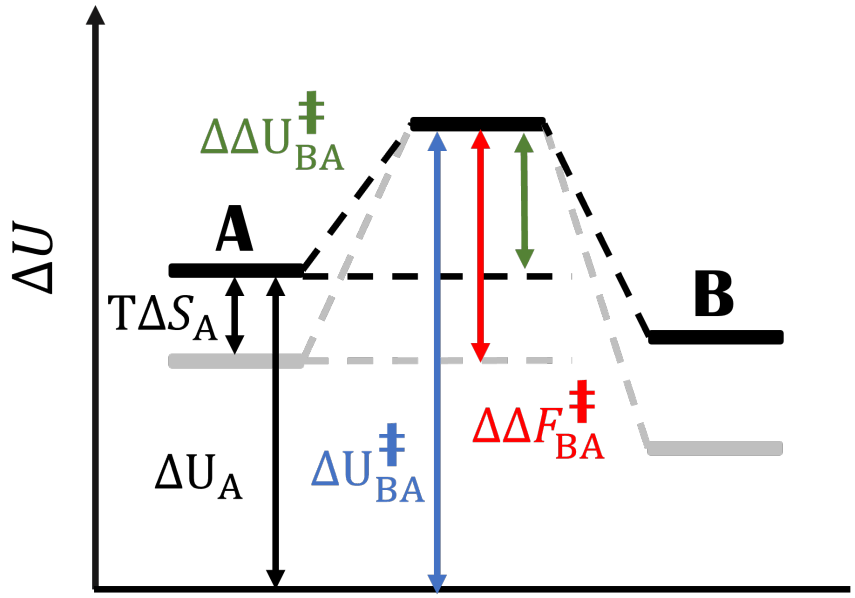

Figure 4.6: Illustration of the relation between $\Delta\Delta U^{\ddagger}_{BA}$ and $\Delta\Delta F^{\ddagger}_{BA}$

Note that the activation energy is a energetic parameter to visualized the EET rate between clusters, the absolute values is meaningless.

Finally, we incorporate the effect of static disorder into the effective internal surface. We sample the PSII-sc Hamiltonian for 1000 realizations and calculate the effective internal surface at each realization. By averaging these individual effective internal surfaces, we obtain the averaged effective internal surface that takes into account the static disorder effect.

doi:10.6342/NTU202301637

4.2.2 High barriers in effective internal energy surface

We construct the effective internal energy surface of the clusters in PSII-sc using the method described in subsection 4.2.1, and we proceed to investigate this effective internal energy surface. By analyzing the characteristics and properties of the effective internal energy surface, we aim to gain insights into the design strategies employed by PSII-sc to mitigate the impact of high entropy in the antenna.

In this effective internal energy surface of the clusters in PSII-sc, which are shown in Figure.4.7, we observe three interesting characteristics. First, the barriers to RC are the bottleneck in EET from antenna to RC. Second, the barriers between the LHCII-M and LHCII-S are as high as the barrier to RC, resulting that the upper-circle path and lower-circle path are divided into 2 paths, respectively. Third, in each path, there is a small energy gradient from outer antenna to RC. Note that because PSII-sc is C_2 symmetry, the effective internal energy surface of the upper-circle path is similar to that of the lower-circle path.

We observe the presence of high barriers in the EET path toward RCs, which is consistent with the literature assignment. On this energies surface, we labeled transition states larger then 1000 cm^{-1} with red. Figure.4.7 a shows the effective internal energy surface along the upper-circle path from RC_1 to RC_2, where cluster 1 is RC_1, and cluster 2 is RC_2. The bottlenecks are located in the EET path from cluster 3 and cluster 6 to RC, which is consistent with previous findings[64]; Figure.4.7 b shows the effective internal energy surface along the lower-circle path from RC_2 to RC_1. Similarly, the bottlenecks are observed in the EET path from cluster 4 and cluster 5 to the RC, mirroring the results obtained from the upper-circle path.

We also observe bottlenecks in the EET path between LHCII-M and LHCII-S, which

doi:10.6342/NTU202301637

divide both the upper-circle path and the lower-circle path into two separate paths. These bottlenecks confine the exciton in the path, effectively reducing the degree of freedom for EET to another path.[67] In Figure.4.7 a, $\Delta U^{\ddagger}_{13-16}$ labeled by red color is a high barrier, so it limits the EET between cluster 13 and cluster 16, and dividing the upper-circle path into path 1 and path 2, as illustrated in Figure.4.7 a. As a result, when an exciton forms in cluster 13, exciton will transfer to RC_1 along the path 1, cluster 13 - 10 - 3 - 1. This bottleneck reduces the degree of freedom for EET to the RC_2; In Figure.4.7 b, $\Delta U^{\ddagger}_{14-15}$ labeled by red color is a high barrier, so it limits the EET between cluster 14 and cluster 15, and dividing the lower-circle path into path 1 and path 2, as illustrated in Figure.4.7 b. Similarly, when an exciton forms in cluster 14, exciton will transfer to RC_2 along the path 1, cluster 14 - 11 - 7 - 4 - 2. This bottleneck reduces the degree of freedom for EET to the RC_1. As a results, these bottlenecks with high effective transition state energies create a timescale separation between path 1 and path 2, confining the exciton within the path, and we verify this timescale separation characteristic in the following section 4.3.

Additionally, we discovered that PSII-sc provides a downhill energy gradient with small energy loss along each path. In Figure 4.7 a, along path 1, we observe the EET from cluster 13 to cluster 1 with a relatively small energy loss of 129 cm^{-1}; In Figure 4.7 b, along path 1, we observe the EET from cluster 17 to cluster 2 with a relatively small energy loss of 147 cm^{-1}. The downhill energy gradient facilitates EET towards the RC, enabling efficient light harvesting in PSII-sc. More analysis of this downhill energy gradient is discussed in the section 6.1.

doi:10.6342/NTU202301637

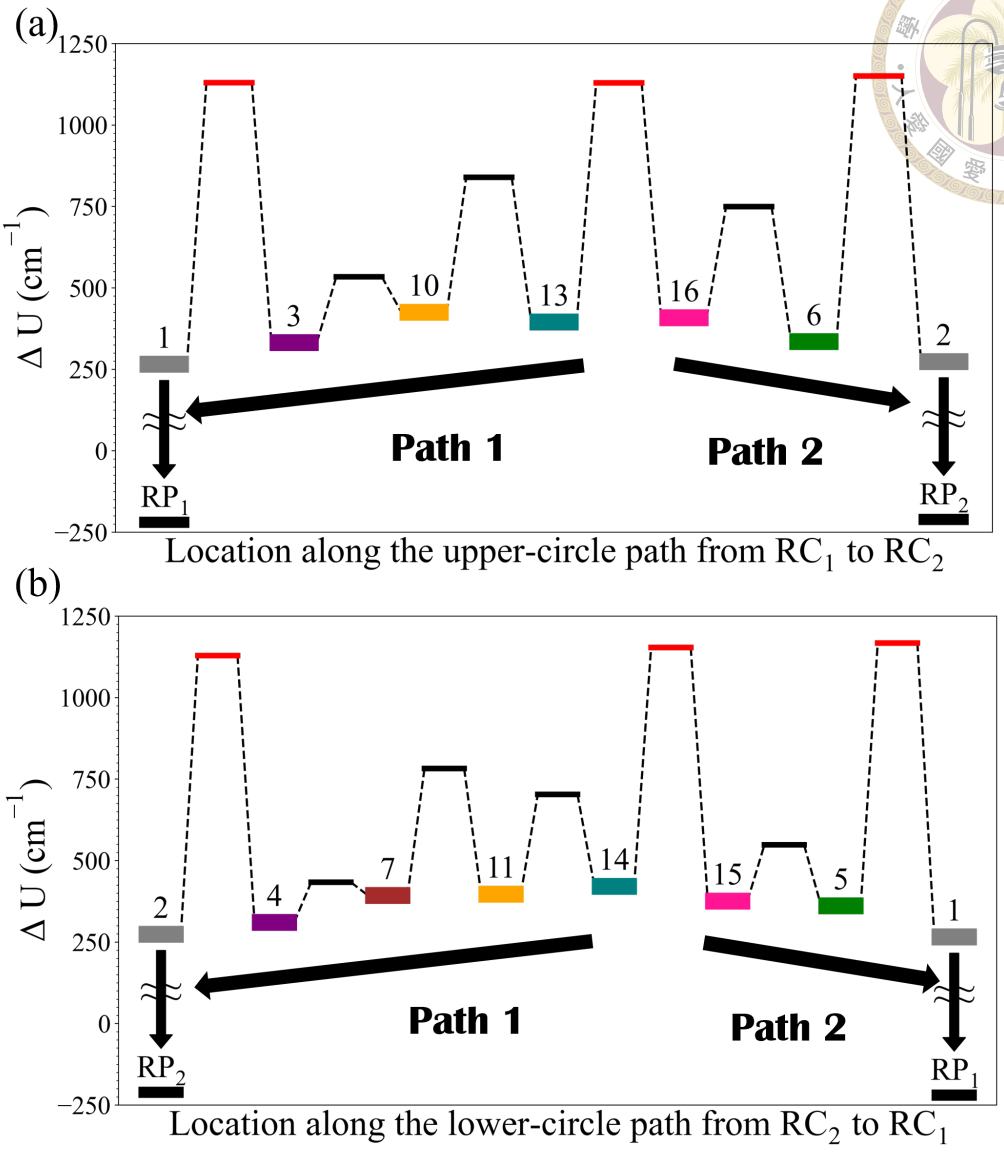

Figure 4.7: Averaged effective internal energy surface of the clusters on the circular network in PSII-sc. (a) effective internal energy surface along the upper-circle path from RC_1 to RC_2 (b) effective internal energy surface along the lower-circle path from RC_2 to RC_1 Note that the cluster 8, 9, 12, and 17 are not in the circular network, so we remove them for clarity (The red states indicate the states with high effective transition state energy)

doi:10.6342/NTU202301637

On the other hand, previous literature [6] suggests that the site 625s in two adjacent CP47s have a relatively strong coupling of 5.14 cm^{-1}, leading to a fast equilibrium of excitons between the two CP47s. In our effective model, we found that the excitonic coupling between the two 625s is 4.22 cm^{-1}, which is consistent with Hsieh's assignment. However, when we extended the PSII-cc system to the larger PSII-sc system ($C_2S_2M_2$), we found another low barrier path for exciton transfer between LHCII-M_1 and LHCII-S_2. The bottleneck for EET in clusters 3, 10, 13, 16, 6, and 2 was found to be the EET from cluster 13 to 16 and from cluster 6 to 2, with effective transition state energies of approximately 1120 cm^{-1}. Moreover, the effective transition state energy between cluster 3 and cluster 4 (EET between CP47s) was found to be as high as 1590 cm^{-1}. Our results suggest that, as we consider more outer antennas connected to the PSII-cc, the EET between LHCII-S and LHCII-M replaces the EET between the 625s, resulting in improved exciton transfer between LHCII-M_1 and LHCII-S_2.

Note that not all clusters are on the circular structure; clusters 8, 9, 12, and 17 connect to the circular structure. The effective transition state energies between these clusters and the circular network are larger than 1000 cm^{-1}, except for cluster 17 which has a comparably low effective transition state energy of 760 cm^{-1} to cluster 5. The effective transition state energies between cluster 8 and 10, cluster 9 and 11, and cluster 12 and 13 are 1174, 1295, and 1293 cm^{-1}, respectively.

4.3 Timescale separation on EET dynamics in PSII-sc

In section 4.2.2, we observed that the bottlenecks between path 1 and path 2 create a timescale separation in PSII-sc. To further investigate the effect of this timescale sepa-

doi:10.6342/NTU202301637

ration on the EET dynamics, we populate the subunits and perform simulations to study the EET dynamics driven by the representative EET rate matrix. In order to visualize the EET dynamics towards the RC, we define an effective center that captures the overall behavior of the EET process. This effective center allows us to analyze the collective behavior of the excitons as they propagate toward the RC, taking into account the influence of timescale separation.

4.3.1 EET dynamics in upper side of PSII-sc

To verify the effect of timescale separation on the EET dynamics in PSII-sc, we populate the subunit in the upper part of PSII-sc and conducted simulations to study the EET dynamics. By populating the subunit and driving the EET dynamics using the representative EET rate matrix, we can observe how the excitons propagate within the PSII-sc system. This approach allows us to investigate the influence of timescale separation on the characteristics of EET dynamics in PSII-sc.

In the upper left side of PSII-sc, populating subunits such as LHCII-M_1-1 or LHCII-M_1-2 leads to the primary transfer of excitons to $CP29_1$, $CP47_1$, and reach RP_1, with a minor population transfer to LHCII-S_2. Similarly, populating LHCII-M_1-3 or $CP24_1$ results in an increased population of $CP29_1$ and $CP47_1$, and most of the population transfers to RP_1. When $CP29_1$ or $CP47_1$ is populated, the majority of the population transfers to RP_1, as mentioned in section 4.2.2. So, as we populate the subunit in the upper left side of PSII-sc, exciton mainly transfers to RP_1 through path 1.

doi:10.6342/NTU202301637

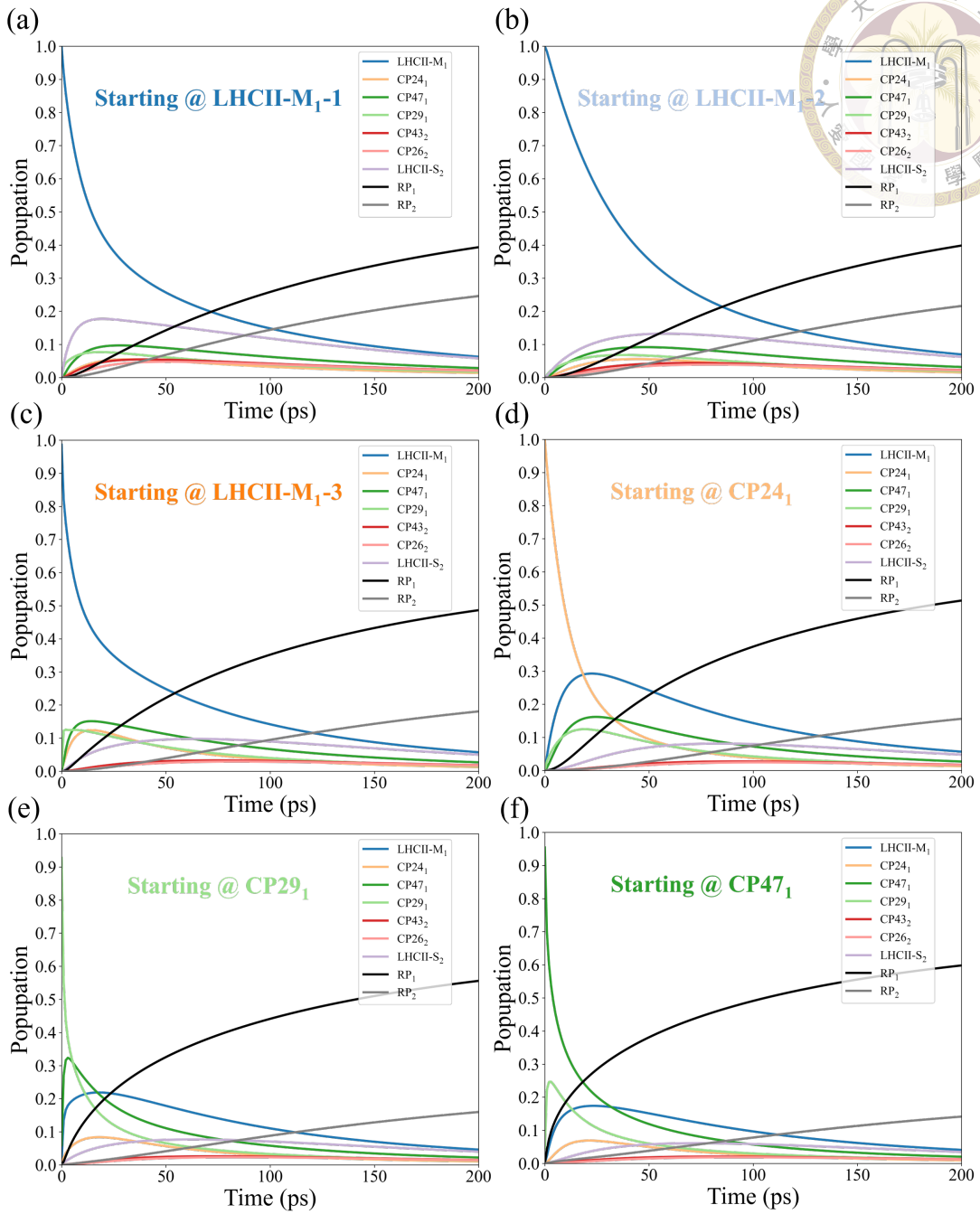

Figure 4.8: The EET dynamics in PSII-sc within 200 ps population time, after we populate the subunit in upper left side of PSII-sc (a) LHCII-M_1-1 (b) LHCII-M_1-2 (c) LHCII-M_1-3 (d) $CP24_1$ (e) $CP29_1$ (f) $CP47_1$ ((Note that the exciton in RC_1 (RC_2) quickly transfer to RP_1 (RP_2), so we remove the EET dynamics of RC_1 and RC_2 for clarity)

In the upper right side of PSII-sc, populating subunits such as LHCII-S_2-1 or LHCII-S_2-2 leads to the primary transfer of excitons to $CP43_2$, $CP26_2$, and reach RP_2, with a minor population transfer to LHCII-M_1. Similarly, populating LHCII-S_2-3 results in an

doi:10.6342/NTU202301637

increased population of $CP26_2$ and $CP43_2$, and most of the population transfers to RP_2. When $CP26_2$ or $CP43_3$ is populated, the majority of the population transfers to RP_2, as mentioned in section 4.2.2. So, as we populate the subunit in the upper right side of PSII-sc, exciton mainly transfers to RP_2 through path 2.

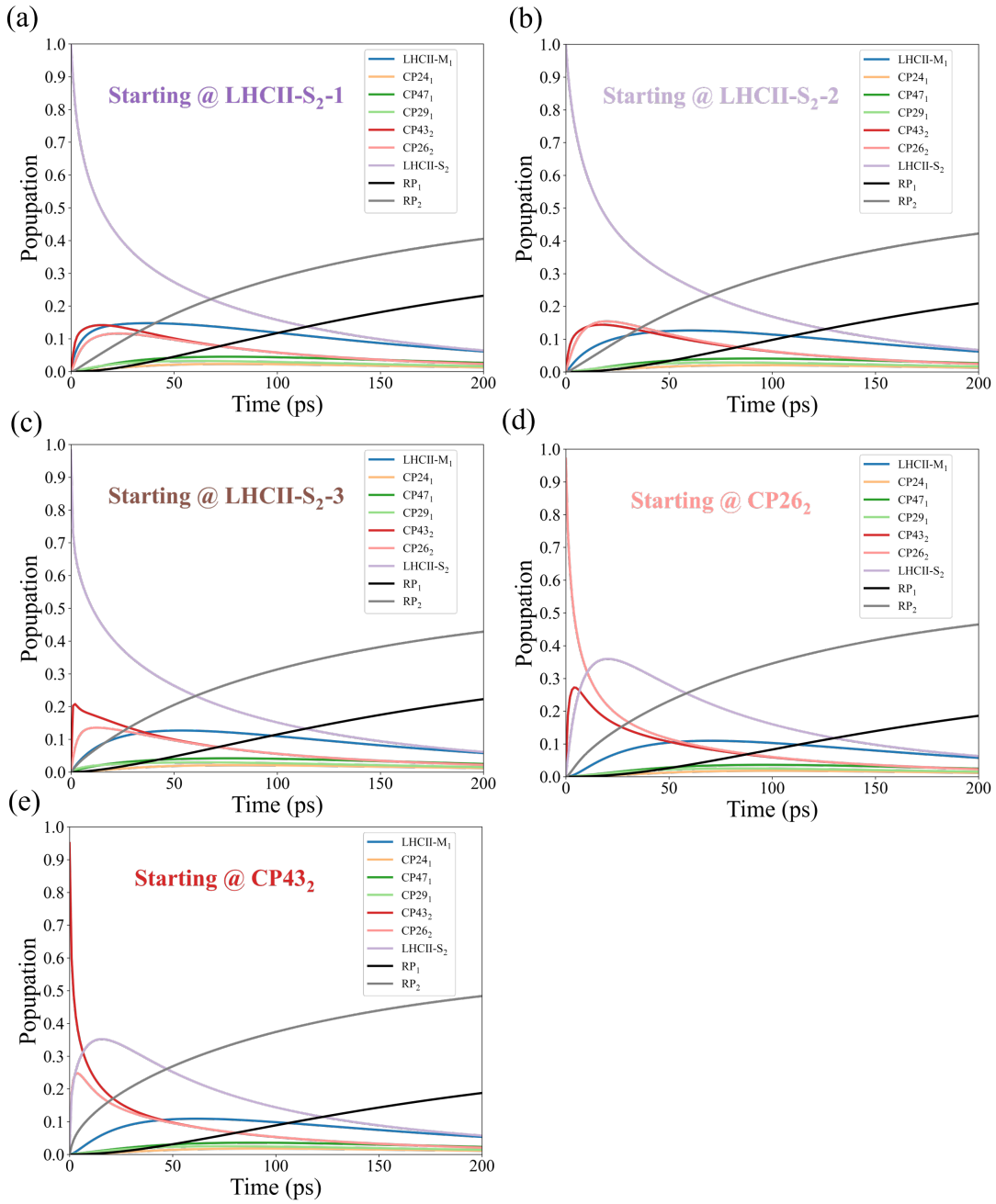

Figure 4.9: The EET dynamics in PSII-sc within 200 ps population time, after we populate the subunit in upper right side of PSII-sc (a) LHCII-S_2-1 (b) LHCII-S_2-2 (c) LHCII-S_2-3 (d) $CP26_2$ (e) $CP43_2$ (Note that the exciton in RC_1 (RC_2) quickly transfer to RP_1 (RP_2), so we remove the EET dynamics of RC_1 and RC_2 for clarity)

doi:10.6342/NTU202301637

4.3.2 Energy transfer trajectories to RC

In section 4.3.1, we investigated the EET dynamics of each subunit in PSII-sc to verify the timescale separation effect in EET dynamics. However, visualizing the precise pathways and dynamics of exciton transfer within the complex PSII-sc system can be challenging based solely on population dynamics. To overcome this limitation, we introduce the concept of effective centers. These effective centers allow us to track the movement of excitons from the antenna to RC_1 or RC_2. By defining two types of effective centers that represent the overall location of excitons in PSII-sc, we repeat the EET dynamics in section 4.3.1 and obtain a more comprehensive understanding of the timescale separation effect in EET dynamics.

To visualize to EET from antenna to RC_1, we define the effective center to RC_1 ($\boldsymbol{r_{RC_1}}$) by Eq. 4.10. As we populate a subunit in upper side of PSII-sc, the kinetic trace of this RC_1 give us an idea how exciton transfer from the subunit to RC_1. Similarity, to visualize to EET from subunit to RC_2, we define the effective center to RC_2 ($\boldsymbol{r_{RC_2}}$) by Eq. 4.11.

$$\boldsymbol{r_{RC_1}} = \sum_{n \in RC_1, uA} P_n \boldsymbol{r_n} \tag{4.10}$$

$$\boldsymbol{r_{RC_2}} = \sum_{n \in RC_2, uA} P_n \boldsymbol{r_n} \tag{4.11}$$

Here, uA is the antenna in uppper side of PSII-sc, which are LHCII-M_1, $CP24_1$, $CP29_1$, $CP47_1$, LHCII-S_2, $CP26_2$, and $CP43_2$. P_n is the population of exciton at pigment n, and $\boldsymbol{r_n}$ is the position of pigment n.

doi:10.6342/NTU202301637

We repeated the EET dynamics described in section 4.3.1 and calculated the kinetic traces of r_{RC_1} and r_{RC_2} as a function of time for each dynamics. These kinetic traces are plotted in Figure 4.10 to verify the effect of timescale separation on EET dynamics. For this analysis, we only populated the complex in the upside PSII-sc, as the results from the downside PSII-sc were similar to those obtained from the upside PSII-sc.

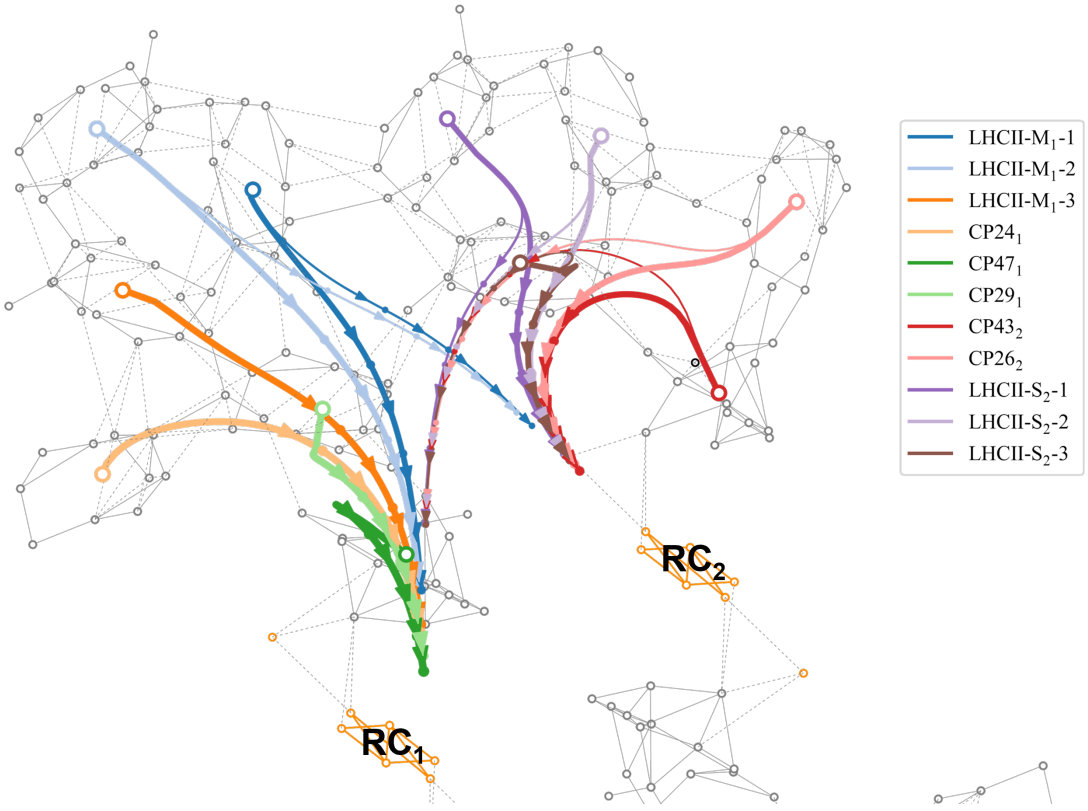

Figure 4.10: Energy transfer trajectories of the effective center of population from 0 ps to 200 ps (The times of circle labels in path are 0, 50, 100, 200 ps) (Both RC_2 and RC_1 contribute to the QYs. However, to ensure clarity in the visualization, if the ratio of high QY and low QY is larger than 2, we ignore the minor path.)

In Figure 4.10, we observe that when we populate the subunit in the upper left side of PSII-sc, the majority of excitons transfer to RC_1. Only LHCII-M_1-1 and LHCII-M_2-2 show a minor kinetic trace to RC_2. Conversely, when we populate the subunit in the upper right side of PSII-sc, the excitons predominantly transfer to RC_2, with a minor kinetic trace to RC_1. This EET dynamics demonstrates the timescale separation between LHCII-

doi:10.6342/NTU202301637

M_1 and LHCII-M_2, which is consistent with the observation in section 4.2.2.

Additionally, due to the presence of bottlenecks in the EET to RC and between M_1 and M_2, the population of excitons quickly diffuses along their respective paths. When we populate $CP47_1$, its kinetic trace initially goes up and then goes down to RC_1. Similarly, when we populate $CP43_2$, its kinetic trace initially goes up and then goes down to RC_2 These observations indicate that excitons rapidly diffuse within their respective pathways.

To further confirm the timescale effect on EET dynamics in PSII-sc, we calculate the QY of RC_1 and RC_2 for each subunit. We ran the dynamics simulation until 10000ps and calculated the QY in RC_1 and RC_2 as shown in Table 4.1. Interestingly, we observed that when we initially populated the subunit in the up-left side of PSII, RC_1 contributions were approximately 0.3 larger than RC_2 contributions. Conversely, when we initially populated the subunit in the up-right side of PSII, RC_2 contributions were about 0.2 larger than RC_1 contributions. This observation can be attributed to the bottlenecks that confine the excitons in their path, resulting in the RC in their path having a higher contribution than the other RC. Therefore, this result provides evidence for the existence of timescale separation of bottlenecks.

Subunit	LHCII-M_1-1	LHCII-M_1-2	LHCII-M_1-3	$CP24_1$	$CP47_1$	$CP29_1$
RC_1	0.54	0.56	0.63	0.65	0.71	0.67
RC_2	0.36	0.34	0.29	0.26	0.22	0.25
Subunit	$CP43_2$	$CP26_2$	LHCII-S_2-1	LHCII-S_2-2	LHCII-S_2-3	
RC_1	0.32	0.33	0.38	0.36	0.36	
RC_2	0.59	0.58	0.53	0.55	0.55	

Table 4.1: The QYs of RC_1 and RC_2 as each subunit in the upside side of PSII are excited

Figure 4.7 and the kinetic traces on Figure 4.10 demonstrate that the bottlenecks

doi:10.6342/NTU202301637

with high effective transition state energies play an essential role in the EET dynamics of PSII. This study provides new insights into the EET process in PSII and highlights the importance of considering the effective transition state energy when designing large light harvesting system.

4.4 Summary

In this section, we investigated the impact of static disorder on the QY of light harvesting in PSII-sc. Remarkably, we found that despite different realizations of the Hamiltonian, the QY consistently remained high at 0.9. This suggests that static disorder has minor effect on the overall efficiency of energy transfer within the system. Furthermore, we observed that the static disorder had only a minor influence on the localization of exciton states (L_D). These findings indicate the robustness of PSII-sc against variations in the Hamiltonian, indicating that the energy transfer dynamics are relatively unaffected by present static disorder.

To uncover how PSII-sc mitigates the impact of entropy, we constructed the effective internal energy surface of PSII-sc, as described in section 4.2.1. This energy surface revealed three intriguing characteristics. Firstly, we observed that the EET path to the RC acts as a rate-determining step in light harvesting, underscoring its crucial role in energy transfer efficiency. Secondly, the presence of a high energy barrier between the LHCII-M_1 and LHCII-S_2 (the LHCII-M_2 and LHCII-S_1) creates timescale separation, effectively confining excitons within their respective pathways. This timescale separation ensures efficient and directional energy transfer within PSII-sc. Lastly, we noted that along each pathway, there is a gradual decrease in energy towards the RC. This energy gradient fa-

doi:10.6342/NTU202301637

cilitates smooth and efficient exciton transfer, minimizing energy losses throughout the process.

Furthermore, to verify the timescale separation effect on EET dynamics within PSII-sc in our investigation, we utilized effective centers to track the kinetic movement of excitons towards RC_1 and RC_2. Upon populating the subunit in the upper left side of PSII-sc, we observed a significant transfer of excitons to RC_1, while only a minor fraction was observed to transfer to RC_2. This evidence strongly demonstrates the presence of timescale separation in the EET process within PSII-sc.

doi:10.6342/NTU202301637

Chapter 5

Inter PSII-sc EET on the thylakoid membrane

5.1 The crystal parameters of PSII-scs on the thylakoid membrane

Investigating how PSII-sc transfers excitons to RC is crucial for understanding the process of light harvesting in photosynthesis. Within the thylakoid membrane, PSII-sc units aggregate and efficiently absorb sunlight and transfer to RC. This aggregation phenomenon enhances the coupling between PSII-sc units and facilitates the transfer of exciton energy between them. To gain insights into this EET process among PSII-sc units, it is essential to determine the crystal parameters of PSII-sc aggregating in the thylakoid membrane, first.

To determine the crystal parameters for PSII-sc aggregation, however, our PSII-sc structure, obtained through Cryo-EM, represents only a single PSII-sc unit and lacks information on how PSII-sc aggregates. To overcome this limitation, we turned to crystal parameters derived from electron micrographs[68]. But, we encountered a discrepancy

doi:10.6342/NTU202301637

when directly applying these parameters to the experimental electron micrographs, potentially attributed to the fact that the images were obtained from *Arabidopsis thaliana* instead of *Pisum sativum*. To address this issue, we made slight adjustments to the parameters to better align them with the observed image.

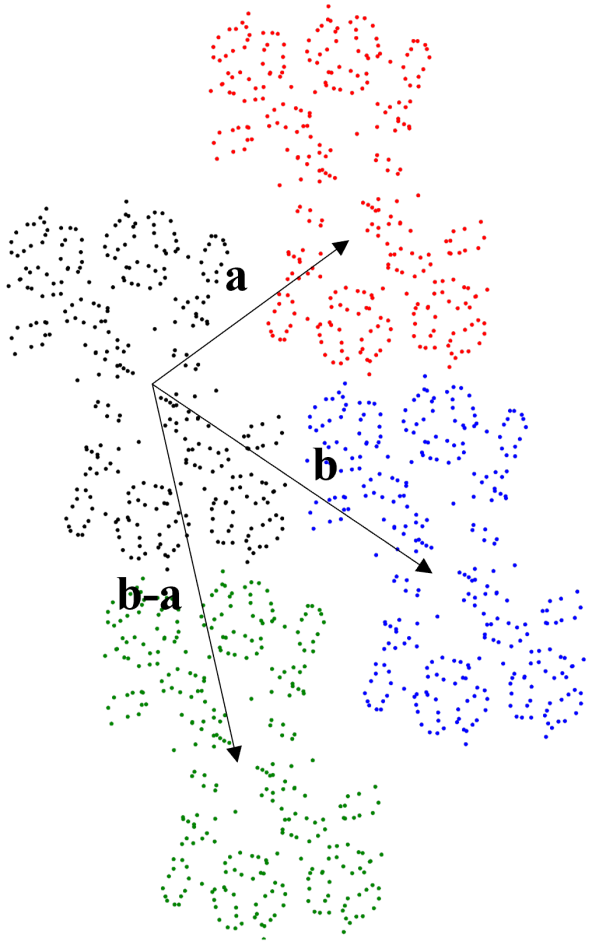

Figure 5.1: The arrangement of PSII-scs

We determined two sets of crystal parameters for PSII-sc: one obtained under low light adaptive conditions and the other under high light adaptive conditions. The arrangement of PSII-sc units in the thylakoid membranes undergoes changes in response to varying sunlight intensities, allowing them to adapt to different environmental conditions. These two sets of parameters may yield different results, revealing how the arrangement of PSII-scs influences the EET between them. The arrangement of PSII-scs is shown in

doi:10.6342/NTU202301637

Figure 5.1. For each light condition, the 2D crystal parameters of PSII-sc include vectors $\boldsymbol{a}$ and $\boldsymbol{b}$, which are detailed in Table 5.1. The comparison results of experimental alignment of PSII-scs and our model are showed in Figure 5.2.

Condition	$\boldsymbol{a}$	$\boldsymbol{b}$
LL	(162.1, 110.8)	(238.4, -152.5)
HL	(158.2, 140.9)	(233.7, -126.1)

Table 5.1: The fitted crystal parameter (Å)

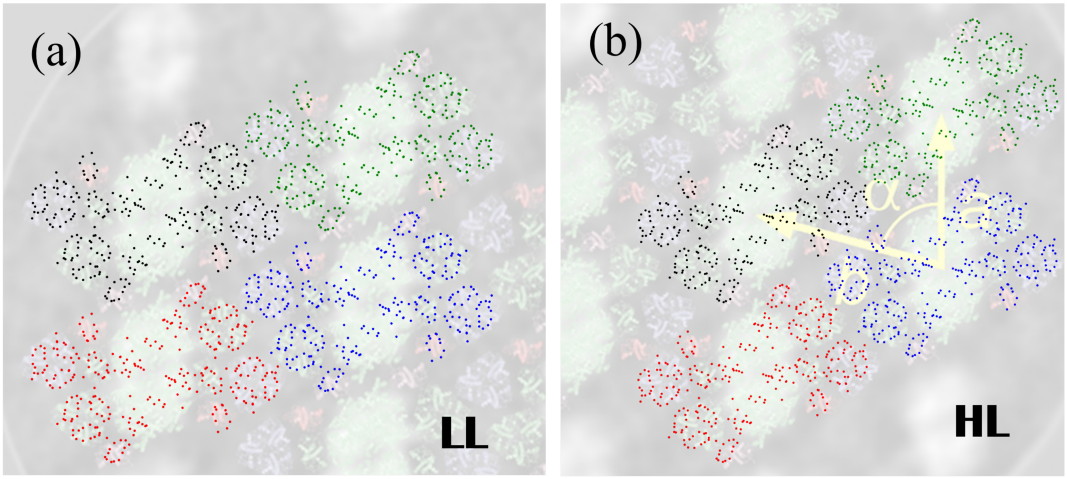

Figure 5.2: The comparison of alignment of PSII-scs in experimental results and in our model (a) at low light adaptive (b) at high light adaptive

5.2 Migration time between two adjacent PSII-scs

With the obtained crystal parameters, we are able to calculate the couplings between PSII-scs, simulate the EET between two PSII-sc units, and define the migration time between them to quantify the EET rate between two PSII-scs. In Figure 5.3 (a), two PSII-sc units are aligned along the $\boldsymbol{b} - \boldsymbol{a}$ direction. The two RCs in the upper PSII-sc unit are denoted as RC_A, while the two RCs in the lower PSII-sc unit are denoted as RC_B. By

doi:10.6342/NTU202301637

populating the antenna in the blue region, the exciton can either transfer to RC_A with a timescale of τ_{migA} or transfer to the antenna in the green region and reach RC_B with a timescale of τ_{migB}, as illustrated in Figure 5.3 (b). As a results, we consider a kinetics model as depicted in Figure 5.3 (c), where the plausible paths for the exciton are transferring to RC_A, RC_B, or undergo stimulated emission. We can evaluate RC_A and RC_B with Eq 5.1.

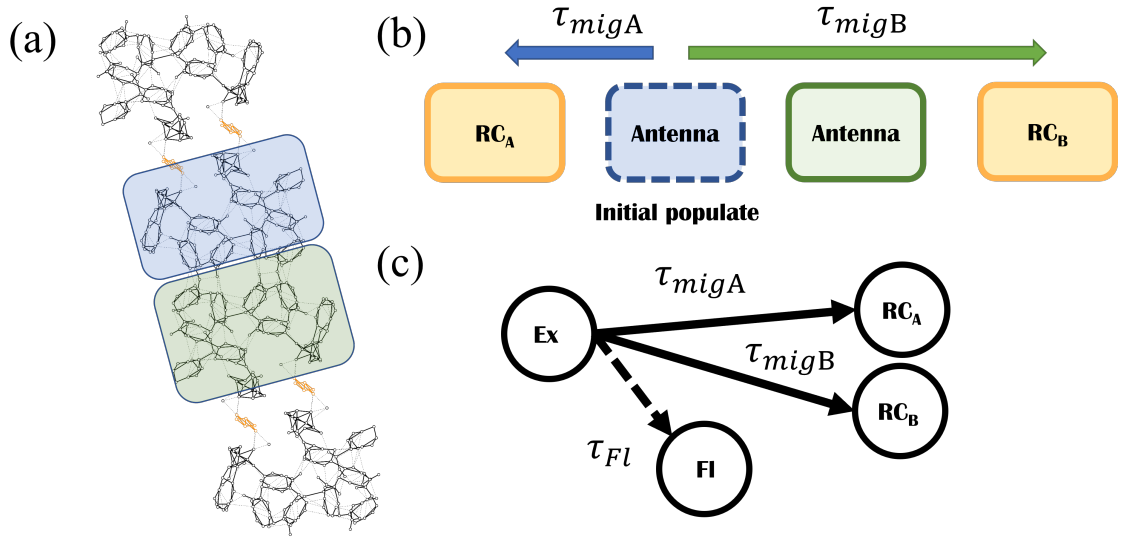

Figure 5.3: (a) the structure of two connecting PSII-sc along the $\boldsymbol{b} - \boldsymbol{a}$ direction (b) as the exciton forms, it transfers to RC_A and to RC_B (c) the plausible paths for exciton are transferring to RC_A, RC_B, and stimulated emission of exciton

$$\frac{QY_A}{k_{migA}} = \frac{QY_B}{k_{migB}} = \frac{1 - QY_A - QY_B}{k_{decay}} \tag{5.1}$$

where QY_A represents the population in RC_A.

We then proceed to calculate the migration time between the antenna in the blue region and the antenna in the green region, which allows us to estimate the EET rate between the two PSII-sc units. In Figure 5.4 (a), we begin by populating the antenna in the blue region and calculate the quantum yields QY_A and QY_B to evaluate τ_{migA}^{inA} and τ_{migB}^{inA},

doi:10.6342/NTU202301637

respectively. Here, $\tau_{\text{migA}}^{\text{inA}}$ represents the migration time from the antenna in the blue region to RC_A. Similarly, in Figure 5.4 (b), we populate the antenna in the green region and calculate QY_A and QY_B to evaluate $\tau_{\text{migA}}^{\text{inB}}$ and $\tau_{\text{migB}}^{\text{inB}}$, respectively.

Next, we estimate the migration time from the antenna in the blue region to the antenna in the green region by calculating $\tau_{\text{migB}}^{\text{inA}} - \tau_{\text{migB}}^{\text{inB}}$, as illustrated in Figure 5.4 (c). Additionally, we estimate the migration time from the antenna in the green region to the antenna in the blue region by calculating $\tau_{\text{migA}}^{\text{inB}} - \tau_{\text{migA}}^{\text{inA}}$.

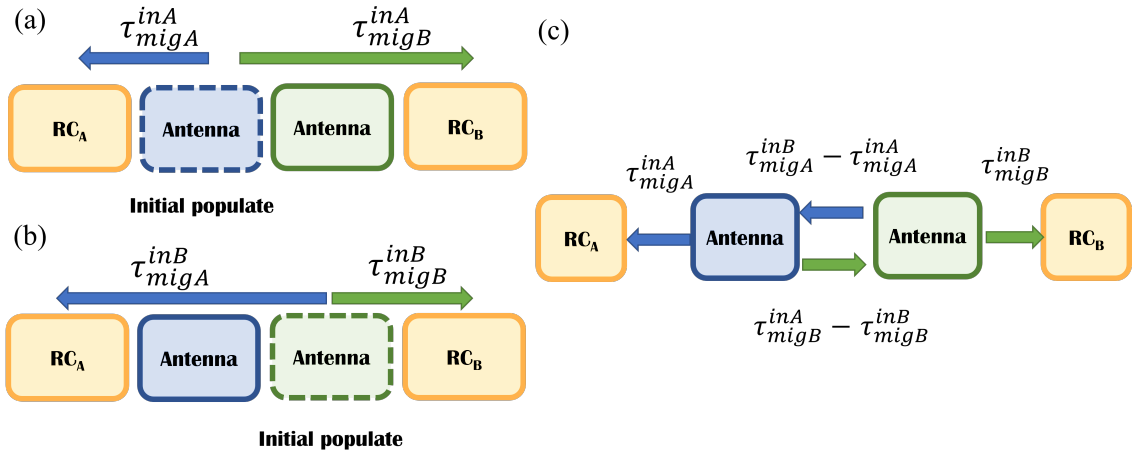

Figure 5.4: Illustration of exciton migration to RC_A and RC_B (a) the antenna in the blue region is populated (b) the antenna in the green region is populated (c) the migration time between the antenna in the blue region and that in the green region

5.2.1 Low light adaptive condition

At the low light adaptive condition, we employ the crystal parameters listed in Table 5.1 to construct the effective Hamiltonian for two PSII-sc units aligned in three directions. As the PSII-sc units aggregate on the membrane, we observe three plausible arrangements for the two PSII-sc units, as depicted in Figure 5.5. In this context, we define the antenna located in the blue region and the antenna located in the green region, as illustrated in the figure.

doi:10.6342/NTU202301637

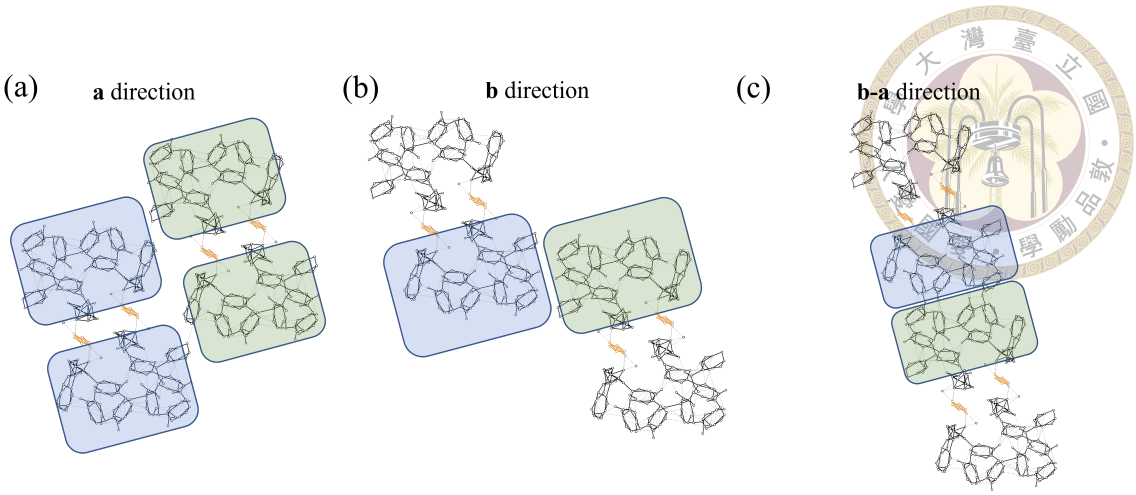

Figure 5.5: The two PSII-sc units at low light adaptive condition aligned along (a) $\boldsymbol{a}$ direction (b) $\boldsymbol{b}$ direction (c) $\boldsymbol{b}-\boldsymbol{a}$ direction

Then, we utilize these model estimate the migration times for the three directions. For $\boldsymbol{a}$ direction, we sample 1000 realization and calculate the migration times ($\tau^{\text{inA}}_{\text{migA}}$, $\tau^{\text{inA}}_{\text{migB}} - \tau^{\text{inB}}_{\text{migB}}$, $\tau^{\text{inB}}_{\text{migA}} - \tau^{\text{inA}}_{\text{migA}}$, $\tau^{\text{inB}}_{\text{migB}}$). We then average these migration times. Similarly, we repeat this process for the $\boldsymbol{b}$ direction and the $\boldsymbol{b}-\boldsymbol{a}$ direction. The resulting migration times are listed in Table 5.2.

In Table 5.2, $\tau^{\text{inA}}_{\text{migA}}$ and $\tau^{\text{inB}}_{\text{migB}}$ represent the migration times to the nearest RC within each PSII-sc unit, while $\tau^{\text{inA}}_{\text{migB}} - \tau^{\text{inB}}_{\text{migB}}$ and $\tau^{\text{inB}}_{\text{migA}} - \tau^{\text{inA}}_{\text{migA}}$ represent the migration times between PSII-sc units.

direction	$\tau^{\text{inA}}_{\text{migA}}$	$\tau^{\text{inA}}_{\text{migB}} - \tau^{\text{inB}}_{\text{migB}}$	$\tau^{\text{inB}}_{\text{migA}} - \tau^{\text{inA}}_{\text{migA}}$	$\tau^{\text{inB}}_{\text{migB}}$
$\boldsymbol{a}$	232 ± 29	2582 ± 273	2648 ± 330	229 ± 32
$\boldsymbol{b}$	241 ± 41	1698 ± 213	1721 ± 209	238 ± 41
$\boldsymbol{b}-\boldsymbol{a}$	301 ± 49	**450±66**	**430±66**	297 ± 49

Table 5.2: The migration times at low light adaptive condition (ps) (the first value in table represent the average value, and the second value represent the σ value)

The analysis of migration times for the three directions reveals interesting insights. In the $\boldsymbol{a}$ and $\boldsymbol{b}$ directions, the migration times to the nearest RC are approximately 230 ps,

doi:10.6342/NTU202301637

while the migration times between PSII-sc units are an order of magnitude larger. This suggests that the excitons primarily undergo efficient energy transfer to the nearest RC within each PSII-sc unit.

On the other hand, in the $\boldsymbol{b} - \boldsymbol{a}$ direction, the migration times to the nearest RC are around 300 ps, which are relatively longer compared to the $\boldsymbol{a}$ and $\boldsymbol{b}$ directions. This could be attributed to the fast EET between PSII-sc units, where the exciton has a higher probability of transferring to another PSII-sc unit before reaching the RC, thereby increasing the migration times. Notably, the migration time between PSII-sc units (highlighted in bold text) is similar to the migration times to the nearest RC. This observation suggests that in the $\boldsymbol{b} - \boldsymbol{a}$ direction, the excitons are allowed to transfer to another PSII-sc unit before reaching the RC.

To further strengthen the reliability of our results based on the crystal parameters, we conducted additional calculations by decreasing the $\boldsymbol{a}$ and $\boldsymbol{b}$ values by 3 Å, and reevaluated the migration times. The updated migration times are presented in Table 5.3.

direction	$\tau_{\text{migA}}^{\text{inA}}$	$\tau_{\text{migB}}^{\text{inA}} - \tau_{\text{migB}}^{\text{inB}}$	$\tau_{\text{migA}}^{\text{inB}} - \tau_{\text{migA}}^{\text{inA}}$	$\tau_{\text{migB}}^{\text{inB}}$
$\boldsymbol{a}$	236 ± 30	2145 ± 221	2201 ± 268	233 ± 32
$\boldsymbol{b}$	248 ± 42	1356 ± 170	1338 ± 175	244 ± 42
$\boldsymbol{b} - \boldsymbol{a}$	313 ± 52	**376±73**	**356±69**	308 ± 53

Table 5.3: The migration times at low light adaptive condition (ps) where decreasing the $\boldsymbol{a}$ and $\boldsymbol{b}$ by 3 Å (the first value in table represent the average value, and the second value represent the σ value)

In the $\boldsymbol{a}$ and $\boldsymbol{b}$ directions, we observe that the migration times between PSII-sc units are relatively larger compared to the migration times to the nearest RC. This finding aligns with our initial model, indicating that the EET between PSII-sc units is less efficient than the transfer to the nearest RC within each PSII-sc unit.

doi:10.6342/NTU202301637

In the $\boldsymbol{b} - \boldsymbol{a}$ direction, the migration times to the nearest RC remain similar to the previous model. This suggests that the changes in the crystal parameters did not significantly impact the migration times in this direction. Therefore, the consistency between the migration times to the nearest RC and those between PSII-sc units reinforces the robustness of our results.

To sum up, at low light adaptive conditions, when excitons are formed in the PSII-sc membrane, they have two possible paths for transfer, as illustrated in Figure 5.6. The first path is the transfer to the nearest RCs within the same PSII-sc unit. The second path is the transfer to another PSII-sc unit along the $\boldsymbol{b} - \boldsymbol{a}$ direction and transfer to another RCs.

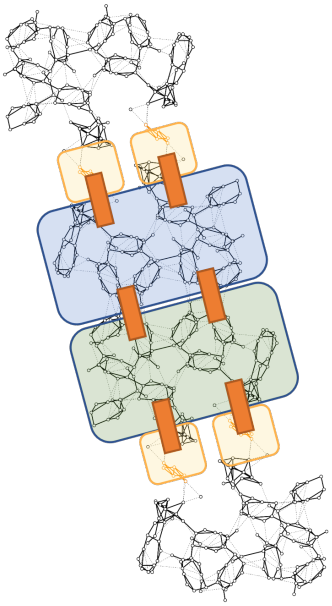

Figure 5.6: Illustration of plausible path for EET at low light adaptive

5.2.2 High light adaptive condition

At the high light adaptive condition, we utilize the crystal parameters listed in Table 5.1 to construct the effective Hamiltonian for two PSII-sc units aligned in three directions.

doi:10.6342/NTU202301637

However, it should be noted that for the $\boldsymbol{a}$ direction, the couplings between the two PSII-sc units are close to zero. Therefore, we will exclude the $\boldsymbol{a}$ direction in this discussion. As the PSII-sc units aggregate on the membrane, we observe two plausible arrangements for the two PSII-sc units, as depicted in Figure 5.7. In this context, we select the antenna located in the blue region and the antenna located in the green region to populate, as illustrated in the figure.

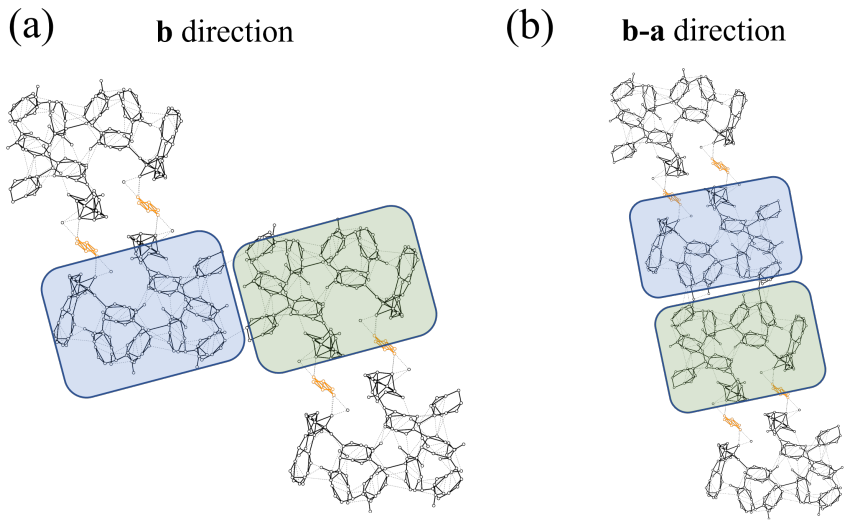

Figure 5.7: The two PSII-sc units at hight light adaptive condition aligned along (a) $\boldsymbol{b}$ direction (b) $\boldsymbol{b}-\boldsymbol{a}$ direction

Then, we utilize these model estimate the migration times for the two directions. For $\boldsymbol{b}$ direction, we sample 1000 realization and calculate the migration times ($\tau^{\text{inA}}_{\text{migA}}$, $\tau^{\text{inA}}_{\text{migB}} - \tau^{\text{inB}}_{\text{migB}}$, $\tau^{\text{inB}}_{\text{migA}} - \tau^{\text{inA}}_{\text{migA}}$, $\tau^{\text{inB}}_{\text{migB}}$). We then average these migration times. Similarly, we repeat this process for the $\boldsymbol{b}-\boldsymbol{a}$ direction. The resulting migration times are listed in Table 5.4.

direction	$\tau^{\text{inA}}_{\text{migA}}$	$\tau^{\text{inA}}_{\text{migB}} - \tau^{\text{inB}}_{\text{migB}}$	$\tau^{\text{inB}}_{\text{migA}} - \tau^{\text{inA}}_{\text{migA}}$	$\tau^{\text{inB}}_{\text{migB}}$
$\boldsymbol{b}$	265 ± 45	**846±109**	**839±124**	261 ± 45
$\boldsymbol{b}-\boldsymbol{a}$	289 ± 48	**554±75**	**531±77**	285 ± 47

Table 5.4: The migration times at high light adaptive condition (ps) (the first value in table represent the average value, and the second value represent the σ value)

doi:10.6342/NTU202301637

In the $\boldsymbol{b}$ and $\boldsymbol{b}-\boldsymbol{a}$ directions under high light adaptive conditions, the migration times to the nearest RC are approximately 270 ps. Interestingly, the migration times between PSII-sc units (highlighted in bold text) are the same order to the migration times to the nearest RC. This indicates that there is a possibility of exciton energy hopping between closely aligned PSII-sc units before it ultimately reaches the RC.

Again, to further strengthen the reliability of our results based on the crystal parameters, we conducted additional calculations by decreasing the $\boldsymbol{a}$ and $\boldsymbol{b}$ values by 3 Å, and reevaluated the migration times. The updated migration times are presented in Table 5.5.

direction	$\tau_{\text{migA}}^{\text{inA}}$	$\tau_{\text{migB}}^{\text{inA}}-\tau_{\text{migB}}^{\text{inB}}$	$\tau_{\text{migA}}^{\text{inB}}-\tau_{\text{migA}}^{\text{inA}}$	$\tau_{\text{migB}}^{\text{inB}}$
$\boldsymbol{b}$	270 ± 45	**761±98**	**756±112**	266 ± 45
$\boldsymbol{b}-\boldsymbol{a}$	301 ± 49	**450±66**	**430±66**	297 ± 49

Table 5.5: The migration times at high light adaptive condition (ps) where decreasing the $\boldsymbol{a}$ and $\boldsymbol{b}$ by 3 Å (the first value in table represent the average value, and the second value represent the σ value)

In the $\boldsymbol{b}$ and $\boldsymbol{b}-\boldsymbol{a}$ directions, the migration times to the nearest RC and the migration time between PSII-sc units remain similar to the previous model, even with the adjusted crystal parameters. This suggests that the changes made to the crystal parameters did not have a significant impact on the migration times in these directions. The consistency in the results further strengthens the confidence in the estimated migration times and the overall model.

At higt light adaptive conditions, when excitons are formed in the PSII-sc membrane, they have three possible paths for transfer, as illustrated in Figure 5.8. The first path is the transfer to the nearest RCs within the same PSII-sc unit. The second path is the transfer to another PSII-sc unit along the $\boldsymbol{b}-\boldsymbol{a}$ direction and transfer to another RCs. The third path

doi:10.6342/NTU202301637

is the transfer to another PSII-sc unit along the ***b*** direction and transfer to another RCs.

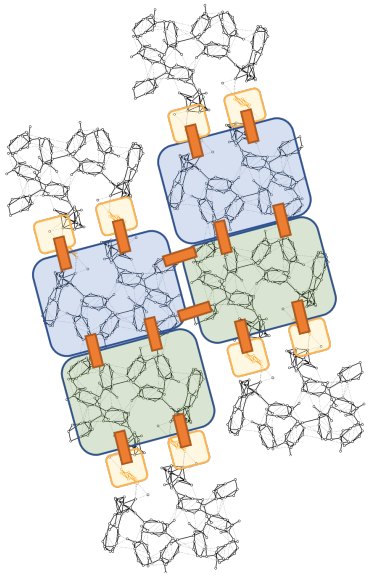

Figure 5.8: Illustration of plausible path for EET at high light adaptive

In the case of exciton energy transfer (EET) along the ***b*** direction, the exciton has the probability to migrate across multiple PSII-sc units. To investigate this phenomenon in the context of high light adaptation, we constructed a larger model of PSII-sc units to study EET on the thylakoid membrane. For convenience, we redefine a PSII-sc unit as the antenna enclosed within a black square.

Figure 5.9 illustrates the construction of our system, which consists of five PSII-sc units. When the antenna in the first PSII-sc unit is excited, the exciton has the possibility to transfer to adjacent PSII-sc units through EET along the ***b*** direction. This diffusion-like behavior of the exciton allows for the exploration of multiple PSII-sc units, expanding the range of energy transfer on the thylakoid membrane.

doi:10.6342/NTU202301637

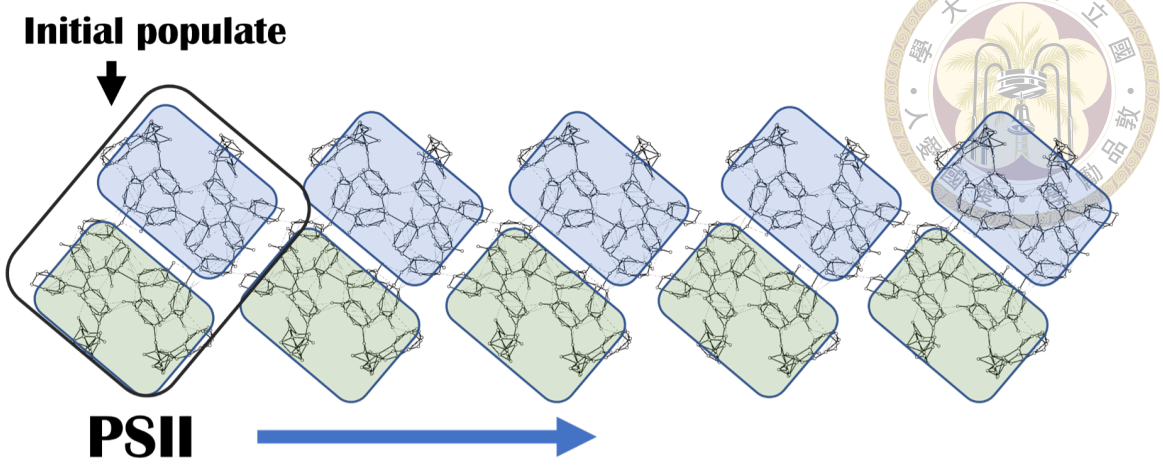

Figure 5.9: Illustration of exciton migrate to the others PSII-sc units in $\boldsymbol{a}$ direction

To quantify the extent of exciton migration across PSII-sc units, we introduce the concept of PSII length (L_{PSII}). This parameter provides an estimate of the number of PSII-sc units to which the exciton distributes. The PSII-sc length is defined by the following equation:

$$L_{PSII} = \left[\sum_i P_i^2 \right]^{-1} \tag{5.2}$$

Here, P_i represents the population of the exciton in the ith PSII-sc unit.

To investigate the behavior of L_{PSII} during exciton transfer on the membrane, we performed simulations by initially populating the first PSII-sc unit in a system of five PSII-sc units, and let exciton to migrate in $\boldsymbol{a}$ direction. We calculated the L_{PSII} at each population time and repeated this process for 100 realizations. The resulting average L_{PSII} at each population time is presented in Figure 5.10 b.

At 1 ns, we observed an increase in L_{PSII} from 1 to 2, indicating the transfer of the exciton to the second PSII-sc unit. Subsequently, the values of L_{PSII} converged around 2.5, suggesting a slight transfer of the exciton to the third PSII-sc unit. This demonstrates

doi:10.6342/NTU202301637

exciton migration to the second adjacent PSII-sc unit in the high light adaptive membrane.

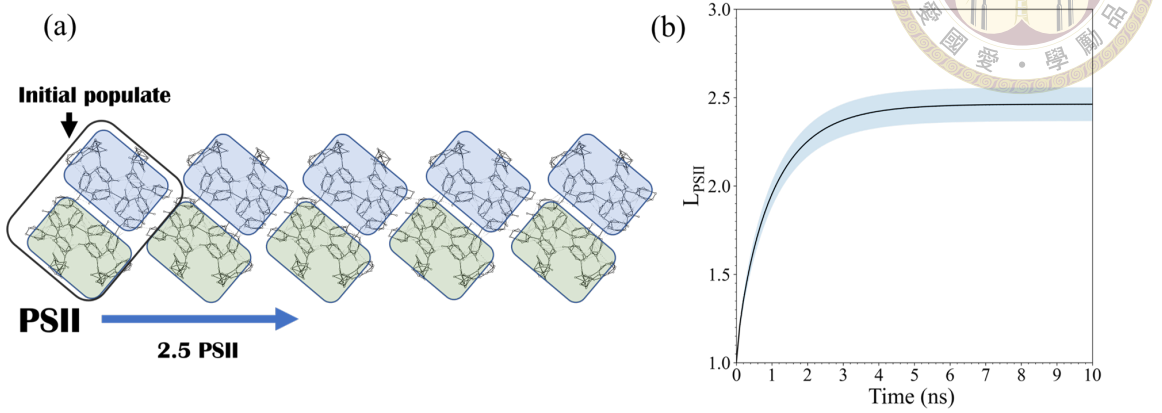

Figure 5.10: (a) illustration of the exciton migrate from the first PSII-sc unit (b) L_{PSII} changes as the probability of exciton diffusing among PSII-sc units. The blue region is $L_{PSII} \pm \sigma$.

To further confirm the previous diffusion results, we conducted a similar experiment to observe how L_{PSII} changes as the exciton transfers to PSII-sc units in the $\boldsymbol{a}$ direction and in the $-\boldsymbol{a}$ direction. In this experiment, we initially populated the third PSII-sc unit in a system of five PSII-sc units and allowed the exciton to migrate in both directions.

The simulations involved calculating L_{PSII} at each population time and repeating the process for 1000 realizations. Figure 5.11 b displays the average L_{PSII} at each population time.

At 1 ns, we observed an increase in L_{PSII} from 1 to 3, indicating the transfer of the exciton to the second and fourth PSII-sc units, consistent with the findings in Figure 5.10. Subsequently, the values of L_{PSII} converged around 4, suggesting a slight transfer of the exciton to the first and fifth PSII-sc units. This further demonstrates exciton migration to the adjacent PSII-sc units in the high light adaptive membrane, consistent with the results in Figure 5.10.

doi:10.6342/NTU202301637

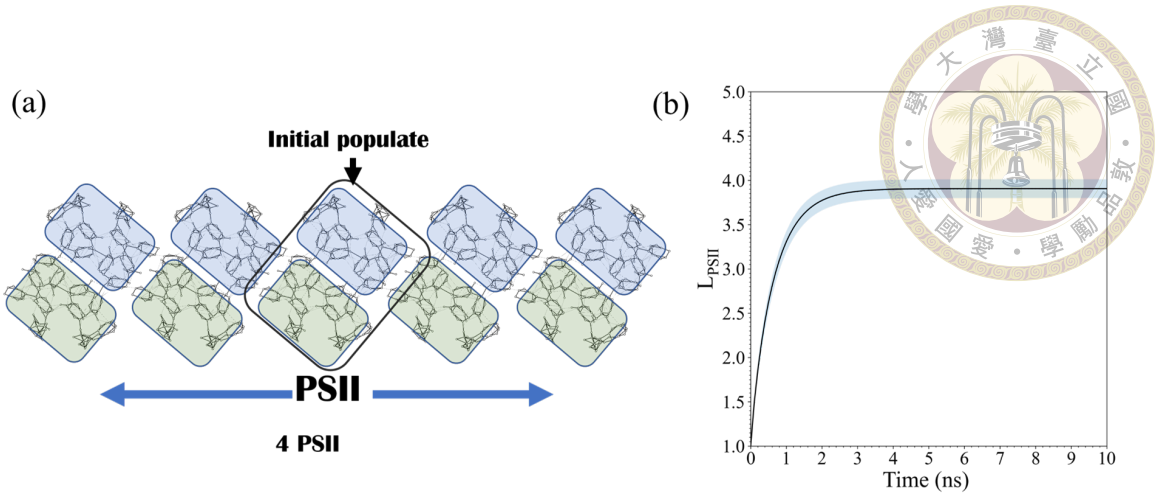

Figure 5.11: (a) illustration of the exciton migrate from the third PSII-sc unit (b) L_{PSII} changes as the probability of exciton diffusing among PSII-sc units. The blue region is $L_{PSII} \pm \sigma$.

5.3 Summary

In summary, when we analyze the L_{PSII} data, we discover interesting patterns in how excitons move in different light conditions. In the low light adaptive condition, the exciton only goes through one PSII-sc unit before stimulated emission occurs. Conversely, in the high light adaptive condition, the exciton takes a much longer journey, going through five PSII-sc units before stimulated emission occurs. This difference in the number of PSII-sc units involved means that it takes more time for the exciton to reach the RC in high light conditions. This longer time is important because it gives the system more chances to dissipate excess energy from the exciton. This helps protect the RC from potential damage caused by too much light and keeps the photosynthetic system stable.

doi:10.6342/NTU202301637

Chapter 6

The factors govering the QY of light harvesting

In this chapter, we investigate three parameters that can potentially influence the QY of light harvesting in PSII-sc. These parameters play crucial roles in determining the efficiency of energy transfer within the system and ultimately affect the overall QY of light harvesting.

The first parameter we examine is the site energies in PSII-sc. The site energies determine the internal energies of the clusters mentioned in section 4.2. By manipulating the site energies, we can explore how variations in these energies impact the efficiency of energy transfer and subsequently affect the QY of light harvesting.

The second parameter of interest is the level of static disorder on the pigments. Large static disorder can disrupt the energy transfer pathways to the RC, potentially hindering efficient light harvesting. Therefore, we investigate the effect of reducing the static disorder to create more favorable pathways for energy transfer, which can lead to an increase in the QY.

doi:10.6342/NTU202301637

The third parameter we focus on is the excitonic coupling between pigments. The strength of excitonic coupling directly influences the EET rate between pigments. By adjusting the excitonic coupling, we quantify the changes of this parameter impact on the efficiency of energy transfer and, consequently, the QY of light harvesting.

Through our investigation of these three parameters, we aim to gain insights into the key factors that affect the QY of light harvesting in PSII-sc. By understanding the role of site energies, static disorder, and excitonic coupling, we can uncover strategies for optimizing light harvesting efficiency and advancing our understanding of the underlying mechanisms in photosynthetic systems.

6.1 Site energies effect on QY

In this section, we explore the influence of site energies on the QY of light harvesting in PSII-sc. By manipulating the site energies, we can study how variations in these energies impact the efficiency of energy transfer and, consequently, affect the overall QY.

To investigate the relationship between site energies and the QY of light harvesting in PSII-sc, we focus our analysis on path 1, which was identified as the primary pathway observed in section 4.2. By selecting path 1, illustrated in Figure 6.1, we can specifically examine how variations in site energies along this pathway affect the efficiency of energy transfer and, subsequently, impact the QY.

doi:10.6342/NTU202301637

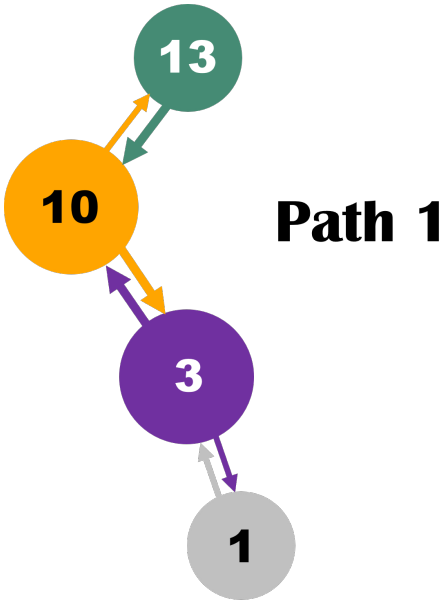

Figure 6.1: Illustration of Path in the upleft side of PSII

Note that the average site energies within clusters has great correlation with the effective internal energy of the cluster, which are shown in Figure 6.2. As a result, manipulating the site energies of cluster lead the the changes in effective internal energies of cluster, which directly influence the energy surface of EET path to RC.

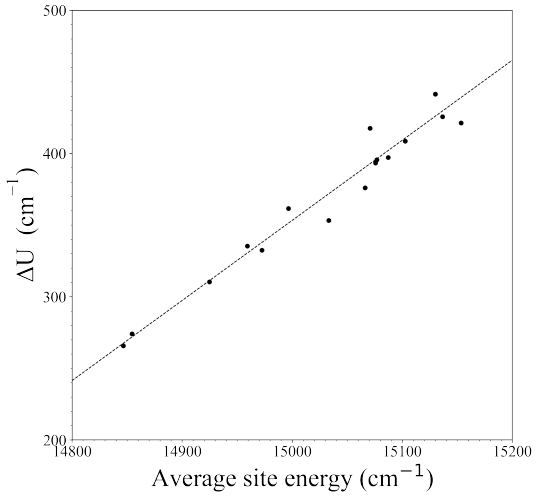

Figure 6.2: Correlation between average site energies of cluster and effective internal energies of the clusters (y=0.56x-8037)

doi:10.6342/NTU202301637

We conducted an investigation by shifting the site energies in cluster 3 and calculating the average QY at different energy shifts within the cluster. To ensure specific energy transfer pathways, we focus on path 1, which are cluster 13 - 10 - 3 - 1 (RC_1), and populated cluster 13.

By manipulating the site energies in cluster 3 and performing calculations for 1000 realizations, we obtained the average QY for each energy shift. Figure 6.3a illustrates the observed trend, where the QY decreases as the site energies in cluster 3 are increased or decreased. Raising the site energies blocks the energy transfer pathway to the RC, while lowering the site energies traps the exciton within cluster 3. Next, we shift the site energies in cluster 10 and calculate the average QY for 1000 realizations. Figure 6.3b shows similar results to Figure 6.3a.

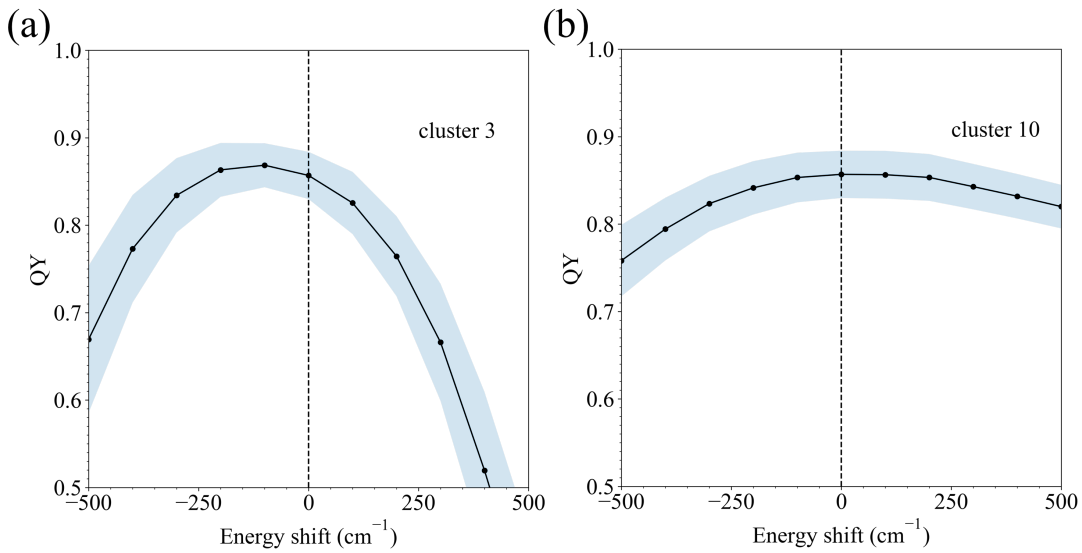

Figure 6.3: (a) The average QY for 1000 realization as a function of energy shift on the site energies in cluster 3(b) The average QY for 1000 realization as a function of energy shift on the site energies in cluster 10

In Figure 6.3, we observe that the maximum QY is achieved when there is no energy shift, and small perturbations of site energies lead to only slight changes in QY. For the energy shift of cluster 3, energy shifts within 100 cm^{-1} result in a QY larger than 0.8, while

doi:10.6342/NTU202301637

for the energy shift of cluster 10, energy shifts within 300 cm^{-1} result in a QY larger than 0.8. Therefore, the ability of PSII-sc to tolerate fluctuations in site energies may be a key factor contributing to its optimization for efficient light harvesting.

Continuing our investigation, we replicated the same experiment for path 2, which involves cluster 16 - 6 - 2 (RC_2), along with the populated cluster 16 depicted in Figure 6.4.

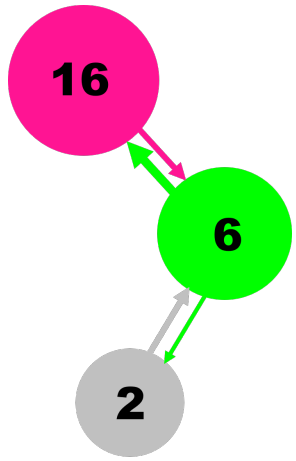

Figure 6.4: Illustration of Path in the upright side of PSII

By manipulating the site energies in cluster 6 and performing calculations for 1000 realizations, we obtained the average QY for each energy shift. Figure 6.5 illustrates the observed trend, where the QY decreases as the site energies in cluster 6 are increased or decreased. This experiment further confirms that the site energies in PSII-sc is optimized for light harvesting.

doi:10.6342/NTU202301637

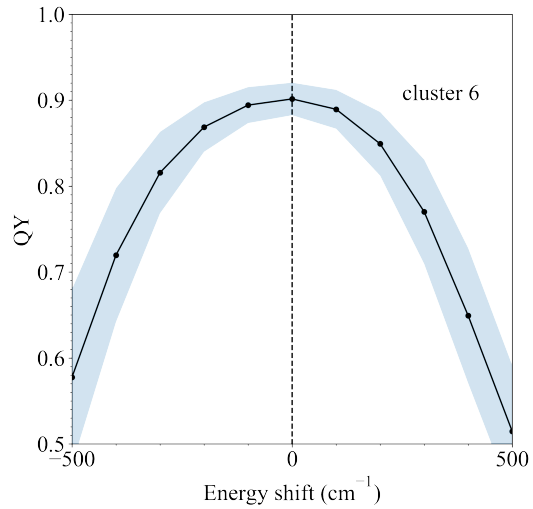

Figure 6.5: The average QY for 1000 realization as a function of energy shift on the site energies in cluster 6

Furthermore, we investigate the effect of site energies on QY using two different sets of site energies. One set has the site energies of Chl b at 15385 cm^{-1}, while those of Chl a and Pheo are at 14900 cm^{-1}. The other set has the site energies of all pigments at 14900 cm^{-1}. For each set, we calculate the distribution of QY using the method described in section 4.1, and the distributions are shown in Figure 6.6.

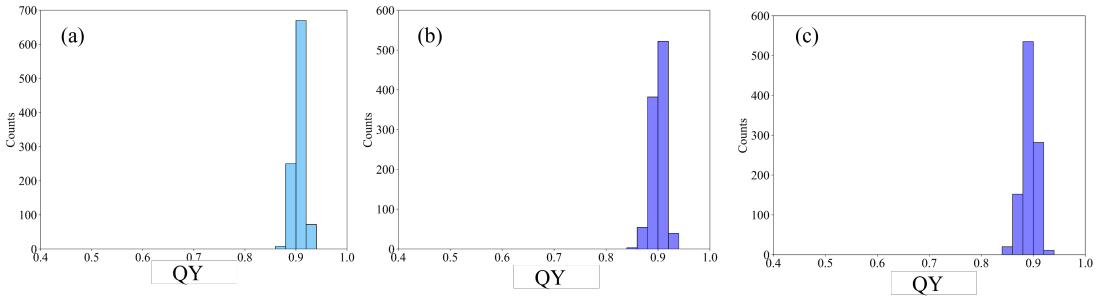

Figure 6.6: The distribution of QY with different sets of site energies (a) original set (b) the site energies of Chl b are 15385 cm^{-1}/ the site energies of Chl a and Pheo are 14900 cm^{-1} (c) the site energies of all pigments are 14900 cm^{-1}

The results reveal that as we set the site energies equally, the shallow energy gradient is slightly removed. For original set, the average QY is 0.91 and migration time is 207 ps;

doi:10.6342/NTU202301637

for site energies of Chl b at 15385 cm^{-1}, while those of Chl a and Pheo are at 14900 cm^{-1}, the average QY is 0.90 and migration time is 220 ps; for all pigments at 14900 cm^{-1}, the average QY is 0.89 and migration time is 242 ps. Overall, these findings suggest that the site energies in PSII-sc are finely tuned by nature to achieve efficient light harvesting.

In this section, the impact of site energies on light harvesting in PSII-sc is investigated by manipulating the site energies in the cluster. The results of the simulations provide insights into the optimal range of site energies required for achieving efficient light harvesting in PSII-sc. The simulations showed that small perturbations of site energies result in only slight changes in the QY of PSII-sc, and that the site energies in PSII-sc are naturally optimized to maximize the efficiency of light harvesting.

6.2 The level of static effect on QY

In this section, we investigate the impact of static disorder on the QY of light harvesting in PSII-sc. Our findings in previous section (Figure. 6.3) reveal that even with fluctuations in site energies within a range of 100 cm^{-1}, the QY remains consistently high, surpassing 0.8. This remarkable observation underscores the robustness of PSII-sc, as it can tolerate a certain level of static disorder and still maintain efficient light harvesting.

To investigate the level of static disorder effect on QY distribution, we calculate the QY distribution at differet level of static disorder. The PSII-sc has optimized its site energies for efficient light harvesting under ambient conditions with a static disorder of σ_s=0.5k_BT. In order to investigate how increasing fluctuation affects the QY, we increased σ_s and calculated the distribution of QY with values of 0.5, 1, and 2k_BT. The resulting comparison of distributions is shown in Figure 6.7.

doi:10.6342/NTU202301637

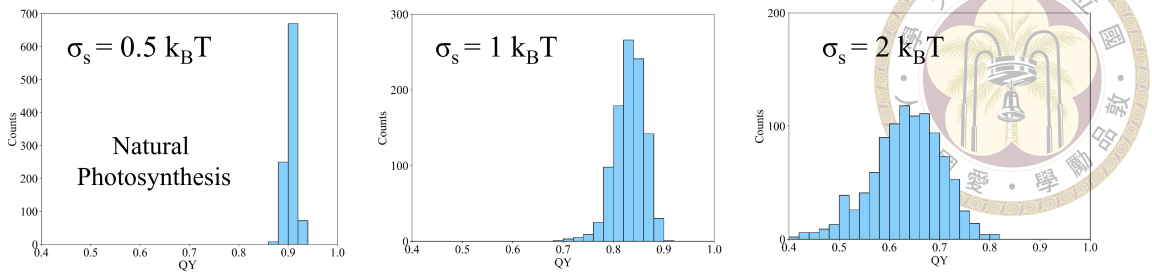

Figure 6.7: The distribution of the QY with different σ_s (a) $0.5k_BT$ (b) $1k_BT$ (c) $2k_BT$

At σ_s = $0.5k_BT$, most excitons trapped in sink sites can be thermally activated and transferred to RC. However, as static disorder increases, fewer excitons can be thermally activated, leading to a significant decrease in QY. This finding is consistent with previous literature, where Tan found that for EET with an energy gap lower than $1k_BT$, the EET rate is independent of ΔE [69]. For small uphill EET reactions, thermal energy can activate the exciton and transfer it. However, if the uphill energy is larger than $1k_BT$, the EET rate depends on the ΔE.

In summary, as σ_s becomes larger than thermal energy, the number of exciton trapped in PSII-sc increases. Consequently, the EET path to RC becomes slower, breaking the robustness of the PSII and leading to a decrease in QY. Clearly, small σ_s plays an important role in natural light harvesting.

6.3 Excitonic coupling effect on QY

In this section, we investigate the effect of excitonic coupling on the QY of the PSII-sc. We examine how the presence or absence of excitonic couplings influences the QY.

To explore this effect, we construct a total Hamiltonian and systematically add or remove excitonic couplings. The excitonic coupling between pigments is determined by

doi:10.6342/NTU202301637

the distance between their Mg centers. We recalculate the exciton coupling for the total Hamiltonian using a distance-based approach. The effective excitonic coupling (V_{nm}^{d-d}) is given by Equation 6.1, where R_{nm} represents the distance between the Mg centers of two pigments.The equation for the effective excitonic coupling is given by:

$$V_{nm}^{d-d} = \frac{100000}{R_{nm}^3} \tag{6.1}$$

We construct a new PSII-sc Hamiltonian by selectively adding or removing excitonic couplings based on their absolute values. Couplings with absolute values greater than 1 cm^{-1} are replaced with V_{nm}^{d-d}, while those with absolute values lower than 1 cm^{-1} are removed. This effective coupling matrix represents the original PSII-sc Hamiltonian. We calculate the average QY and standard deviation for 1000 realizations using the method described in 4.2.2. The obtained average QY is 0.902, with a standard deviation of 0.01, which closely aligns with the original QY distribution. A comparison of the coupling distribution between the total Hamiltonian and the original PSII-sc Hamiltonian is depicted in Figure 6.8.

doi:10.6342/NTU202301637

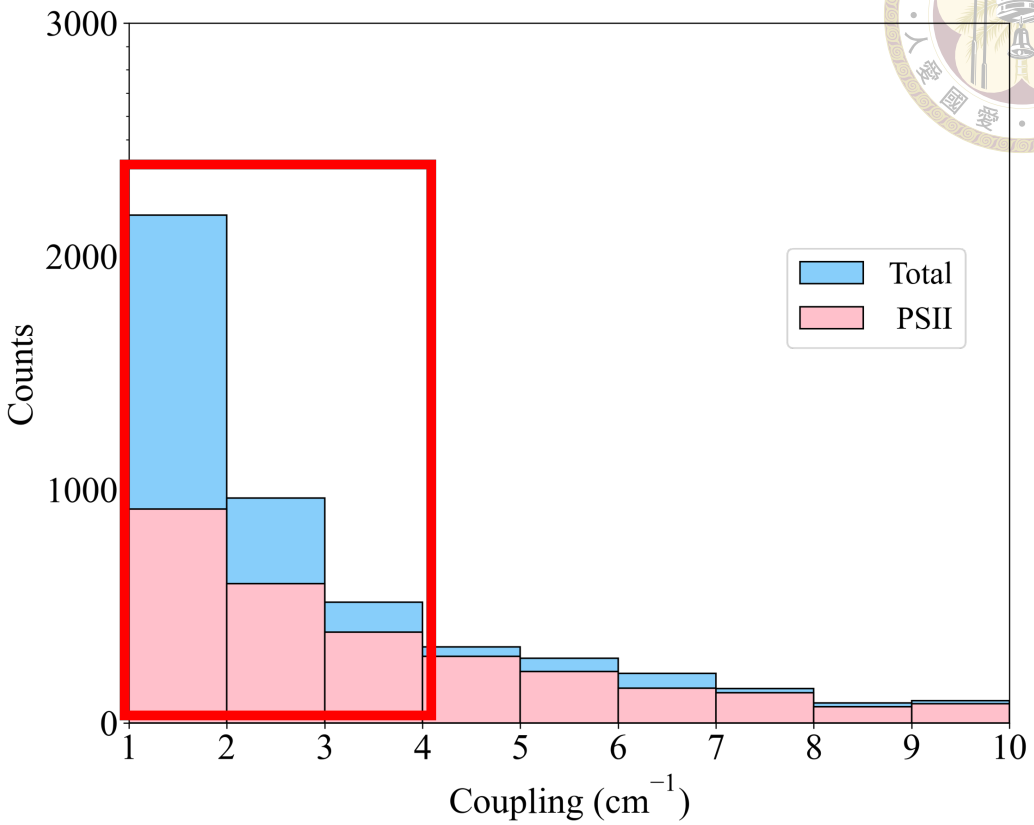

Figure 6.8: The distribution of excitonic couplings of total Hamiltonian and that of the original PSII-sc Hamiltonian

Figure 6.8 shows the excitonic couplings in the range of 1 to 10 for clarity. We found that the original PSII-sc Hamiltonian turns off a lot of low excitonic couplings ($V_{nm}^{d-d} < 4$ cm^{-1}) compared with total Hamiltonian. This reduction on excitonic couplings may avoid unfavorable slow random walk in EET to RC for excitons, and remain efficient EET to RC.

Using original PSII-sc Hamiltonian as a reference, we investigate the effect of removing the excitonic coupling of the original PSII-sc Hamiltonian. We remove the absolute excitonic coupling lower than 1, 2, 3, ..., 10 cm^{-1} from the original PSII-sc Hamiltonian and calculate the average migration time and standard deviation for 1000 realizations by method 4.2.2. Similarly, we investigate the effect of adding the excitonic couplings of

doi:10.6342/NTU202301637

the original PSII-sc Hamiltonian. We add the absolute excitonic coupling lower than 1, 2, 3, ..., 10 cm^{-1} to the original PSII-sc Hamiltonian, and calculate the average migration time and standard deviation for 1000 realizations by method 4.2.2. The results of how the average migration time changes as we change the degree of coupling are shown in Figure 6.9, where the ln(edges) at the x-axis is calculated by Eq. 6.2.

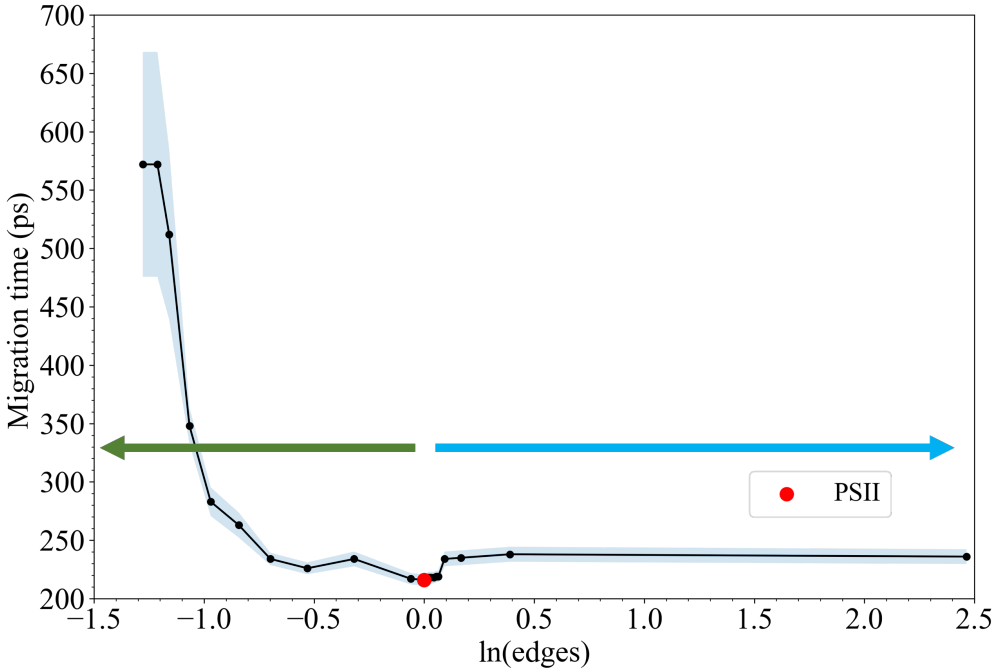

Figure 6.9: The changes of migration time to RC as the degree of coupling changing(the direction of green is reducing the degree, and the direction of blue is increasing the degree. The blue area represents the $\pm 2\sigma$) (ln(edges) is reference to the natural PSII-sc)

doi:10.6342/NTU202301637

ln(edge)	-1.278	-1.212	-1.158	-1.066	-0.970	-0.842
$\langle \tau_{mig} \rangle$	572	572	512	348	283	263
ln(edge)	-0.698	-0.530	-0.318	-0.061	0.000	0.019
$\langle \tau_{mig} \rangle$	234	226	234	217	216	218
ln(edge)	0.022	0.026	0.030	0.044	0.056	0.065
$\langle \tau_{mig} \rangle$	218	218	218	218	219	219
ln(edge)	0.092	0.168	0.389	2.464		
$\langle \tau_{mig} \rangle$	234	235	238	236		

Table 6.1: Comparison of $\langle \tau_{mig} \rangle$ to RCs for different number of edges

The number of edges in a Hamiltonian corresponds to the number of non-zero couplings in the system. To investigate how the number of edges influences the migration time to RCs, we utilize the natural logarithm of the number of edges (ln(edges)) as an independent variable.

Mathematically, we express ln(edges) as:

$$ln(edges)_i = \frac{N_i}{N_{PSII}} \tag{6.2}$$

In Equation 6.2, the subscript "i" represents different Hamiltonians, N_i represents the number of edges in the ith Hamiltonian, and N_{PSII} represents the number of edges in the original edges of the PSII system.

Figure 6.9 shows that as we remove more excitonic coupling, the robustness of QY in PSII-sc decreases, and the standard deviation of QY becomes larger. Inversely, we found that as we add more excitonic couplings, the migration time to RC will lightly increase. Increasing edges lead to unfavorable random walk in EET to RC, and this effect may more

doi:10.6342/NTU202301637

significant for larger light-harvesting systems.

Table 6.1 provides a summary of the average migration time to RCs for different numbers of edges. The ln(edge) values represent the natural logarithm of the number of edges, while $\langle \tau_{mig} \rangle$ represents the average migration time.

In summary, the degree of excitonic couplings plays a critical role in the efficiency and robustness of photosynthetic light harvesting systems. Through systematic manipulation of the excitonic coupling in the PSII-sc Hamiltonian, we found that the original PSII-sc Hamiltonian avoids low excitonic couplings, which reduces unfavor random walk in antenna and maintains efficient EET to RC. We also found that decreasing the degree of coupling leads to decreased robustness and larger standard deviation of QY, while increasing the degree of coupling leads to a slight increase in migration time to RC.

6.4 Summary

In this chapter, we investigate the effects of site energies, static disorder, and excitonic coupling on the QY of light harvesting in PSII-sc. Our analysis reveals that the present set of site energies is optimized for efficient light harvesting. Any deviation from these optimized site energies disrupts the balance of energy transfer pathways. Increasing the site energies blocks the energy transfer path to the RC, while decreasing the site energies traps the exciton within the antenna.

We also observed that PSII-sc exhibits a certain degree of tolerance to fluctuations in site energies within a range of 100 cm^{-1}. This suggests that the system can utilize thermal energy to overcome the noise in site energies and maintain a relatively high QY. So, as we increase the static disorder in site energies, enhancing the likelihood of exciton trapping

doi:10.6342/NTU202301637

in the antenna, thereby decreasing the QY and the robustness of QY.

Furthermore, we systematically manipulated the excitonic coupling in the PSII-sc Hamiltonian. Removing the exciton coupling resulted in decreased system robustness and an decreased QY. Conversely, when we introduced more excitonic coupling, we observed a slight increase in the migration time to the RC. This can be attributed to the unfavorable random walk behavior in energy transfer to the RC caused by increased connectivity.

doi:10.6342/NTU202301637

Chapter 7

Conclusion

In this study, we aim to understand how PSII-sc achieves efficient light harvesting despite the challenges posed by high entropy in the antenna and limited energy loss during the process. To simulate the EET dynamics in PSII-sc, we build up an effective model based on the Frenkel exciton model and TrEsp method. This model employs a Hamiltonian to describe the system and determines excitonic coupling. The EET rate are calculated using the Generalized Foster and modified Redfield methods. To validate our model, we compare migration times and examine the lowest states in the PSII-cc, demonstrating consistency with previous findings.

We specifically investigate the impact of static disorder on the QY by sampling 1000 realizations of the PSII-sc Hamiltonian. Our results reveal the robustness of PSII-sc against random static energetic disorder. We construct effective internal energy surfaces for each pathway leading to the RC. PSII-sc effectively employs energy barriers to confine excitons within the path, mitigating the unfavorable effects of entropy on light harvesting. Manipulating site energies creates a downhill energy gradient, facilitating efficient energy transfer to the RC.

doi:10.6342/NTU202301637

We investigate EET on the PSII membrane. In the low light adaptive membrane, excitons migrate across one PSII unit before stimulated emission occurs. In contrast, the high light adaptive membrane allows excitons to migrate across five PSII units before stimulated emission, prolonging the migration time to the RC. This extended migration time provides more opportunities for the dissipation of excessive exciton energy.

Furthermore, we investigated the effects of site energies, static disorder, and excitonic coupling on the QY of light harvesting in PSII-sc. Our analysis shows that the current set of site energies is optimized for efficient light harvesting, and any deviations from these optimized values disrupt the energy transfer pathways. Increasing the site energies blocks the transfer path to the RC, while decreasing them traps the exciton within the antenna, both leading to reduced QY. PSII-sc exhibits a degree of tolerance to fluctuations in site energies within a range of 100 cm^{-1}, utilizing thermal energy to maintain a high QY. However, increasing static disorder reduces the QY and system robustness. Moreover, we find that manipulating excitonic coupling affects system robustness and migration time to the RC, with increased coupling leading to unfavorable random walk behavior in energy transfer.

These findings provide valuable insights into the dynamics of EET in PSII-sc and highlight strategies employed by PSII-sc for efficient light harvesting and energy dissipation.

doi:10.6342/NTU202301637

References

[1] Roberta Croce and Herbert van Amerongen. Light harvesting in oxygenic photosynthesis: Structural biology meets spectroscopy. *Science*, 369(6506):eaay2058, 2020.

[2] Roman Kouřil, Jan P Dekker, and Egbert J Boekema. Supramolecular organization of photosystem II in green plants. *Biochim. Biophys. Acta Bioenerg.*, 1817(1):2–12, 2012.

[3] Cristina Pagliano, Guido Saracco, and James Barber. Structural, functional and auxiliary proteins of photosystem ii. *Photosynth. Res.*, 116:167–188, 2013.

[4] Xiaodong Su, Jun Ma, Xuepeng Wei, Peng Cao, Dongjie Zhu, Wenrui Chang, Zhenfeng Liu, Xinzheng Zhang, and Mei Li. Structure and assembly mechanism of plant c2s2m2-type psII-LHCII supercomplex. *Science*, 357(6353):815–820, 2017.

[5] Jan P Dekker and Egbert J Boekema. Supramolecular organization of thylakoid membrane proteins in green plants. *Biochim. Biophys. Acta - Bioenerg.*, 1706(1-2):12–39, 2005.

[6] Shou-Ting Hsieh, Lu Zhang, De-Wei Ye, Xuhui Huang, and Yuan-Chung Cheng. A theoretical study on the dynamics of light harvesting in the dimeric photosystem II core complex: regulation and robustness of energy transfer pathways. *Faraday Discussions*, 216:94–115, 2019.

doi:10.6342/NTU202301637

[7] Roberta Croce and Herbert Van Amerongen. Natural strategies for photosynthetic light harvesting. *Nat. Chem. Biol.*, 10(7):492–501, 2014.

[8] William P Bricker, Prathamesh M Shenai, Avishek Ghosh, Zhengtang Liu, Miriam Grace M Enriquez, Petar H Lambrev, Howe-Siang Tan, Cynthia S Lo, Sergei Tretiak, Sebastian Fernandez-Alberti, et al. Non-radiative relaxation of photoexcited chlorophylls: theoretical and experimental study. *Sci. Rep.*, 5(1):13625, 2015.

[9] Eric A Arsenault, Yusuke Yoneda, Masakazu Iwai, Krishna K Niyogi, and Graham R Fleming. The role of mixed vibronic qy-qx states in green light absorption of light-harvesting complex II. *Nat. Commun*, 11(1):6011, 2020.

[10] Akihito Ishizaki and Graham R Fleming. Insights into photosynthetic energy transfer gained from free-energy structure: Coherent transport, incoherent hopping, and vibrational assistance revisited. *J. Phys. Chem. B* ., 125(13):3286–3295, 2021.

[11] Gregory D Scholes, Graham R Fleming, Alexandra Olaya-Castro, and Rienk Van Grondelle. Lessons from nature about solar light harvesting. *Nat. Chem.*, 3(10):763–774, 2011.

[12] Gregory D Scholes, Graham R Fleming, Lin X Chen, Alán Aspuru-Guzik, Andreas Buchleitner, David F Coker, Gregory S Engel, Rienk Van Grondelle, Akihito Ishizaki, David M Jonas, et al. Using coherence to enhance function in chemical and biophysical systems. *Nature*, 543(7647):647–656, 2017.

[13] Elena Meneghin, Andrea Volpato, Lorenzo Cupellini, Luca Bolzonello, Sandro Jurinovich, Vincenzo Mascoli, Donatella Carbonera, Benedetta Mennucci, and Elisabetta Collini. Coherence in carotenoid-to-chlorophyll energy transfer. *Nat. Commun.*, 9(1):3160, 2018.

doi:10.6342/NTU202301637

[14] Tammie Nelson, Sebastian Fernandez-Alberti, Adrian E Roitberg, and Sergei Tretiak. Electronic delocalization, vibrational dynamics, and energy transfer in organic chromophores. *J. Phys. Chem. Lett.*, 8(13):3020–3031, 2017.

[15] Margherita Maiuri, Evgeny E Ostroumov, Rafael G Saer, Robert E Blankenship, and Gregory D Scholes. Coherent wavepackets in the fenna–matthews–olson complex are robust to excitonic-structure perturbations caused by mutagenesis. *Nat. Chem.*, 10(2):177–183, 2018.

[16] Tammie R Nelson, Alexander J White, Josiah A Bjorgaard, Andrew E Sifain, Yu Zhang, Benjamin Nebgen, Sebastian Fernandez-Alberti, Dmitry Mozyrsky, Adrian E Roitberg, and Sergei Tretiak. Non-adiabatic excited-state molecular dynamics: Theory and applications for modeling photophysics in extended molecular materials. *Chem. Rev.*, 120(4):2215–2287, 2020.

[17] Pei-Yun Yang and Jianshu Cao. Steady-state analysis of light-harvesting energy transfer driven by incoherent light: From dimers to networks. *J. Phys. Chem. Lett.*, 11(17):7204–7211, 2020.

[18] Lili Wang, Marco A Allodi, and Gregory S Engel. Quantum coherences reveal excited-state dynamics in biophysical systems. *Nat. Rev. Chem.*, 3(8):477–490, 2019.

[19] Jean-Luc Brédas, Edward H Sargent, and Gregory D Scholes. Photovoltaic concepts inspired by coherence effects in photosynthetic systems. *Nat. Mater.*, 16(1):35–44, 2017.

[20] Hong-Guang Duan, Valentyn I Prokhorenko, Richard J Cogdell, Khuram Ashraf, Amy L Stevens, Michael Thorwart, and RJ Dwayne Miller. Nature does not rely on

doi:10.6342/NTU202301637

long-lived electronic quantum coherence for photosynthetic energy transfer. *Proc. Natl. Acad. Sci.*, 114(32):8493–8498, 2017.

[21] Hiroyuki Tamura, Keisuke Saito, and Hiroshi Ishikita. The origin of unidirectional charge separation in photosynthetic reaction centers: nonadiabatic quantum dynamics of exciton and charge in pigment–protein complexes. *Chem. Sci.*, 12(23):8131–8140, 2021.

[22] David Mauzerall and Nancy L Greenbaum. The absolute size of a photosynthetic unit. *Biophys. Acta, Bioenerg.*, 974(2):119–140, 1989.

[23] Gregory D Scholes, Courtney A DelPo, and Bryan Kudisch. Entropy reorders polariton states. *J. Phys. Chem. Lett.*, 11(15):6389–6395, 2020.

[24] Xiche Hu, Ana Damjanović, Thorsten Ritz, and Klaus Schulten. Architecture and mechanism of the light-harvesting apparatus of purple bacteria. *Proc. Natl. Acad. Sci. U.S.A.*, 95(11):5935–5941, 1998.

[25] Graham R Fleming and Rienk van Grondelle. Femtosecond spectroscopy of photosynthetic light-harvesting systems. *Curr. Opin. Struct. Biol.*, 7(5):738–748, 1997.

[26] Xiche Hu, Thorsten Ritz, Ana Damjanović, Felix Autenrieth, and Klaus Schulten. Photosynthetic apparatus of purple bacteria. *Quart. Rev. Biophys.*, 35(1):1–62, 2002.

[27] Jian-Ren Shen et al. The structure of photosystem II and the mechanism of water oxidation in photosynthesis. *Annu. Rev. Plant Biol*, 66(66):23–48, 2015.

[28] Richard John Cogdell, Alastair Thomas Gardiner, Hideki Hashimoto, and Tatas Hardo Panintingjati Brotosudarmo. A comparative look at the first few milliseconds

doi:10.6342/NTU202301637

of the light reactions of photosynthesis. *Photochem. Photobiol. Sci.*, 7(10):1150–1158, 2008.

[29] Tihana Mirkovic, Evgeny E Ostroumov, Jessica M Anna, Rienk Van Grondelle, Govindjee, and Gregory D Scholes. Light absorption and energy transfer in the antenna complexes of photosynthetic organisms. *Chem. Rev.*, 117(2):249–293, 2017.

[30] Koen Broess, Gediminas Trinkunas, Chantal D van der Weij-de, Jan P Dekker, Arie van Hoek, Herbert van Amerongen, et al. Excitation energy transfer and charge separation in photosystem II membranes revisited. *Biophys. J.*, 91(10):3776–3786, 2006.

[31] Natalia P Pawlowicz, M-L Groot, IHM Van Stokkum, Jacques Breton, and Rienk van Grondelle. Charge separation and energy transfer in the photosystem II core complex studied by femtosecond midinfrared spectroscopy. *Biophys. J.*, 93(8):2732–2742, 2007.

[32] Stefano Caffarri, Koen Broess, Roberta Croce, and Herbert van Amerongen. Excitation energy transfer and trapping in higher plant photosystem II complexes with different antenna sizes. *Biophys. J.*, 100(9):2094–2103, 2011.

[33] Yutaka Shibata, Shunsuke Nishi, Keisuke Kawakami, Jian-Ren Shen, and Thomas Renger. Photosystem II does not possess a simple excitation energy funnel: time-resolved fluorescence spectroscopy meets theory. *J. Am. Chem. Soc.*, 135(18):6903–6914, 2013.

[34] Thanh Nhut Do, Hoang Long Nguyen, Stefano Caffarri, and Howe-Siang Tan. Two-dimensional electronic spectroscopy of the qx to qy relaxation of chlorophylls a in photosystem II core complex. *Chem. Phys.*, 156(14):145102, 2022.

doi:10.6342/NTU202301637

[35] Thanh Nhut Do, Hoang Long Nguyen, Parveen Akhtar, Kai Zhong, Thomas LC Jansen, Jasper Knoester, Stefano Caffarri, Petar H Lambrev, and Howe-Siang Tan. Ultrafast excitation energy transfer dynamics in the LHCII–CP29–CP24 subdomain of plant photosystem II. *J. Phys. Chem. Lett.*, 13:4263–4271, 2022.

[36] Doran IG Bennett, Kapil Amarnath, and Graham R Fleming. A structure-based model of energy transfer reveals the principles of light harvesting in photosystem II supercomplexes. *J. Am. Chem. Soc.*, 135(24):9164–9173, 2013.

[37] Lu Zhang, Daniel-Adriano Silva, Houdao Zhang, Alexander Yue, YiJing Yan, and Xuhui Huang. Dynamic protein conformations preferentially drive energy transfer along the active chain of the photosystem II reaction centre. *Nat. Commun.*, 5(1):1–9, 2014.

[38] Kapil Amarnath, Doran IG Bennett, Anna R Schneider, and Graham R Fleming. Multiscale model of light harvesting by photosystem ii in plants. *Proc. Natl. Acad. Sci. U.S.A.*, 113(5):1156–1161, 2016.

[39] Christoph Kreisbeck and Alán Aspuru-Guzik. Efficiency of energy funneling in the photosystem ii supercomplex of higher plants. *Chem. Sci.*, 7(7):4174–4183, 2016.

[40] Vladimir Novoderezhkin, Alessandro Marin, and Rienk van Grondelle. Intra-and inter-monomeric transfers in the light harvesting LHCII complex: the redfield–förster picture. *Phys. Chem. Chem. Phys.*, 13(38):17093–17103, 2011.

[41] Vladimir I Novoderezhkin and Rienk van Grondelle. Physical origins and models of energy transfer in photosynthetic light-harvesting. *Phys. Chem. Chem. Phys.*, 12(27):7352–7365, 2010.

doi:10.6342/NTU202301637

[42] Mino Yang and Graham R Fleming. Influence of phonons on exciton transfer dynamics: comparison of the redfield, förster, and modified redfield equations. *Chem. Phys.*, 282(1):163–180, 2002.

[43] Frank C Spano. The spectral signatures of frenkel polarons in h-and j-aggregates. *Acc. Chem. Res.*, 43(3):429–439, 2010.

[44] Yuan-Chung Cheng and Graham R Fleming. Dynamics of light harvesting in photosynthesis. *Annu. Rev. Phys. Chem.*, 60(1):241–262, 2009.

[45] ME Madjet, A Abdurahman, and T Renger. Interpigment coulomb couplings from ab-initio transition charges: application to strongly coupled pigments in photosynthetic antennae and reaction centers. *J. Phys. Chem. B* ., 110:17268, 2006.

[46] Thomas Renger. Theory of excitation energy transfer: from structure to function. *Photosynthesis. Research.*, 102(2):471–485, 2009.

[47] Gregory D Scholes, Carles Curutchet, Benedetta Mennucci, Roberto Cammi, and Jacopo Tomasi. How solvent controls electronic energy transfer and light harvesting. *J. Phys. Chem. B* ., 111(25):6978–6982, 2007.

[48] Vladimir I Novoderezhkin. Excitation dynamics in photosynthetic light-harvesting complex b850: exact solution versus redfield and förster limits. *Phys. Chem. Chem. Phys.*, 25(20):14219–14231, 2023.

[49] Gregory D Scholes. Long-range resonance energy transfer in molecular systems. *Ann. Rev. Phys. Chem.*, 54(1):57–87, 2003.

[50] Seogjoo Jang, Marshall D Newton, and Robert J Silbey. Multichromophoric förster resonance energy transfer. *Phys. Rev. Lett.*, 92(21):218301, 2004.

doi:10.6342/NTU202301637

[51] Jian Ma and Jianshu Cao. Förster resonance energy transfer, absorption and emission spectra in multichromophoric systems. i. full cumulant expansions and system-bath entanglement. *J. Chem. Phys.*, 142(9), 2015.

[52] Jian Ma, Jeremy Moix, and Jianshu Cao. Förster resonance energy transfer, absorption and emission spectra in multichromophoric systems. ii. hybrid cumulant expansion. *J. Chem. Phys.*, 142(9), 2015.

[53] Jeremy M Moix, Jian Ma, and Jianshu Cao. Förster resonance energy transfer, absorption and emission spectra in multichromophoric systems. iii. exact stochastic path integral evaluation. *J. Chem. Phys.*, 142(9), 2015.

[54] Wei Min Zhang, Torsten Meier, Vladimir Chernyak, and Shaul Mukamel. Exciton-migration and three-pulse femtosecond optical spectroscopies of photosynthetic antenna complexes. *J. Chem. Phys.*, 108(18):7763–7774, 1998.

[55] Yu-Hsien Hwang-Fu, Wei Chen, and Yuan-Chung Cheng. A coherent modified redfield theory for excitation energy transfer in molecular aggregates. *Chem. Phys.*, 447:46–53, 2015.

[56] Peter Hamm. Principles of nonlinear optical spectroscopy: A practical approach or: Mukamel for dummies. *University of Zurich*, 41(5):77, 2005.

[57] Frank Müh, Dominik Lindorfer, Marcel Schmidt am Busch, and Thomas Renger. Towards a structure-based exciton hamiltonian for the CP29 antenna of photosystem II. *Phys. Chem. Chem. Phys.*, 16(24):11848–11863, 2014.

[58] Hiroshi Haramoto, Makoto Matsumoto, and Pierre L' Ecuyer. A fast jump ahead algorithm for linear recurrences in a polynomial space. In *Sequences and*

doi:10.6342/NTU202301637

Their Applications-SETA 2008: 5th International Conference Lexington, KY, USA, September 14-18, 2008 Proceedings 5, pages 290–298. Springer, 2008.

[59] Frank Müh, Melanie Plöckinger, and Thomas Renger. Electrostatic asymmetry in the reaction center of photosystem II. *J. Phys. Chem. Lett.*, 8(4):850–858, 2017.

[60] Frank Müh, Melanie Plöckinger, Helmut Ortmayer, Marcel Schmidt Am Busch, Dominik Lindorfer, Julian Adolphs, and Thomas Renger. The quest for energy traps in the CP43 antenna of photosystem II. *J. Photochem. Photobiol. B: Biol.*, 152:286–300, 2015.

[61] Frank Müh and Thomas Renger. Refined structure-based simulation of plant light-harvesting complex II: linear optical spectra of trimers and aggregates. *Biochim. Biophys. Acta - Bioenerg.*, 1817(8):1446–1460, 2012.

[62] Adam G Koziol, Tudor Borza, Ken-Ichiro Ishida, Patrick Keeling, Robert W Lee, and Dion G Durnford. Tracing the evolution of the light-harvesting antennae in chlorophyll a/b-containing organisms. *Plant Physiol.*, 143(4):1802–1816, 2007.

[63] Vladimir I Novoderezhkin, Elisabet Romero, Jan P Dekker, and Rienk van Grondelle. Multiple charge-separation pathways in photosystem II: Modeling of transient absorption kinetics. *ChemPhysChem*, 12(3):681–688, 2011.

[64] Grzegorz Raszewski and Thomas Renger. Light harvesting in photosystem II core complexes is limited by the transfer to the trap: can the core complex turn into a photoprotective mode? *J. Am. Chem. Soc.*, 130(13):4431–4446, 2008.

[65] Mahboobe Jassas, Tonu Reinot, Adam Kell, and Ryszard Jankowiak. Toward an understanding of the excitonic structure of the CP47 antenna protein complex of

doi:10.6342/NTU202301637

photosystem II revealed via circularly polarized luminescence. *J. Phys. Chem. B*., 121(17):4364–4378, 2017.

[66] Maria J Schilstra, Jon Nield, Wolfgang Dörner, Ben Hankamer, Maria Carradus, Laura Barter, James Barber, and David R Klug. Similarity between electron donor side reactions in the solubilized photosystem II–LHC II supercomplex and photosystem-II-containing membranes. *Photosynth. Res.*, 60(2):191–198, 1999.

[67] Chern Chuang, Jasper Knoester, and Jianshu Cao. Scaling relations and optimization of excitonic energy transfer rates between one-dimensional molecular aggregates. *J. Phys. Chem. B*, 118(28):7827–7834, 2014.

[68] Roman Kouřil, Emilie Wientjes, Jelle B Bultema, Roberta Croce, and Egbert J Boekema. High-light vs. low-light: effect of light acclimation on photosystem II composition and organization in arabidopsis thaliana. *Biochim. Biophys. Acta - Bioenerg.*, 1827(3):411–419, 2013.

[69] Li-Ming Tan, Jie Yu, Tomoaki Kawakami, Masayuki Kobayashi, Peng Wang, Zheng-Yu Wang-Otomo, and Jian-Ping Zhang. New insights into the mechanism of uphill excitation energy transfer from core antenna to reaction center in purple photosynthetic bacteria. *J. Phys. Chem. Lett.*, 9(12):3278–3284, 2018.

doi:10.6342/NTU202301637